

Study of Excited Cascade Baryons and Preliminary Cross-Sections for $\Xi(1530)$ Using

Data from the GlueX Experiment

by

Brandon Christopher Lamont Sumner

A Dissertation Presented in Partial Fulfillment
of the Requirements for the Degree
Doctor of Philosophy

Approved April 2022 by the
Graduate Supervisory Committee:

Michael Dugger, Chair
Barry Ritchie
Richard Lebed
Ricardo Alarcon

ARIZONA STATE UNIVERSITY

May 2022

ABSTRACT

The spectra of predicted particles from elementary quark models (CQMs) are expansive, accurate for the low-lying spectra, but incomplete. The GlueX experiment at Jefferson Lab is a vehicle to study medium energy photoproduction of hadronic states. The primary goal of the GlueX collaboration is to study Quantum Chromodynamics (QCD, also known as the strong nuclear force) and the nature of quark confinement. The GlueX collaboration uses a polarized photon beam incident on a liquid hydrogen target (LH₂) to investigate the aftermath of photon-proton interactions.

The cascade baryons, denoted by \mathcal{E} , are defined by having two, second-generation, strange quarks with an additional first-generation light quark (u or d). Experimentally, few cascades have been discovered, which is the antithesis of what most models expect. The cascades have some favorable attributes but are difficult to detect because the production cross sections are small and direct production is unlikely. Fortunately, in the 12 GeV era of the GlueX experiment, there is sufficient energy, beam time and data analysis tools for the detection of excited cascade states and their properties.

From the reaction $\gamma p \rightarrow K^+ K^+ \mathcal{E}^- \pi^0$, the invariant mass spectra of $\mathcal{E}^- \pi^0$ system was surveyed for new possible resonances. The invariant mass spectrum has a strong $\mathcal{E}(1530)$ signal with other smaller resonances throughout the spectrum. Preliminary cross sections for the $\mathcal{E}(1530)$ that was photoproduced from the proton are presented at energies never before explored.

While the $\mathcal{E}(1530)$ couples almost exclusively to the $\mathcal{E}\pi$ channel, there is an easily identifiable $\mathcal{E}(1690)$ signal decaying $\mathcal{E}\pi$. Through the use of a simultaneous fitting routine of the \mathcal{E}^{*-} mass spectra, I was able to observe the $\mathcal{E}(1690)$ decaying to the $K\mathcal{A}$, as well as to the $\mathcal{E}\pi^0$ branch. With additional statistics, a measurement of the branching ratio should be possible.

Lastly, a partial wave analysis (PWA) was completed to verify that the total angular momentum of $\mathcal{E}(1530)$ is $J = 3/2$ and consistent with having positive parity. Additionally, there is evidence of a potentially interesting feature slightly above the mass of the $\mathcal{E}(1530)$ that should be more fully explored as new GlueX data becomes available.

DEDICATION

Dedicated to my son, Luther Scott Sumner. You are my why. You are the reason why I get up early, work late, keep going. You, my son, are the reason I have completed this endeavor.

ACKNOWLEDGMENTS

There have been several parts of this journey when I thought this mountain was insurmountable. I've been waiting to write this section until last to give me time to remember all of the people that have helped me get to this point. First to my tribe: my people; my family, blood or not, thank you for being there for me. To my parents, I do not have the words to say what you have meant to me from afar, uplifting me, sending resources, and most importantly sending love. To my brother and sister, Alex and Morgan, thank you for being my guard-rails, keeping me on track forcing me to be multidimensional and toughening me up. To Tiffany, my partner, thank you showering me with love during the dog days of my graduate school journey. T, thank you for undertaking the vast amount of roles from raising our son, finishing college and helping me traverse a tumultuous world.

Being at Arizona State University for nine years, it would be a disservice to not thank my mentors this university has provided. Mentors that guided, fostered, and helped build the kid that began this journey into the man I am today. I want to thank Dr. Amy Golden, Dr. Emeka Ikegwonu, Dr. Michael Tracey, Dr. Anna Zaniewski, Dr. Kevin Schmidt, Dr. Tanmay Vachaspati, Dr. Andrei Belitsky, and Araceli Vizcarra. Lastly I want to thank two professors that have made a profound effect on my physics career. First Dr. Barry Ritchie, you were the only professor to give me a chance to perform physics research as an undergraduate. You met me with open arms and gave me the only thing I wanted (an opportunity) and for that I am forever grateful. To Dr. Michael Dugger you are the single most important person I have the pleasure to come across here at ASU. Without hyperbole,

if not for you I would not have finished this degree. You rescued me when I was out of options and under your tutelage I was able to become the experimental Nuclear Physicist I am today. While you are my mentor, I will always view you as a close friend and hope and pray for a continued relationship. From the bottom of my heart to all mentioned thank you.

TABLE OF CONTENTS

	Page
LIST OF TABLES.....	ix
LIST OF FIGURES.....	x
CHAPTERS	
1 INTRODUCTION.....	1
1.1 Quark Models	1
1.2 QCD	5
1.3 Confinement.....	8
1.4 Partial Wave Analysis Introduction.....	11
1.4.1 Gottfried-Jackson Frame.....	15
1.4.2 Transition Amplitude Revisited.....	17
2 GLUEX EXPERIMENT.....	19
2.1 CEBAF.....	19
2.2 Bremsstrahlung Photon Tagger	21
2.2.1 Low Granularity Counter (Hodoscope).....	22
2.2.2 High Granularity Counter (Microscope).....	23
2.3 Coherent Bremsstrahlung Process.....	23
2.4 Triplet Polarimeter.....	26
2.5 Pair Spectrometer.....	27
2.6 Solenoid.....	28
2.7 Target.....	28
2.8 Start Counter.....	29
2.9 Drift Chambers.....	31
2.9.1 Central Drift Chamber.....	31
2.9.2 Forward Drift Chamber.....	32

CHAPTER	Page
2.10 Barrel Calorimeter.....	33
2.11 Time of Flight.....	35
2.12 Forward Calorimeter.....	36
2.13 Detection of Internally Reflected Cherenkov (DIRC).....	37
3 DATA SET.....	39
3.1 Run Period.....	39
3.2 Beam Photons.....	39
3.3 Photon Flux.....	41
3.4 Number of Scattering Centers per Unit Area.....	42
4 EVENT SELECTION.....	43
4.1 Kinematic Fitting.....	43
4.2 Reconstruction.....	45
4.2.1 $E^- \pi^0$ Decay Channel.....	45
4.2.2 $K^- \Lambda$ Decay Channel.....	51
4.3 Error Determination.....	55
5 MONTE CARLO EXCITED CASCADE.....	56
5.1 Event Generation.....	56
5.2 Efficiencies.....	60
6 $E(1530)$ CROSS SECTION.....	62
6.1 $E^- \pi^0$ Cross Section.....	62
6.2 Attempt at $E^0 \pi^-$ Cross Section.....	64
6.3 Past Measurements.....	67
6.4 Total Cross Section for $E^{*-}(1530)$	70
7 SIMULTANEOUS FITTING.....	74
8 PARTIAL WAVE ANALYSIS.....	78

CHAPTER	Page
9 CONCLUSIONS.....	89
9.1 Accomplishments	89
9.1.1 Cross Section Measurement.....	89
9.1.2 Simultaneous Fit.....	90
9.1.3 Branching Ratio.....	90
9.1.4 PWA.....	91
9.2 Future Work.....	91
REFERENCES.....	93

LIST OF TABLES

Table	Page
1.1 Cascade Baryons Invariant Mass and J^P Predicted from OGE, GBE, RQM and LQCD in Comparison to PDG Values.....	7
1.2 List of J^P for Cascade Resonances in 2021 PDG.....	12
7.1 Summary of the Analysis Cuts Used on the Spring and Fall 2018 Data Sets for the $E^- \pi^0$ and $K^- \Lambda$	76
7.2 Summary of $E\pi$ Invariant-Mass-Spectrum Gaussian-Fit Parameters in MeV, with Comparison to PDG[2] Values.....	79
8.1 Clebsch-Gordan Coefficients $\langle 10s\lambda J\lambda \rangle$ for $J=1/2$ and $J=3/2$	80
8.2 Small Wigner- d Table, $d_{m_1 m_2}^J$, for $J= 3/2, 1/2$ Expressed in Terms of Sines and Cosines.....	85

LIST OF FIGURES

Figure	Page
1.1 Vector (Left) and Pseudo-Scalar (Right) Meson Nonets. Horizontal Lines are Lines of Constant Strangeness and Diagonal Lines Represent Lines of Fixed Charge.....	2
1.2 Baryon Octet and Decuplet Housing the Cascade Baryon and Excited Cascade Baryon Respectively. Horizontal Lines Are Lines of Constant Strangeness and Diagonal Lines Represent Lines of Fixed Charge.....	3
1.3 t -channel Production Mechanism for Excited Cascades Through an Intermediate Hyperon Y^* Decaying $K^+ \Xi^{*-}$	4
1.4 Plot of the Strong Coupling Constant, α_s , Against the Momentum Transfer Q^2 . The Double Yellow Line is the Prediction from QCD, the Data Points Represent Several Different Experiments [7].....	9
1.5 Diagram of the Gottfried-Jackson Coordinate System Following a Reaction of the form $\gamma p \rightarrow K^+ K^+ \Xi^{*-}$. Particles Ξ and π Are the Decays of Particle Ξ^*	16
1.6 Decay of Resonance Ξ^* into Two Daughter Particles with Designated Spin (s), Orbital Angular Momentum (l), and Helicity (λ).....	17
2.1 Illustration of the Jefferson Lab Halls After the 12 Gev Upgrade in 2012 Where Additional Cryomodules, Power Supplies and Upgrade to the Halls and Magnets Were Added.....	19

Figure	Page
2.2 Illustration of the Cavities Used in Hall-D, the Polarity is Flipped Each Time the Electrons Travel to Another Node in the Cavity in Order to Accelerate the Electrons Through the Space.....	20
2.3 Hall-D Beamline Beginning from the Linearly Accelerated Electron Beam Passing Through the Photon Tagger into the GlueX Spectrometer and Finally into the Beam Dump.....	21
2.4 Depiction of the Electron Beam Incident on the Diamond Wafer Entering the Tagger Microscope and Hodoscope.....	22
2.5 The Enhancement Versus Photon Beam Energy Plots for PARA, PERP and Aluminum Are Shown in the Top Panel, with the Bottom Panel Showing the Polarization of the PARA and PERP Data. A Gray Band Represents the Systematic Uncertainty for the Polarization Measurement. In Both Panels Red Represents the PARA Data While Blue Represents PERP and Black is Aluminum [11].....	24
2.6 A Compactified Graphical Representation of The Hall-D Experiment from Photon Tagger to the GlueX Spectrometer, and Finally the Forward Detectors.....	25

Figure	Page
2.7 Illustration of the Pair Spectrometer. The Photon Beam Comes in from the Left and is Incident on the Converter That is Common to Both the TPOL and PS. When Pairs Are Produced in the Converter, Those Pairs Enter the PS Magnetic Field and Then Move Through the Vacuum Chamber and Finally to the Detector Elements. The Detector Elements Are Shown As PS And PSC, Where PSC Are Course.....	26
2.8 Diagram of Conical Target with Dimensions Given in Degrees and Inches.....	28
2.9 Pulse Tube Refrigeration System, Comprised of a Pulse Tube Refrigerator, Vacuum Chamber, Two Safety Storage Tanks, and the Target Cell Filled With LH_2	29
2.10 Drawing of Start Counter Surrounding LH_2 Target, Tapering Toward the Beamline on the Downstream Side.....	30
2.11 The CDC Endcap Straw-Tubes Layout is Shown on the Left, and the CDC Partially Filled with Straw Tubes is on the Right.....	31
2.12 Fully Constructed FDC Shown Outside of the GlueX Superconducting Solenoid Magnet.....	32
2.13 Individual FDC Package. From Bottom to Top, the FDC Package Starts with a Ground Plane Followed by a Down Cathode, Wire Frame Assembly and Topped Off with an Upper Cathode Layer.....	33

Figure	Page
2.14 3-D Model of BCAL Readout System, from the Light Guides, Silicon Photo-Multipliers and the Readout System.....	34
2.15 A Fully Constructed TOF Detector with a 12x12 Cm ² Cutout for the Beamline....	35
2.16 Fully Constructed FCAL with 2800 Lead Blocks Exposed.....	36
2.17 Cross Section of Photon Camera. The Babar Pads Slide into the Bottom and the Light is Bounced into the MaPMT.....	37
3.1 The Sideband and Signal Peak Structure Using Beam Time and RF-Time with a Confidence Level Above 10 ⁻⁴	40
3.2 The Tagged Photon Flux from the Pair Spectrometer.....	41
4.1 Confidence Level Distribution for the Reaction $\gamma p \rightarrow K^+ K^+ \Xi^- \pi^0$	44
4.2 Plots of β Vs p for a Kaon. The Plot on the Left is for Kaons That Have Time of Flight Information Only from the ST. The Plot on the Right is for the Case Where Time-Of-Flight Information is Taken from the TOF Detector.....	46
4.3 The Invariant Mass of the $\Lambda\pi^-$ System in GeV.....	47
4.4 The Invariant Mass of the Ξ^{*-} in Gev.....	48
4.5 K* Contribution of the Excited Cascade.....	49
4.6 A Plot of the Invariant Mass of the $\Xi^- \pi^0$ System for Events Where the Confidence Level is Greater Than 10 ⁻⁷	50
4.7 A Plot of the FOM Against the Confidence Interval.....	51

Figure	Page
4.8 Plot of the Invariant Mass of the Lambda Baryon Versus Against the Confidence Level.....	52
4.9 Invariant Mass of the K^+K^- System in GeV.....	53
4.10 Invariant Mass of $K^- \Lambda$ System in GeV.....	54
5.1 Feynman Diagram of the Photoproduction of the Excited Cascade.....	56
5.2 Kaon Polar Angle Vs Momentum in GeV.....	57
5.3 Invariant Mass of $\Xi^{*-}K^+$ System in GeV.....	58
5.4 Generic Feynman Diagram for a t -channel Process With Time Running Upward....	59
5.5 Counts vs Mandelstam Variable $-t$ for Events Within the $\Xi^*(1530)$ Peak.....	59
5.6 Illustration of the GlueX Spectrometer With Polar Acceptance Angles.....	60
5.7 Plot of the Efficiency Versus Beam Energy in GeV.....	61
6.1 Fit to the $\Xi^{*-}(1530)$ for Five Different Energy Bins With Each Energy Bin Spanning 800 Mev. The Photon Energy is Clearly Labeled on Each Histogram. The Green Line Represents the Full Fit (Gaussian with a First Order Polynomial Background) and the Red Line Represents the Background.....	63
6.2 Cross Section for the $\Xi^{*-}(1530) \rightarrow \Xi^- \pi^0$ for Beam Energies 7 – 11 GeV.....	64
6.3 Invariant Mass of the $\Xi^0 \pi^-$ (Reconstructed from $\Lambda \pi^0 \pi^-$) Without Vertex Fitting.....	65

Figure	Page
6.4 Plot of the Confidence Level Against the Invariant Mass for the $\Lambda\pi^0$ System in GeV.....	66
6.5 The Total Cross-Section For Differing Values of Center of Mass Energy (\sqrt{s}) for the Ξ^- and $\Xi(1530)$. Note: the Photon Energy Range Corresponding to the \sqrt{s} Range Shown for the $\Xi(1530)$ is ~ 3.5 to 5.3 GeV[17].....	68
6.6 Updated Total Cross Sections for the Ξ^- [19].....	69
6.7 Invariant Mass Distributions of the Ξ^- on the Left and Neutral Ξ^0 Right Measured in GeV.....	71
6.8 Total Cross Section for the $\Xi(1530)$ in nb Plotted Against Center of Mass Energy \sqrt{s} in GeV. CLAS g12 Data is in Red, My Total Cross Section is in Blue.....	73
7.1 Simultaneous Fit Between the $K^- \Lambda$ Channel and the $\Xi^- \pi^0$ Channel.....	75
8.1 Invariant Mass of the $\Xi\pi$ System Plotted Against $\cos(\theta_{GJ})$	81
8.2 Invariant Mass Distribution of Ξ^{*-} in GeV with $\cos\theta_{GJ}$, Between -1.0 and -0.8 , with Extracted $\Xi(1530)$ Having a Yield of 138 ± 12	82
8.3 Invariant Mass Distribution of Ξ^{*-} in GeV with $\cos\theta_{GJ}$, Between -0.8 and -0.6 , with Extracted $\Xi(1530)$ Having a Yield of 56 ± 7	83

Figure	Page
8.4 Invariant Mass Distribution of Ξ^{*-} in GeV with $\cos\theta_{GJ}$, Between -0.6 and -0.4 , with Extracted $\Xi(1530)$ Having a Yield of 96 ± 10	83
8.5 Invariant Mass Distribution of Ξ^{*-} in GeV with $\cos\theta_{GJ}$, Between -0.4 and -0.2 , with Extracted $\Xi(1530)$ Having a Yield of 119 ± 11	84
8.6 Invariant Mass Distribution of Ξ^{*-} in GeV with $\cos\theta_{GJ}$, Between -0.2 and 0.0 , with Extracted $\Xi(1530)$ Having a Yield of 72 ± 8	84
8.7 Invariant Mass Distribution of Ξ^{*-} in GeV with $\cos\theta_{GJ}$, Between 0.0 and 0.2 , with Extracted $\Xi(1530)$ Having a Yield of 61 ± 8	85
8.8 Invariant Mass Distribution of Ξ^{*-} in GeV with $\cos\theta_{GJ}$, Between 0.2 and 0.4 , with Extracted $\Xi(1530)$ Having a Yield of 72 ± 8	85
8.9 Invariant Mass Distribution of Ξ^{*-} in GeV with $\cos\theta_{GJ}$, Between 0.4 and 0.6 , with Extracted $\Xi(1530)$ Having a Yield of 73 ± 9	86
8.10 Invariant Mass Distribution of Ξ^{*-} in GeV with $\cos\theta_{GJ}$, Between 0.6 and 0.8 , with Extracted $\Xi(1530)$ Having a Yield of 32 ± 6	86
8.11 Invariant Mass Distribution of Ξ^{*-} in GeV with $\cos\theta_{GJ}$, Between 0.8 and 1.0 , with Extracted $\Xi(1530)$ Having a Yield of 78 ± 9	87
8.12 Efficiency Corrected Yields Versus $\cos(\theta_{GJ})$ Fit to an Intensity Function Having Only $J = 1/2$ Contribution.....	88

Figure	Page
8.13 Efficiency Corrected Yields Versus $\cos(\theta_{GJ})$ Fit to an Intensity Function Having Only $J = 3/2$ Contribution.....	88

Chapter 1

INTRODUCTION

1.1 Quark Models

With the exception of purely gluonic states (glueballs), hadrons are made, in part, by constituent quarks. At the heart of hadronic physics is a desire to understand the internal structure of hadronic particles and their properties. Quarks interact through the strong nuclear force which is rooted in the theoretical description of Quantum Chromodynamics (QCD). Empirically, though not proven theoretically, quarks are confined to be within bound states, which is the basis for “quark confinement”. From QCD, all naturally occurring particles are color singlets (analogous to a spin singlet state), having no net color and only interacting with other colorless states. Working with the three lightest quarks u , d , and s , most of the low-lying hadronic spectrum can be recreated through the outer product of an approximate $SU(3)$ flavor symmetry. Mesons, a quark and anti-quark pair, are the union of the normal and conjugate representations of $SU(3)$. In group theoretic language, the combination of two representations produces an octet and singlet, yielding much of the low-lying meson spectrum. Diagrams representing the vector- and pseudoscalar-meson nonets can be seen in Figure 1.1.

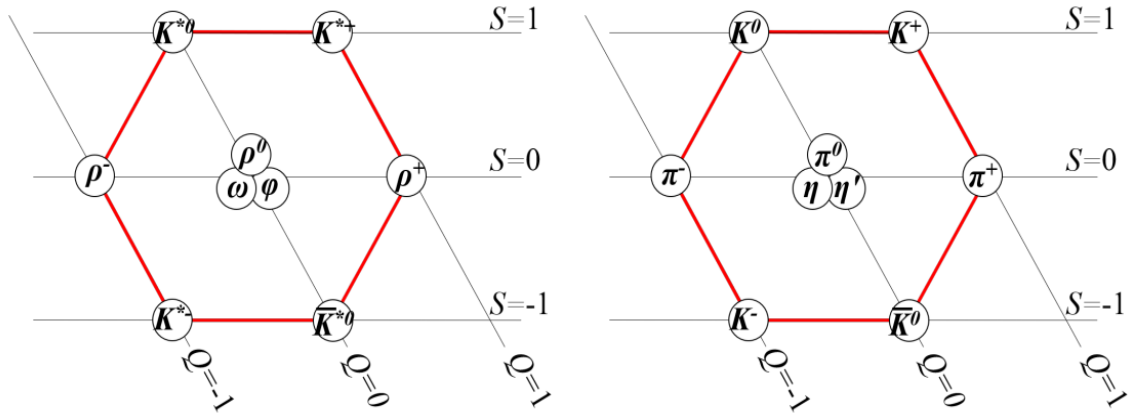


Figure 1.1: Vector (Left) and Pseudo-Scalar (Right) meson nonets. Horizontal lines are lines of constant strangeness and diagonal lines represent lines of fixed charge.

Quantum mechanical particle states are often characterized by the quantum numbers of angular momentum J , parity P , and charge conjugation C with the nomenclature J^{PC} . The pseudoscalar ($J^{PC} = 0^{-+}$) predicted states are made of K , π , η and η' mesons, while the vector nonet ($J^{PC} = 1^{-}$) is comprised of the K^* , ρ , ω , and ϕ mesons. Many of the predicted meson states have a mass consistent with their constituent internal quark masses modified by the spin-spin (hyperfine) interaction between them. Baryons follow a similar analysis, except baryons bring together three quarks. The direct product of three fundamental representations of $SU(3)$ decomposes into 27 different states. Of those 27 states, 10 belong to a decuplet, 16 states form two mixed-symmetry octets, and the remaining state is an anti-symmetric singlet. The baryons making up the two octets represent the same baryons but differ in the order of quarks assigned in the mixed symmetry. Diagrams of the baryon octet and decuplet are shown in Figure 1.2.

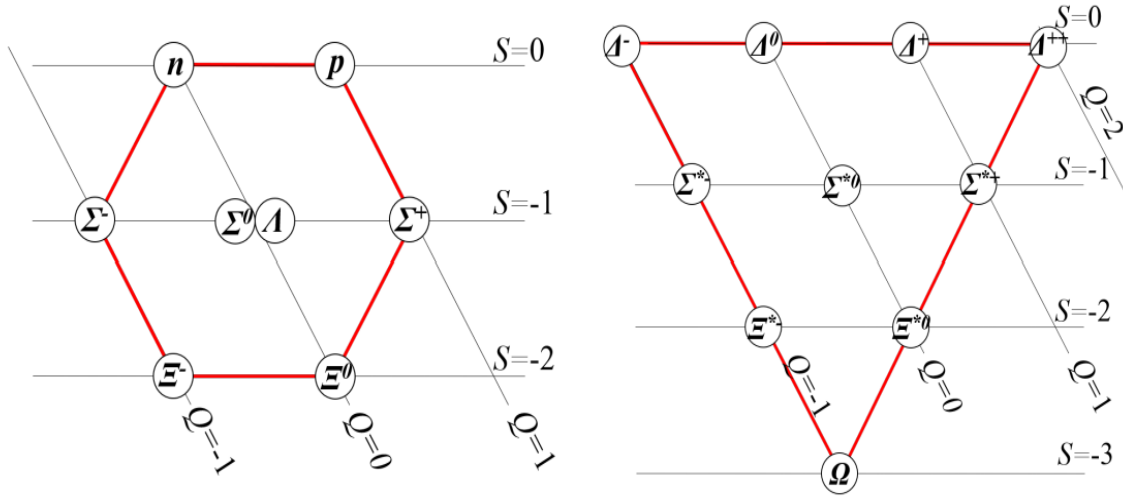


Figure 1.2: Baryon Octet and Decuplet housing the cascade baryon and excited cascade baryon respectively. Horizontal lines are lines of constant strangeness and diagonal lines represent lines of fixed charge.

Beyond the well-known proton and neutron, the predicted baryon states are Δ , Λ , Σ , Ξ and Ω . Using a similar mass formula as for the mesons, relying only on the hyperfine interaction for mass splitting, one can calculate the final bound state masses. Remarkably, this simple model only deviates from the measured mass by a few percent. Nevertheless, there are several issues hidden away. For example, the mass predicted using this simple model for the η' is off by a factor of three, and not all possible baryon excitations are included. To better shed light on the baryon spectrum, Capstick and Isgur wrote a paper in 1986 that uses a semi-relativistic Hamiltonian to predict 44 Ξ resonances with a mass less than $2.4 \text{ GeV}/c^2$ [1]. Currently, within that mass range, there are only 6 Ξ baryon states (neglecting charge) in the Particle Data Group PDG [2] that have three or four stars in that mass range (The PDG star system ranges from 1 to 4 stars, where a 1-star state has poor evidence of existence while the existence of a 4-star state is certain [2]). Additionally, due to the flavor independence of the QCD Lagrangian, the number of excited cascade (Ξ^*)

baryon states should be equal to the number of combined N^* and Δ^* states [3]. Not surprisingly, there are far fewer Ξ^* states when compared to N^* and Δ^* states, as there are only six cascades verified to exist while there are at minimum 25 based off the correspondence with the N^* and Δ^* states listed in the [2].

The QCD baryonic mass spectrum has yet to be solved analytically, but there have been advances using lattice QCD (LQCD), which shows a similar density of states as models dependent on one-gluon exchange and relativistic quark models. For baryons with two strange quarks, LCQD simulations are easier to run due to lower computational costs associated with having only a single light quark [4]. Experimental determination of the spectrum of cascade states in comparison to the spectrum predicted by LQCD provides additional motivation to find all of the cascade baryons, which may help assess the validity of LQCD spectrum.

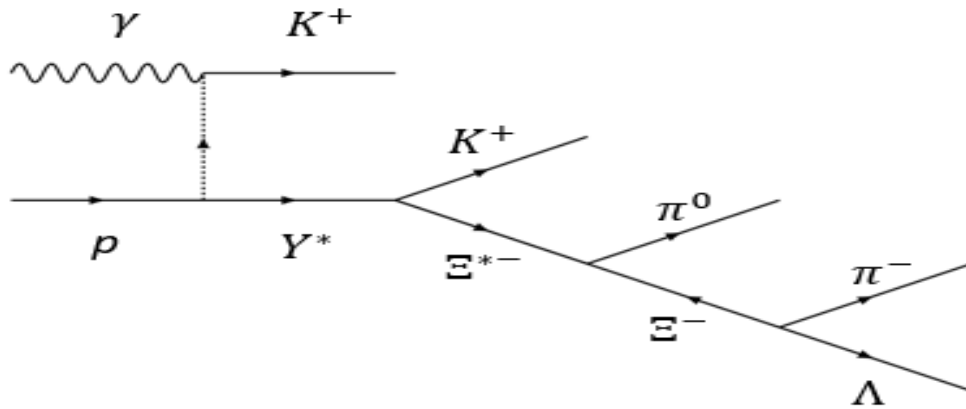


Figure 1.3: t -channel production mechanism for excited cascades through an intermediate hyperon Y^* decaying $K^+\Xi^{*-}$.

As aforementioned, the cascade baryon has great potential for uncovering some missing states originating from the discrepancy between the number of discovered and

predicted states. The photoproduction of the charged cascade $\Xi^*(1535)$ is a two-step process. Direct production of the excited cascade is OZI-suppressed due to the two strange and two anti-strange quarks produced at the production vertex. In the initial reaction, a positively charged kaon and high-mass hyperon are produced as shown in Figure 1.3.

Not much is known about the high-mass hyperon due to its very short life and large width in energy. The high-mass hyperon then decays quickly into another charged kaon and charged excited cascade. Figure 1.3 shows one such production and decay sequence. Exotic hadrons lie outside the previous two categories of constituent particles, falling under one of the umbrella terms of glueballs, pentaquark, tetraquarks (also known as XYZ states), or hybrids. Glueballs are made entirely of gluons and lack any valence quarks. Tetraquarks consist of two $q\bar{q}$ states that combine as a colorless state. The tetraquark can be represented as the direct product of two SU(3) octets that can be grouped as a 27-plet, two decuplets, two octets and a singlet, or as a molecular state of two $q\bar{q}$ singlets. Pentaquarks consist of four quarks and one antiquark. Lastly, hybrids are a $q\bar{q}$ system with one or more gluons promoted from virtual to real. Identifying exotic hadrons is most convincingly done by finding exotic J^{PC} quantum numbers, where J is the total angular momentum, P is the parity of the particle and C is the charge conjugation. In this case “exotic” means that the J^{PC} quantum numbers are not allowed within the constituent quark model.

1.2 QCD

Quantum Chromodynamics (QCD) is the theory of hadrons, their inner structure and how they interact with other hadrons. The dynamics and construction of all bound-state particles from their multiquark interactions is an important topic within particle

physics. There are several models that attempt to predict hadrons and their properties. Constituent quark models such as the one-gluon exchange (OGE), Goldstone boson exchange (GBE), non-relativistic and relativistic quark models (N/RQMs), along with LQCD, predict a plethora of bound states. The difference between hadronic models can be found within the kinetic and interaction terms of their Hamiltonians, which comes down to the approximations taken.

Starting with the relativistic one-gluon exchange (OGE) model, OGE originates from asymptotic freedom which implies quarks interact weakly when close together. Therefore, all interactions between quarks can be approximated to Feynman diagrams in QCD when the quarks are close together. The potential is split into two terms: a confinement term and an OGE term. The latter is collection of three parts, beginning with the strong force equivalent of a Coulombic interaction, a hyperfine interaction and spin-orbit coupling between each of the quarks [1]. The GBE model, instead, states the force mediator between the quarks originates from Goldstone bosons that are generated from the spontaneous breaking of chiral symmetry. Similar to the OGE model, the GBE model's interaction potential is of two parts: a confinement term and a hyperfine term [5]. The non-relativistic quark model has a similar potential term to that of the OGE, except the non-relativistic quark model neglects the Thomas precession spin-orbit term due to the non-relativistic treatment [1]. Table 1.1 shows the Ξ baryons predicted for several models, as well as measured experimental values listed in the PDG [2]. The last four columns are the predicted resonances for the OGE, GBE, RQM and LQCD. Of note,

LQCD predicts a similar density of states for cascade baryons, as seen in Table 1.1 when compared to the OGE model and the RQM.

J^P	State	PDG Mass Range	QM OGE	QM GBE	RQM	LQCD
1^+	1318 ^(****)	1314-1322	1305	1348	1310	1351±9
$\frac{3}{2}$	--	--	1840	1805	1876	2281±17
3^+	1530 ^(****)	1530-1532	1505	1528	1539	1635±8
$\frac{3}{2}$	--	--	2045	--	1988	2262±18
5^+	--	--	2045	--	2013	2296±13
$\frac{5}{2}$	--	--	2165	--	2141	2428±14
1^-	1690 ^(***)	1680-1700	1755	--	1770	1845±17
$\frac{3}{2}$	--	--	1810	--	1922	1875±15
3^-	1820 ^(***)	1818-1828	1785	1792	1780	1973±12
$\frac{3}{2}$	--	--	1880	--	1870	1998±17
5^-	--	--	1990	1881	1955	2127±11
$\frac{5}{2}$	--	--	--	--	--	--

Table 1.1: Cascade baryons invariant mass and J^P predicted from OGE, GBE, RQM and LQCD in comparison to PDG values.

Cross referencing the spectrum of states found in experiment with the known LQCD spectrum allows us to probe LQCD theory. Unfortunately, probing the lattice QCD model leads to problems. The mass of the pion is often an incorrect value (e.g. 300 MeV/c² instead of 140 MeV/c² [6]) and all other masses are incorrectly determined. Fortunately, two and three-strange-quark hadrons have the potential to help elucidate the spectrum of LQCD. The Ξ^* (dss or uss) baryon has a more auspicious content of light quarks, as well as excitations that are much narrower than that of the N^* or Δ^* , however with a much smaller cross section.

Because pions are lighter than kaons, pion decays are favored by phase space. However, since cascades contain two s quarks and only a single light u or d quark, there

are fewer ways to create a pion than a kaon. Thus, the phase-space favored branches to pion decay have less favorable combinatorics. The reduction in ways that a pion can be produced then reduces the decay width when compared to the N^* and Δ^* [3]. Additionally, the mass separation between resonances is larger than the resonance widths (~ 25 MeV) leading to cleaner identification of cascade baryons compared to N^* and Δ^* baryons (with widths of ~ 150 MeV). However, while the Ξ^* should prove to be useful for furthering our understanding of hadronic structure, there is very little Ξ^* information that has been added to the PDG tables since the late 90s.

The $\Xi(1530)$ baryon is unlike its higher mass cascade counterparts. The $\Xi(1530)$, having a mass below the ΛK threshold has a dominant decay branch of $\Xi\pi$, which is given as 100 percent in the PDG. Other excited cascades, like the $\Xi(1820)$ and $\Xi(2030)$, weakly couple to the $\Xi\pi$ channel and prefer to decay ΛK and ΣK respectively [2].

1.3 Confinement

Hadrons exhibit the property of asymptotic freedom, that cause interactions between particles to become asymptotically weaker at short distances. An experimentally evident, but theoretically unproven aspect of QCD, is quark confinement, which causes there to be no free quarks. In QCD, at short distances (large momentum exchanges), perturbative analysis can be used. The strength of the interaction is directly attributable to the QCD coupling “constant”. Figure 1.4 shows the coupling constant as function of the momentum transfer Q^2 .

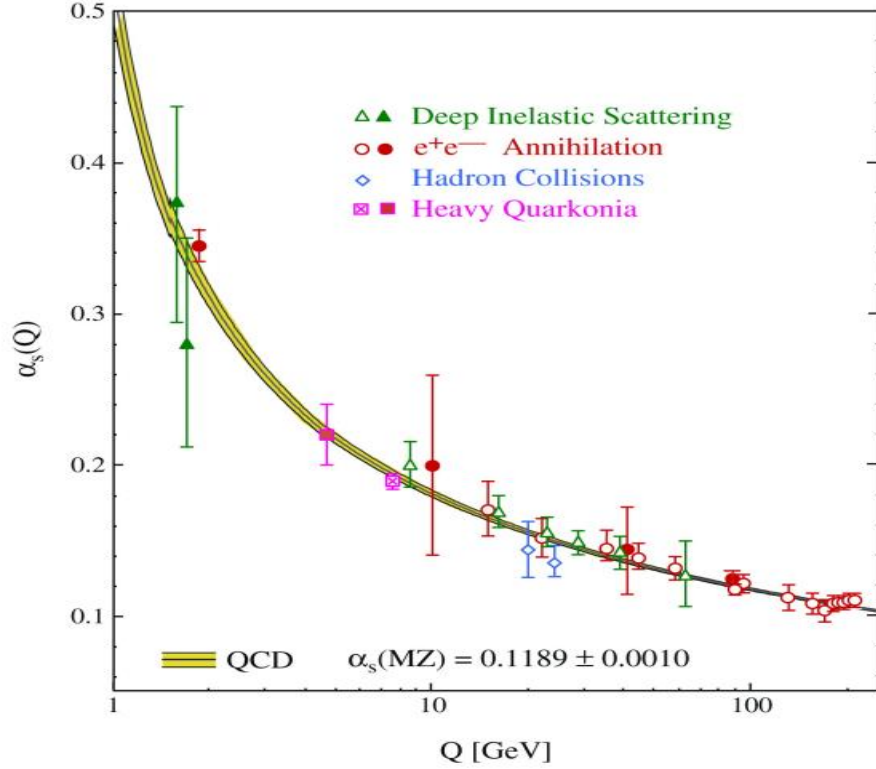


Figure 1.4: Plot of the strong coupling constant, α_s , against the momentum transfer Q^2 . The double yellow line is the prediction from QCD, the data points represent several different experiments [7].

While counterintuitive, the strength α_s , of the strong interaction is strongest at large distances/low momentum transfer (while for QED, the correlation between distance and coupling strength is the opposite). When in the perturbative regime of QCD, the simplest interaction between the quarks can be modeled as the exchange of one gluon (OGE). The OGE model contains a confining Coulomb-like potential, a hyperfine interaction and a constant quark term. In many ways, the machinery from QED is brought over to QCD, because single-gluon exchange only differs from QED by color factors and the coupling constant. In Isgur and Robert's paper [8] on baryon masses they describe a non-relativistic three-quark Hamiltonian:

$$H = \sum_i \left(m_i + \frac{p_i^2}{2m_i} \right) + \sum_{i<j} (V^{ij} + H_{hyp}^{ij}),$$

where m_i is the individual quark mass, p_i is the corresponding momentum, V^{ij} is a pairwise potential and H_{hyp}^{ij} is a pairwise hyperfine interaction. The above Hamiltonian uses a nonrelativistic kinetic energy, and the potential has two parts, V_{ij} , and H_{hyp}^{ij} . The V_{ij} term is spin independent, and can be expressed as:

$$V^{ij} = C_{qqq} + br_{ij} - \frac{2\alpha_s}{3r_{ij}},$$

where $r_{ij} = |r_i - r_j|$ and C_{qqq} is a constant term between the three quarks. The linear term br_{ij} is phenomenological in nature. The last term in the spin independent V^{ij} potential is a coulomb-like quark-quark interaction term. Regarding the spin dependent potential H_{hyp}^{ij} there are two terms that contain spin dependence, the hyperfine term ($\mathbf{S}_i \cdot \mathbf{S}_j$ coupling) and spin orbit term (not shown here). The H_{hyp}^{ij} term consists of two parts, a tensor term originating from color, magnetic dipole-dipole interaction, and a fermi contact term where the quarks overlap:

$$H_{hyp}^{ij} = \sum_{i<j} \frac{2\alpha_s}{3m_i m_j} \left\{ \frac{1}{r_{ij}^3} \left[\frac{3(\mathbf{S}_i \cdot \mathbf{r}_{ij})(\mathbf{S}_j \cdot \mathbf{r}_{ij})}{r_{ij}^2} - \mathbf{S}_i \cdot \mathbf{S}_j \right] + \frac{8\pi}{3} \mathbf{S}_i \cdot \mathbf{S}_j \delta^3(\mathbf{r}_{ij}) \right\}.$$

The spin-orbit term originates from the angular momentum interacting with the spin of the quarks and a Thomas precession piece (From the non-inertial reference frame). In the non-relativistic model of Capstick and Roberts, the spin-orbit terms are intentionally neglected, yet this model still creates the low-lying baryon spectrum well [8]. The different CQM

Hamiltonian's determine which salient features are used to parameterize the hadron. In basic quark models, that accurately determine the mass of the ground state baryons, the only dynamic variable is the spin-spin interaction of the quarks:

$$M(\text{Baryon}) = \sum_i^3 m_i + A \sum_{i<j}^3 \frac{\mathbf{S}_i \cdot \mathbf{S}_j}{m_i m_j},$$

where m_i is the mass of the i 'th quark, S_i is the spin of the i 'th quark which is proportional to the magnetic moment and A is a fitting parameter (experimentally, A has a best fit with a value of $4m_u^2/\hbar^2$). When $l=0$, the baryon mass formula has the same form as that of the spin-spin portion of the hyperfine interaction (Inversely proportional to mass squared and proportional to a spin squared) and works well in reproducing the baryon octet and decuplet.

1.4 Partial Wave Analysis Introduction

Since the 1980s, there have been few new measurements of the properties of cascade baryons, nevertheless, determining the quantum numbers (J^{PC}) of cascade resonances are critical in understanding the angular distribution of the resonances decay products. Unfortunately, there are only two excited cascades of determined total angular momentum and parity, while seven of the remaining eight listed, have completely unknown J^{PC} . Table 1.2 enumerates the PDG states with the corresponding J^P . The caveat in Table 1.2, is there has been evidence the $\Xi(1690)$ from the decay of the charmed lambda baryon, $\Lambda_c(\text{ud}\bar{c}) \rightarrow \Xi^- \pi^+ K^+$, for the total angular momentum and parity to be $1/2^-$.

Cascade State	J^P
$E(1530)$	$3/2^+$
$E(1620)$	$?^?$
$E(1690)$	$?^?$
$E(1820)$	$3/2^-$
$E(1950)$	$?^?$
$E(2030)$	$?^?$
$E(2120)$	$?^?$
$E(2030)$	$\geq 5/2^?$
$E(2120)$	$?^?$
$E(2500)$	$?^?$

Table 1.2: List of J^P for cascade resonances in 2021 PDG.

Table 1.2 list the J^P for cascade resonances in the PDG [2] and communicates that J^P for cascades has largely been unexplored by experiment, leaving the opportunity to discover the J^P quantum numbers through partial wave analysis (PWA). The PWA formalism will follow the process presented by Carlos Salgado and Weygand [9].

The reaction $\gamma p \rightarrow K^+ K^+ \Xi^- \pi^0$ decays via the strong interaction, but at intermediate energies, perturbative QCD cannot be used. The issue of being in the non-perturbative regime of QCD can be side-stepped by abiding by pillars of quantum field theory: conservation laws, Fermi’s golden rule, and the relativistic angular momentum-spin formalism. The assumption is made of having two-body decays within the “isobar model”. The final state is assumed to be in a bounded region of phase space such that the

cross section only depends on the angular dependencies. The data is fit to all possible J^P quantum states, i.e. partial waves, in the bounded phase space region that are independent of the mass. Beginning the analysis with Fermi's Golden rule:

$$\frac{d\sigma}{dt ds} = \sum_{ext\ spins} \int |M|^2 d\rho(\tau).$$

The above equation is the differential cross section, σ , in terms of Mandelstam variables s and t , while on the right side of the equation M is the Lorentz-invariant transition amplitude (connecting incoming and outgoing states), $d\rho$ is the Lorentz-invariant phase space and τ represents all phase space variables. Assuming that the cross-sectional dependence on Mandelstam variable s can be neglected, we can write the differential cross section as

$$\frac{d\sigma}{dt dm} = \sum_{ext\ spins} \int |M|^2 d\rho(\tau),$$

or in terms of intensity I

$$\frac{d\sigma}{dt dm} = \int I(\tau) d\tau,$$

where m is the mass of the excited cascade and

$$I(\tau) \equiv \sum_{ext\ spins} |M|^2.$$

The intensity is closely related to the probability of a particle being scattered into a particular angular distribution. The transition amplitude M is defined by the transition operator \hat{T} as

$$M = \langle out | \hat{T} | in \rangle.$$

The intensity can be related to the transition operator as

$$I(\tau) \equiv \sum_{ext\ spins} |M|^2 = \sum_{ext\ spins} \langle out | \hat{T} | in \rangle \langle in | \hat{T}^\dagger | out \rangle.$$

The initial spin density matrix $\widehat{\rho}_{in}$, houses the initial photon and target spin configurations and connects the various $|in\rangle$ polarization states:

$$\widehat{\rho}_{in} = |in\rangle\langle in|.$$

Generally, the initial spin density matrix is a 2x2 matrix defined by two state kets

$$\widehat{\rho}_{in} = \sum_{i,j} |i\rangle\langle j|.$$

The intensity can be written in terms of the spin density matrix as

$$I(\tau) \equiv \sum_{ext\ spins} \sum_{i,j} \langle out | \hat{T} \rho_{ij} \hat{T}^\dagger | out \rangle.$$

Factoring the transition operator into the production and decay of some set of states $|X\rangle$ and inserting a set of complete, orthonormal states (also known as partial waves) culminates in an expression for the partial wave amplitudes, ${}^i A_b(\tau)$.

$${}^i A_b(\tau) = \langle out | {}^i \hat{T}_{decay} | X \rangle,$$

where the subscript b refers to a specific partial wave and the superscript i connects to one of the subscripts of $\widehat{\rho}_{ij}$.

The production amplitude contains QCD calculations that are not computable at this time, but the expectation value of the production amplitude can be used as a weight on each partial decay amplitude. The “weights” are to be fit to the data and depend on external spins, not including the initial photon and target spin. Using similar nomenclature as above, the intensity spectrum to be fit can be expressed as the following:

$$I(\tau) \equiv \sum_{i,j} \sum_{b,b'} {}^i A_b(\tau) {}^{i,j} \rho_{b,b'} {}^j A_{b'}^*(\tau),$$

where ${}^{i,j} \rho_{b,b'}$ denotes to the resonance spin density matrix, which is similar to the initial spin density matrix, that houses the expectation value of the production amplitude. The above equation is fit to the data and can help determine the resonance quantum numbers. The frame that is chosen for the partial wave analysis of $E^* \rightarrow E^- \pi^0$ is the Gottfried-Jackson (GJ) frame.

1.4.1 Gottfried-Jackson Frame

The reaction that is the topic of this document is

$$\gamma p \rightarrow K^+ K^+ E^{-*}.$$

To analyze the angular distribution of the daughter particles of E , one can use several frames of reference. I chose the Gottfried-Jackson frame, where the angular distributions

of the daughter particles are measured from the rest frame of the Ξ^* and the z -axis points in the direction of the initial photon beam

$$\hat{z}_{GJ} = \frac{\vec{p}_\gamma(\Xi^*)}{|\vec{p}_\gamma(\Xi^*)|},$$

the y -axis is defined to be the normal to the production plane of Ξ^* in the CM frame.

$$\hat{y}_{GJ} = \frac{\vec{p}_\gamma \times \vec{p}_{\Xi^*}}{|\vec{p}_\gamma \times \vec{p}_{\Xi^*}|},$$

and the x -axis is defined by making the coordinate system right-handed:

$$\hat{x}_{GJ} = \hat{y}_{GJ} \times \hat{z}_{GJ}.$$

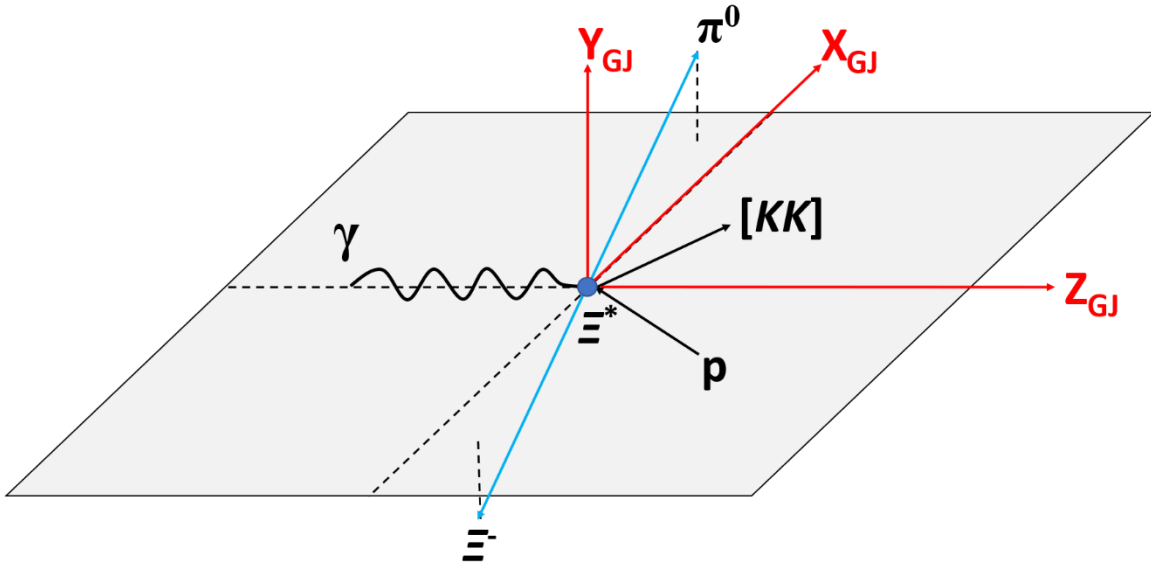


Figure 1.5: Diagram of the Gottfried-Jackson coordinate system following a reaction of the form $\gamma p \rightarrow K^+ K^+ \Xi^{*-}$. Particles Ξ and π are the decays of particle Ξ^* .

There is a problem associated with any choice of frame. The problem is in knowing with certainty which kaon emerges first. One prescription is to perform a Lorentz boost to

the rest frame of the resonance (Y^*), then boost from Y^* to the \mathcal{E}^{*-} . From the Lorentz group, two consecutive non-colinear boosts are equivalent to a single boost plus a rotation. Formally sequential boosts (K_i) are non-commuting with a commutator resulting in an angular momentum (J_k) as shown in the equation:

$$[K_i, K_j] = -i\epsilon_{ijk}J_k .$$

Thus, if the boost order is wrong, the “helicity frame” would be rotated from the true helicity frame by a Wigner rotation that is orthogonal to the boosts. If the boosts were to exist entirely within the production plane, the Wigner rotation would be orthogonal to the production plane. Because the Wigner rotation can exist orthogonal to the production plane, the choice of the GJ frame mitigates the contribution of the Wigner rotation in the definition of the coordinate system axes.

1.4.2 Transition Amplitude Revisited

Continuing the analysis from Salgado and Weygand, an expression can be derived for the transition amplitudes given a two-body decay like that shown in Figure 1.6.

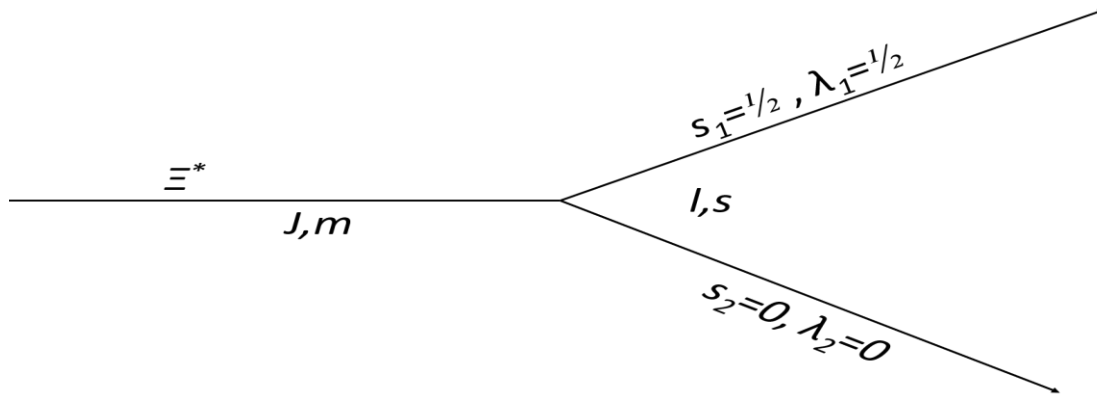


Figure 1.6: Decay of resonance Ξ^* into two daughter particles with designated spin (s), orbital angular momentum (l), and helicity (λ).

Per the recipe in section 1.4, we start the analysis of the decay of Ξ^* in the rest frame of Ξ^* (i.e. $p_1 + p_2 = 0$). Being in the rest frame of Ξ^* , the kinematics are determined by one momentum $p(\Omega_{GJ})$. Referring to the equation given below, the state ket is typically enumerated by the total angular momentum J and its component along z ($|J m\rangle$) while the bra describing the final state p_1 and p_2 , use helicities λ_1, λ_2 . Omitting the initial state indicator i , the decay amplitude can be expressed as

$$A_b(\tau) = \langle \Omega_{GJ}; \lambda_1 \lambda_2 | \hat{T}_{decay} | J m \rangle.$$

The full derivation is within [9]. The final expression for the decay amplitude is:

$$A_b(\tau) = \sqrt{\frac{2l+1}{4\pi}} F_l(p) \sum_{\lambda_1 \lambda_2} D_{m\lambda}^{J*}(\Omega_{GJ}) \langle l 0 s \lambda | J \lambda \rangle \langle s_1 \lambda_1 s_2^{-\lambda_2} | s \lambda \rangle a_{ls},$$

where the new factor $F_l(p)$ is the Blatt-Weisskopf centrifugal-barrier factor. The Blatt-Weisskopf factor that takes into account the centrifugal-barrier effects caused by the angular factors in the potential. The a_{ls} factor is a fit parameter that represents the transition amplitude

$$a_{ls} = \langle J m l s | \hat{T}_{decay} | J m \rangle.$$

Chapter 2

GLUEX EXPERIMENT

In this chapter I describe the experimental apparatus that was utilized in the creation of the data used in this document. I start with a brief discussion of the accelerator and then discuss the target and individual detector elements.

2.1 CEBAF

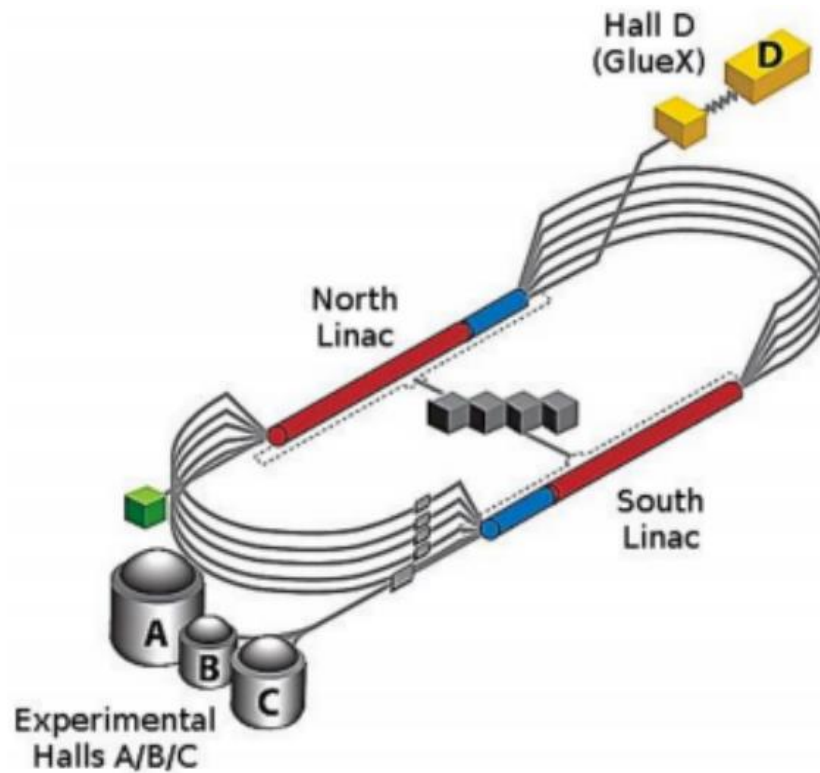


Figure 2.1: Illustration of the Jefferson Lab Halls after the 12 GeV upgrade in 2012 when additional cryomodules, power supplies and upgrade to the halls and magnets were added.

The Continuous Electron Beam Accelerator Facility (CEBAF) at Thomas Jefferson National Accelerator Facility initially began construction in 1987 with design specifications for a maximum electron beam energy of 4 GeV, that was later upgraded to 6 GeV. Two decades ago, in 2001, Jefferson lab started the process for the second upgrade to CEBAF, increasing the beam energy to 12 GeV. Along with the accelerator upgrade, the three halls at Jefferson lab were joined by a fourth hall, Hall D [10]. A diagram showing the placement of the halls in relation to the accelerator can be seen in Figure 2.1. Even though the CEBAF has been through several iterations, the CEBAF has continued to consist of the same base elements. The CEBAF consists of two parallel, superconducting radio frequency (RF) linear accelerators (linacs) joined by two recirculation arcs.

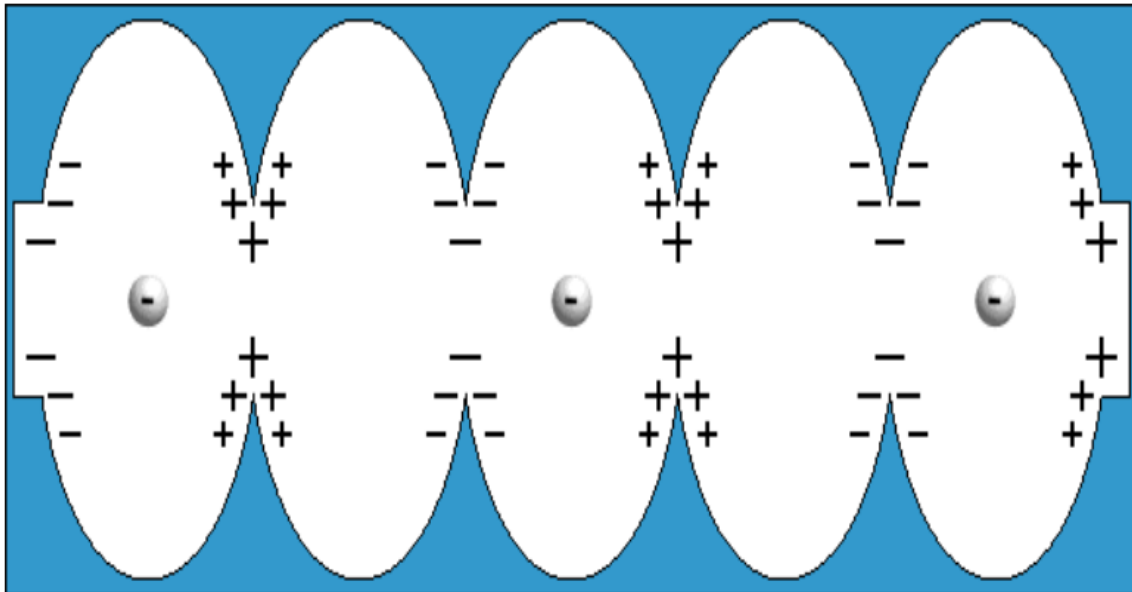


Figure 2.2: Illustration of the cavities used in Hall-D, the polarity is flipped each time the electrons travel to another node in the cavity in order to accelerate the electrons through the space.

The CEBAF electrons are accelerated to high energies with devices called RF cavities. As shown in Figure 2.2, the RF cavities push electron by placing negative and positive charge clusters in front and behind the accelerating electrons. The cavities are supercooled with cryomodules to drop the temperature of the niobium (the material the cavities are made from) such that the cavities become superconducting. Hall-D receives CEBAF electrons at 249.5 MHz (1/4.008ns), and the RF signal is multiplexed into four systems; the tagger hodoscope, forward drift chamber, pair spectrometer and the time-of-flight counter[11].

2.2 Bremsstrahlung Photon Tagger

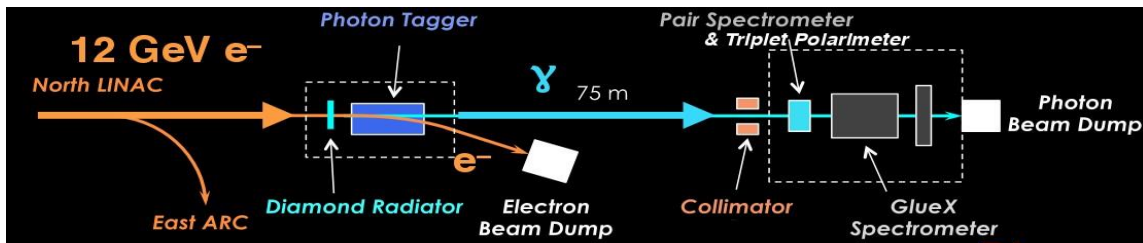


Figure 2.3: Hall-D Beamline beginning from the linearly accelerated electron beam passing through the photon tagger into the GlueX spectrometer and finally into the beam dump.

CEBAF produces an electron beam that is steered to the Hall-D experiment. As seen in Figure 2.3, the electron beam travels downstream and is incident on a diamond wafer, which may produce a secondary photon beam nearly parallel to the electron beam. The secondary photon beam is produced via the coherent Bremsstrahlung process inside the diamond wafer, and together with the electron beam, enter the region between the poles of the tagger magnet. The tagger magnet applies a constant Lorentz force to all electrons sent by the CEBAF, causing the electron beam to curve with a radius of curvature that depends on the electron's energy, deflecting the scattered electrons more

than the electrons that did not interact with the diamond. Noting the initial electron energy supplied by the accelerator, and the post-bremsstrahlung energy of the electron, one can determine the final photon energy, within the energy range determined by the physical dimension of the detector element that the post bremsstrahlung electron struck. This process is called tagging. The tagger microscope, as pictured in Figure 2.4, measures the coherent-peak energy region of the photon beam (8 to 9 GeV), while the tagger hodoscope measures a wider range of energies associated with different arcs of the electron beam. Using timing information, the tagger eliminates much of the accidentals that arise from the background that comes from within the photon tagger and/or the start counter. The tagger, however, becomes ineffective at rejecting accidentals for rates above 10^7 tagged photons/s in the coherent peak region [11].

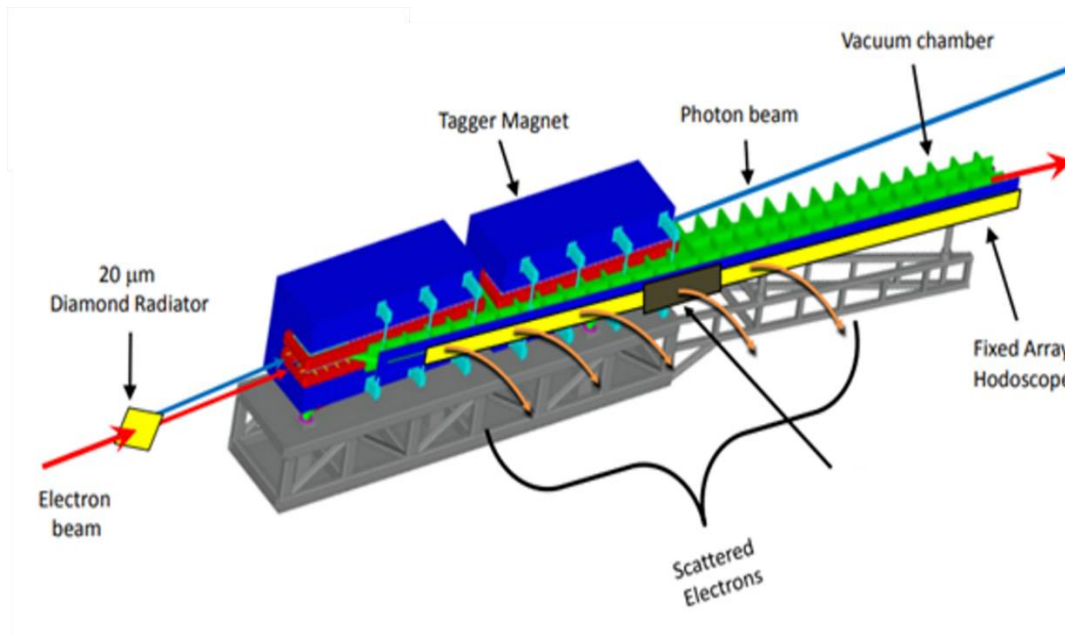


Figure 2.4: Depiction of the electron beam incident on the diamond wafer entering the tagger microscope and hodoscope.

2.2.1 Low Granularity Counter (Hodoscope)

The tagger hodoscope consists of 218 counters that are made of scintillating material and coupled to light guides. The hodoscope coarsely measures the tagged electrons associated with the photon beam energy ranging from 3.0 to 8.1 GeV and 9.1 to 11.8 GeV, with the energy gap filled by the tagger microscope [11].

2.2.2 High Granularity Counters (Microscope)

The tagger microscope consists of 102 columns of five thin scintillator fibers connected to photomultiplier tubes (PMTs). The microscope finely measures the tagged electrons for photons with energies from 8.1 GeV to 9.1 GeV [11].

2.3 Coherent Bremsstrahlung Process

By utilizing the coherent bremsstrahlung process, the Hall D experiment can photoproduce hadrons that have polarized amplitudes. The bremsstrahlung process happens when relativistic electrons propagate through matter and lose energy by radiating photons. The coherent bremsstrahlung process is more deliberate than the regular bremsstrahlung process and is used in high energy physics to produce energetic, linearly polarized photons within an oriented diamond radiator.

The accelerator provides a beam of electrons that are incident on a thin diamond converter. The nominal converter thickness was 50 μm . Within the diamond, the electrons interact with the electromagnetic field of the radiator's nuclei. To understand coherent bremsstrahlung, two things must be considered, the orientation of the diamond lattice and

the momentum of the high energy electron. Photons are emitted when the electrons are accelerated by the electric field of the atoms. If the momentum transfer from the electron to the atomic lattice matches a reciprocal lattice vector (Fourier transform of the actual lattice vector), the probability for an interaction is enhanced, which causes enhancements in the photon beam energy spectrum [12].

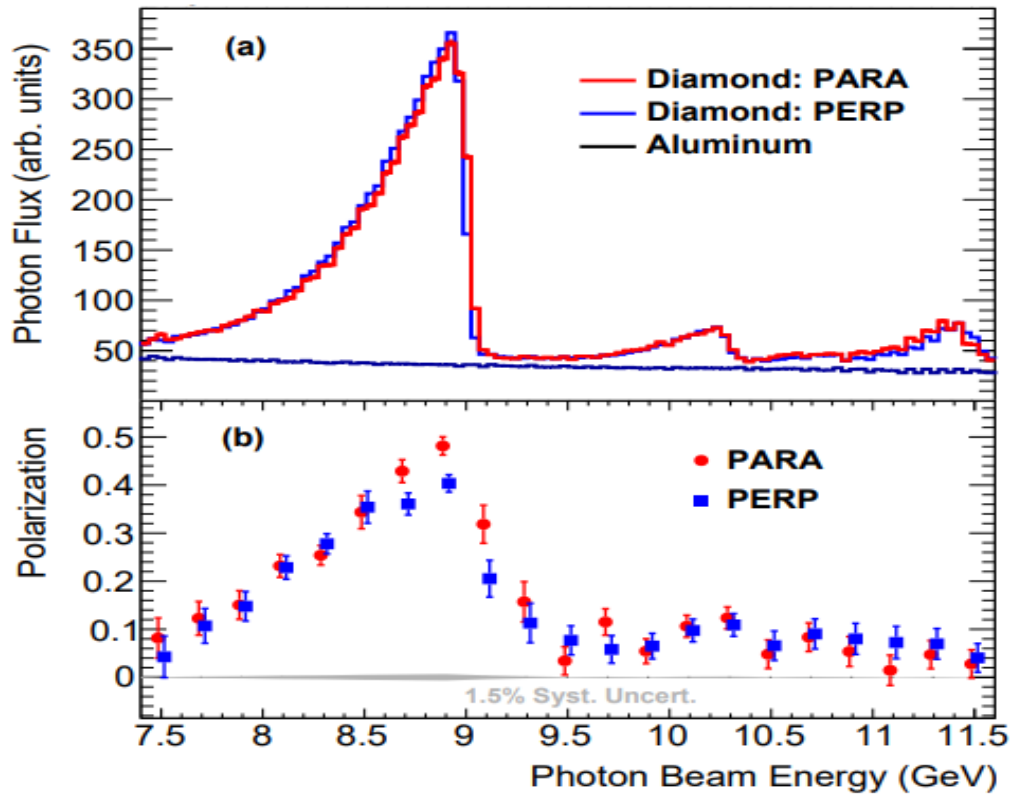


Figure 2.5: The enhancement versus photon beam energy plots for PARA, PERP and Aluminum are shown in the top panel, with the bottom panel showing the polarization of the PARA and PERP data. A gray band represents the systematic uncertainty for the polarization measurement. In both panels red represents the PARA data while blue represents PERP and black is aluminum [11].

The terms PARA and PERP are used in the collaboration to refer to the polarization vector of the photon being parallel or perpendicular to the floor of the experimental hall. There are special non-polarized runs (amorphous runs) that utilize an aluminum target that

does not produce enhancements in the photon spectrum. Enhancement plots are defined as the energy spectrum of the bremsstrahlung process divided by the energy spectrum of some portion of the amorphous data. The enhancement plots for PARA, PERP and aluminum are shown in the top panel Figure 2.5. The bottom panel of Figure 2.5 shows the polarization of the PARA and PERP data with a band of systematic uncertainty given as a gray region.

To maximize the enhancements, the orientation of the diamond must have the lattice vector perpendicular to the electron beam. By adjusting the crystal orientation, the peaks can be shifted to provide the greatest photon flux at the desired photon beam energy. The polarization is necessary for the Hall-D experiment because the asymmetries generated can contribute to refined analyses. Additionally, asymmetry measurements are favored in early analyses because many systematic uncertainties cancel when taking ratios of differences over sums. Lastly, to purify the amount of highly polarized photons, the photon beam is collimated to reduce contributions from unpolarized photons (with characteristic opening angles of m_e/E_γ that are greater than those of coherent bremsstrahlung). The characteristic polarization in the coherent peak region is around 40% [11].

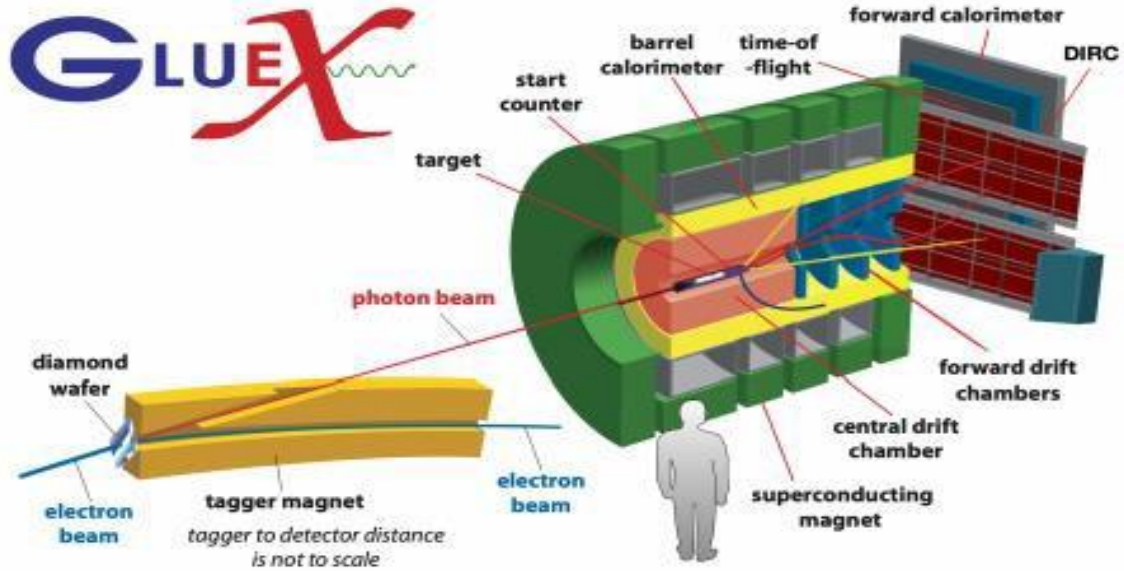


Figure 2.6: A compactified graphical representation of the Hall-D experiment from photon tagger to the GlueX spectrometer, and finally the forward detectors.

2.4 Triplet Polarimeter

The triplet polarimeter (TPOL) precedes the pair spectrometer (PS) and is the first detector to encounter the collimated photon beam in the GlueX experiment. TPOL and PS exist between the tagger magnet and GlueX spectrometer (Fig. 2.6). The purpose of TPOL is to measure the degree of polarization of the linearly polarized photon beam in the coherent peak region. Inside of the TPOL vacuum chamber, the linearly polarized photon beam is incident on a 75-micron beryllium converter where triplet photoproduction takes place. In triplet photoproduction, the incoming photon interacts with the electric field of an atomic electron and produces a high-energy electron-positron pair. The high-energy electron-positron pair continue downstream into the pair spectrometer, while the scattered atomic electron is detected by a silicon strip detector that provides energy and azimuthal angle information. The azimuthal angle distribution of the recoil electron contains the

information regarding photon beam polarization. The degree of polarization must be known within ± 0.04 absolute uncertainty for the partial wave analyses done by the GlueX experiment to be effective in resolving parity information [4].

2.5 Pair Spectrometer

The pair spectrometer, pictured in Figure 2.7, is located downstream from the TPOL and is used to measure the energy of electron-positron pairs generated in a beryllium foil that is located within the TPOL vacuum chamber.

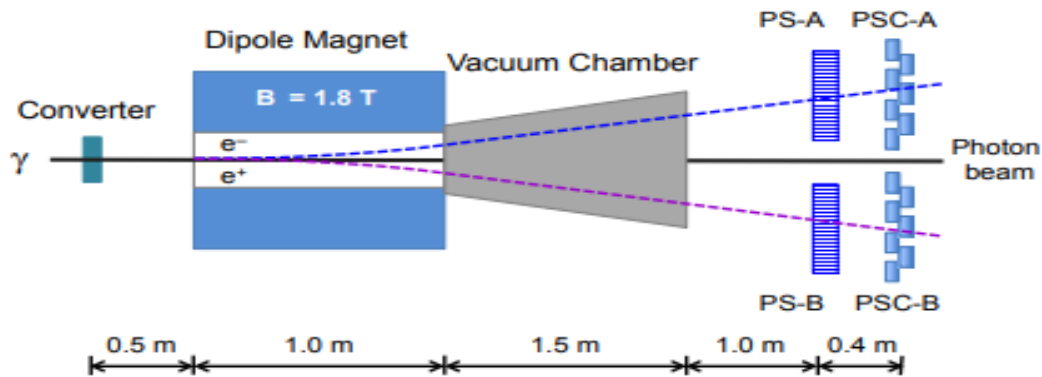


Figure 2.7: Illustration of the pair spectrometer. The photon beam comes in from the left and is incident on the converter that is common to both the TPOL and PS. When pairs are produced in the converter, those pairs enter the PS magnetic field and then move through the vacuum chamber and finally to the detector elements. The detector elements are shown as PS and PSC, where the PSC are course counters.

Sequentially, after leaving TPOL the electron positron pair enters the 1.8 T dipole magnet of the PS. The magnetic field separates the pair and is followed by a 1.5 m long vacuum chamber [11]. Further downstream, there are a pair of two-layered detectors on each side of the beamline: a high granularity hodoscope followed by a set of coarse counters. The hodoscope is used to precisely determine the electron/positron momentum that is related to the x -position of each tile, where the x -axis is defined perpendicular to the

beamline and parallel to the floor. The purpose of the coarse counter is to form a PS trigger that requires a coincidence hit in both sides of the coarse counters (left and right).

2.6 Solenoid

Encompassing the start counter (ST), central drift chambers (CDC) and forward drift chambers (FDC) is the superconducting solenoid magnet. The magnet consists of four separate coils located in vacuum separated compartments that generates a magnetic field parallel to the beamline. The GlueX solenoid runs at a nominal current of 1350 A, producing a magnetic field of 2.0 T in the bore that is 4.8 m long, has an inner diameter of 2.9 m and an outer diameter of 3.8 m [11].

2.7 Target

The linearly polarized photon beam is incident on a vacuum chamber antecedent to the liquid hydrogen target (LH_2). The target is incased in a 30 cm long Kapton conical shell. The Kapton is used because Kapton has high thermal conductivity at low temperatures. When filled with LH_2 , the target is cooled to a temperature of 17K and maintained at 18 psia [11]. A diagram of the shell is shown in Figure 2.8.

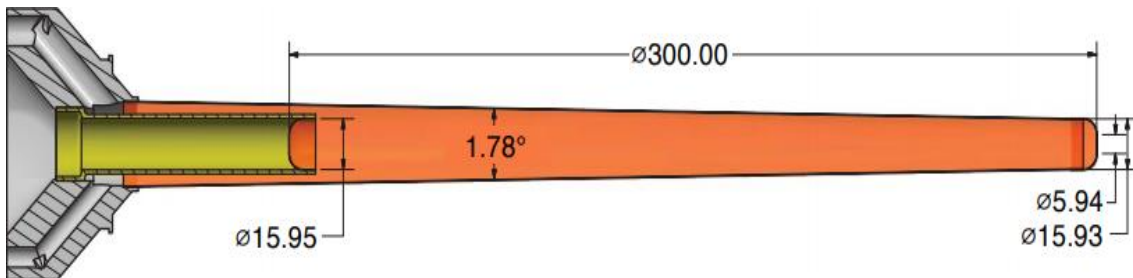


Figure 2.8: Diagram of conical target with dimensions given in degrees and inches.

The GlueX collaboration constructed a pulse tube refrigeration system to keep the target at a constant temperature. A diagram of the refrigeration system is provided in Figure 2.9. The refrigeration system takes the hydrogen gas from the storage tanks and condenses the gas into liquid hydrogen. From the collimated photon beam perspective, the number of scattering centers per unit area τ , is $1.32 \times 10^{24}/\text{cm}^2$ or 1.32 per barn.

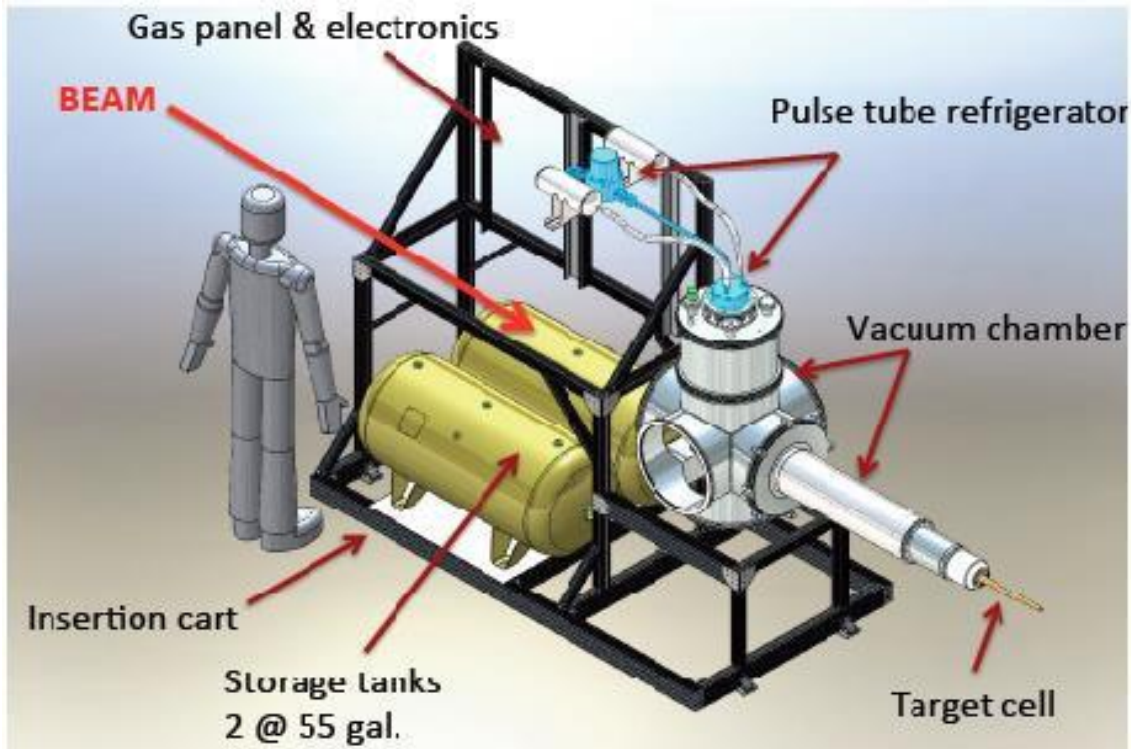


Figure 2.9: Pulse tube refrigeration system, comprised of a pulse tube refrigerator, vacuum chamber, two safety storage tanks, and the target cell filled with LH_2 .

2.8 Start Counter

The start counter (ST) is a detector that is used to help identify which accelerator-provided electron beam bucket a photon originated from by providing accurate timing information. The start counter can also be used for the time-of-flight when no other end-time information is available. The start counter is a part of the level-one trigger that requires timing coincidence with other GlueX detectors. The required coincidences

reduces the rate of triggers from electromagnetic and hadronic interactions to a level acceptable for the data acquisition (DAQ) software to readout and write. The DAQ can operate with an event rate up to 200 MB/s without incurring excessive deadtime. Additionally, as a part of the level one trigger, the start counter must accept all multiparticle exotic meson candidates produced above the beam energy of 8 GeV. The start counter was designed to operate at photon intensities of up to 10^8 photons per second in the coherent peak region ($E_\gamma = 8.0 - 9.0$ GeV) and has a timing resolution of ~ 300 ps. The ST provides successful identification of the correct electron beam buckets with 99% accuracy [13]. Lastly, the start counter is comprised of 30 scintillators (Figure 2.10), each 5 mm thick, formed into a cylindrical array that tapers towards the beamline on the downstream end. The taper is utilized to increase the solid angle coverage.

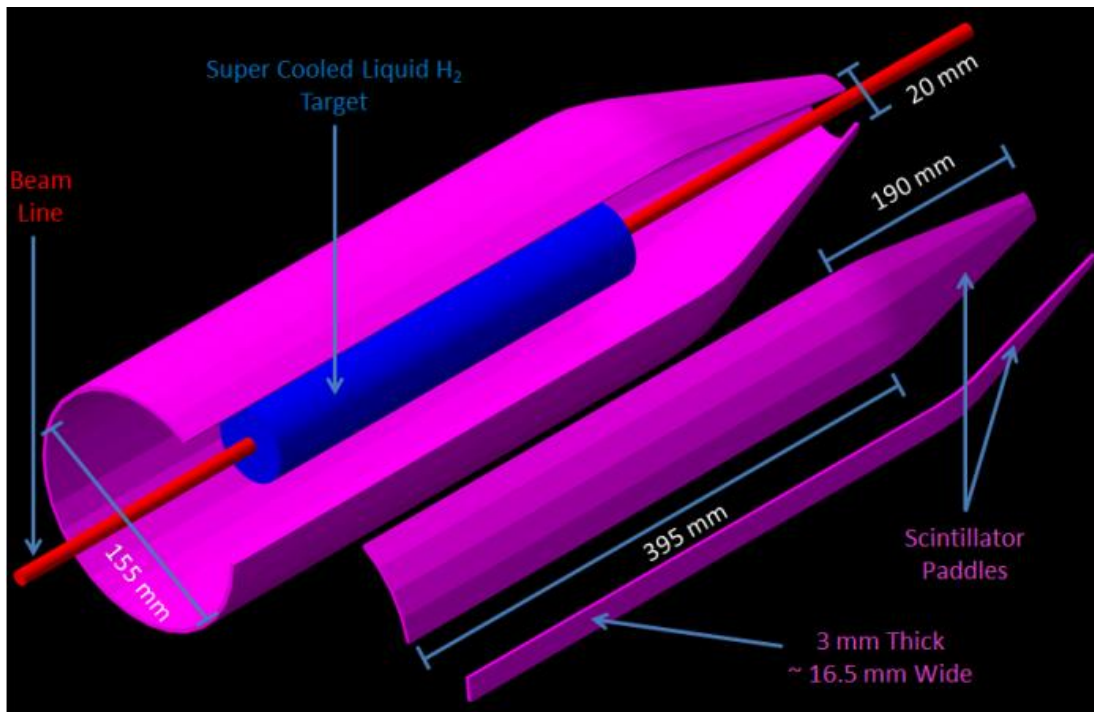


Figure 2.10: Drawing of start counter surrounding LH_2 target, tapering toward the beamline on the downstream side.

2.9 Drift Chambers

2.9.1 Central Drift Chambers

The central drift chamber (CDC) is within the superconducting solenoid magnet and surrounds the start counter. The CDC's purpose is to track charged particles created after the collimated photon beam interacts with the liquid hydrogen target. The CDC can track charged particles with momenta as low as 0.25 GeV/c and identify low-momenta protons by energy loss [11]. To achieve charged particle tracking, the CDC contains 28 layers of 1.5m long straw-tubes arranged in a cylinder, 3522 in total (Figure 2.11).

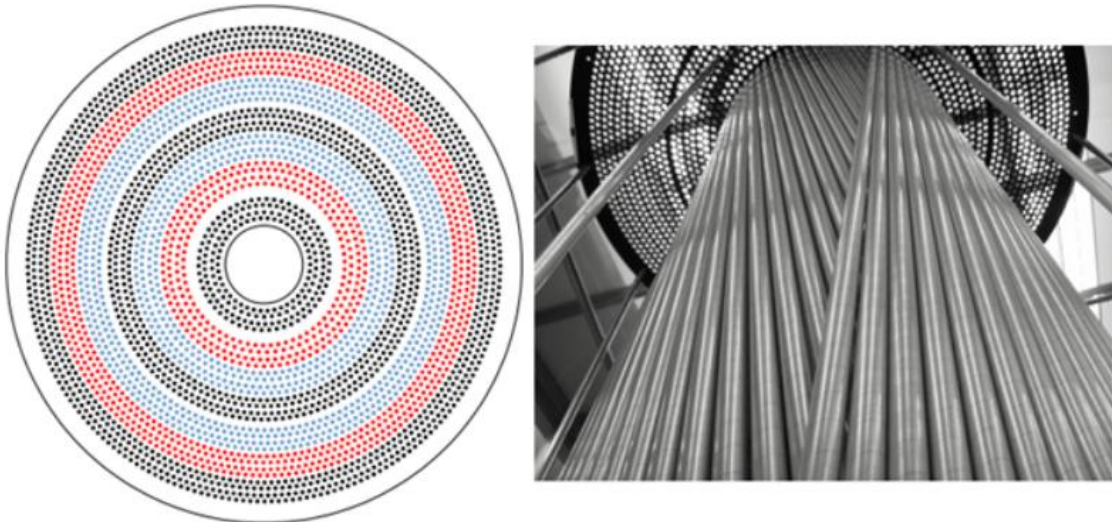


Figure 2.11: The CDC endcap straw-tubes layout is shown on the left, and the CDC partially filled with straw tubes is on the right.

The CDC provides position measurements for charged tracks with an expected position resolution of 150 μm . The CDC also yields timing and dE/dx measurements, obtained from a field programmable gate array that includes an analog to digital converter (ADC). Lastly, the CDC has polar angle coverage from 29° to 132° [11].

2.9.2 Forward Drift Chamber

The forward drift chamber (FDC), shown in Figure 2.12, consists of 24 disc-shaped drift chambers each 1 m in diameter. The FDC resides in the bore of the spectrometer magnet downstream of the CDC and upstream of the TOF detector. The drift chambers are grouped in four packages of six closely placed detectors each rotated 60 azimuthal degrees with respect to the previous chamber. Individually, each of the 24-drift chamber consists of three layers consisting of an anode wire plane packed between two cathode wire planes as seen in Figure 2.13 [11].



Figure 2.12: Fully constructed FDC shown outside of the superconducting solenoid magnet.

The FDC assists in distinguishing multiple charged-particle tracks in the high-particle-density forward region. To aide in multiparticle track separation, additional cathode strips are used on both sides of the wire plane resulting in a space point on the track from each chamber. The FDC registers partial charged track coverage from polar angles of 1° and up to 20° [11].

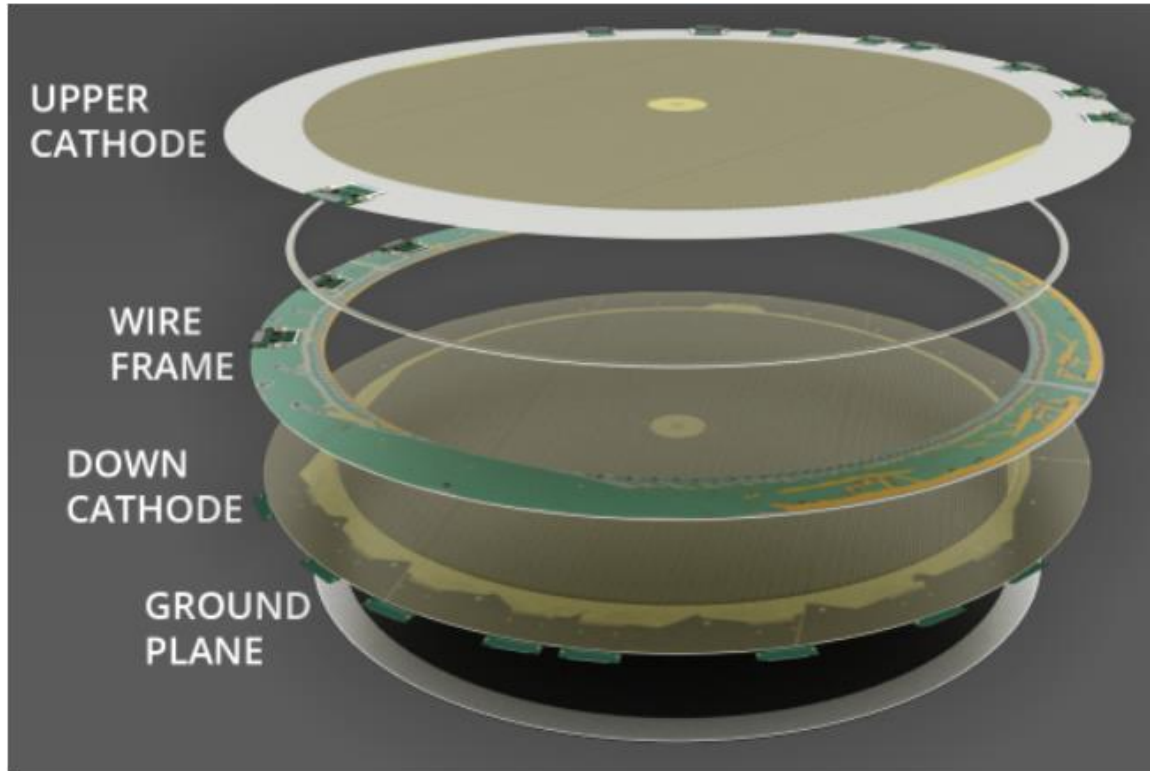


Figure 2.13: Individual FDC package. From bottom to top, the FDC package starts with a ground plane followed by a down cathode, wire frame assembly and topped off with an upper cathode layer.

2.10 Barrel Calorimeter

The barrel calorimeter (BCAL) incapsulates the CDC, FDC and target within the super conducting solenoid magnet. The BCAL is responsible for detecting, identifying and measuring the total energy of both charged and neutral particles. The BCAL reconstructs the photons from the decays of particles such as π^0 and η 's. The BCAL

utilizes 48 trapezoidal modules, each 3.9 m long, formed into a cylindrical geometry having an inner diameter of 1.3 m and outer diameter of 1.8 m. The BCAL has a polar acceptance between 11° and 126° with each module covering an azimuthal sector that extends 7.5° . A module consists of approximately of 185 layers and 15,000 scintillating fibers [11]. As seen in Figure 2.14, the light generated in the fibers is collected by light guides at each end of the module, which send the light to silicon photomultipliers. Silicon was used in the photomultiplier tubes because of the insensitivity of silicone to magnetic fields [11].

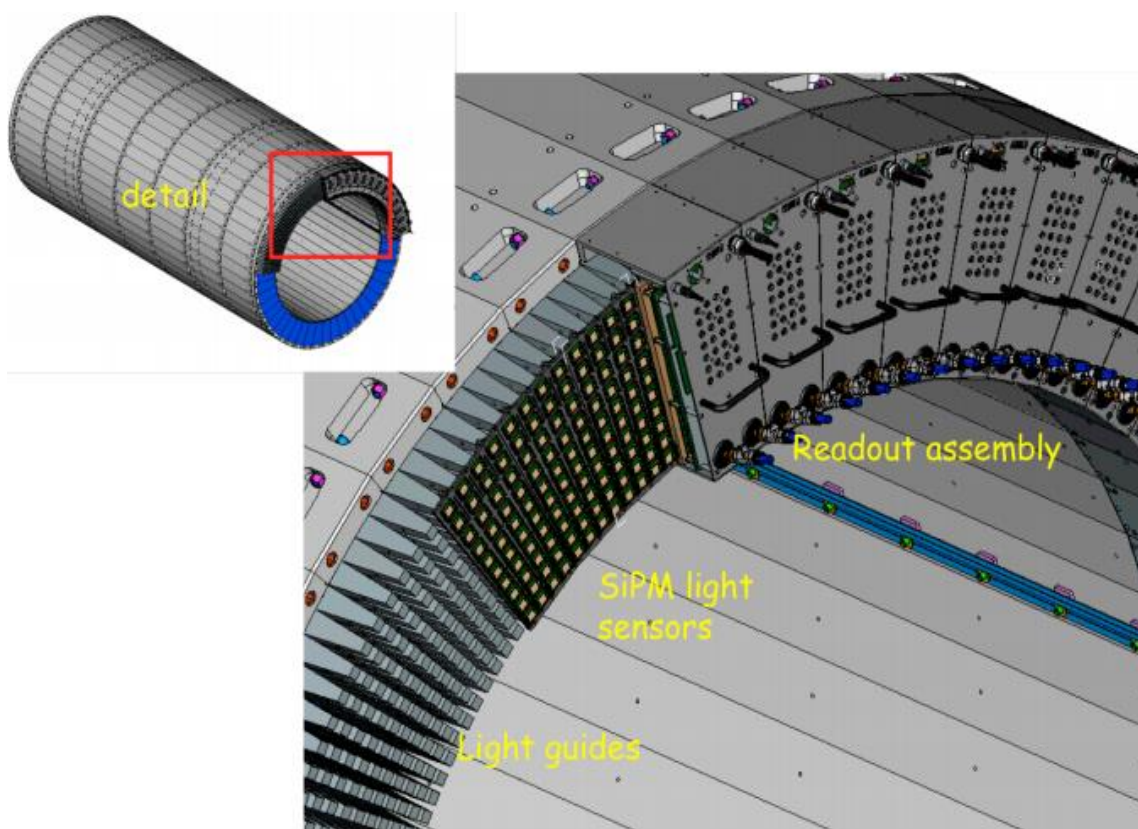


Figure 2.14: 3-D model of BCAL readout system, showing the light guides, silicon photomultipliers and the readout system.

2.11 Time of Flight

Downstream from the FDC is the time of flight (TOF) detector. The purpose of the TOF detector is to aid in charged-particle identification through measurement of the timing information required to determine the velocity of particles traveling between the target and TOF detector. The TOF is 5.5 m downstream from the center of the target and consists of 84 vertical scintillator paddles antecedent to 84 horizontal scintillator paddles. Each scintillator paddle of the TOF has a light guide affixed at each end, coupled to a photomultiplier tube. The TOF detector provides a coverage of 252×252 cm^2 , with a 12×12 cm^2 hole for the beamline (Figure 2.15). The TOF detector has polar angle acceptance for charged tracks between 0.6° and 13° [11].

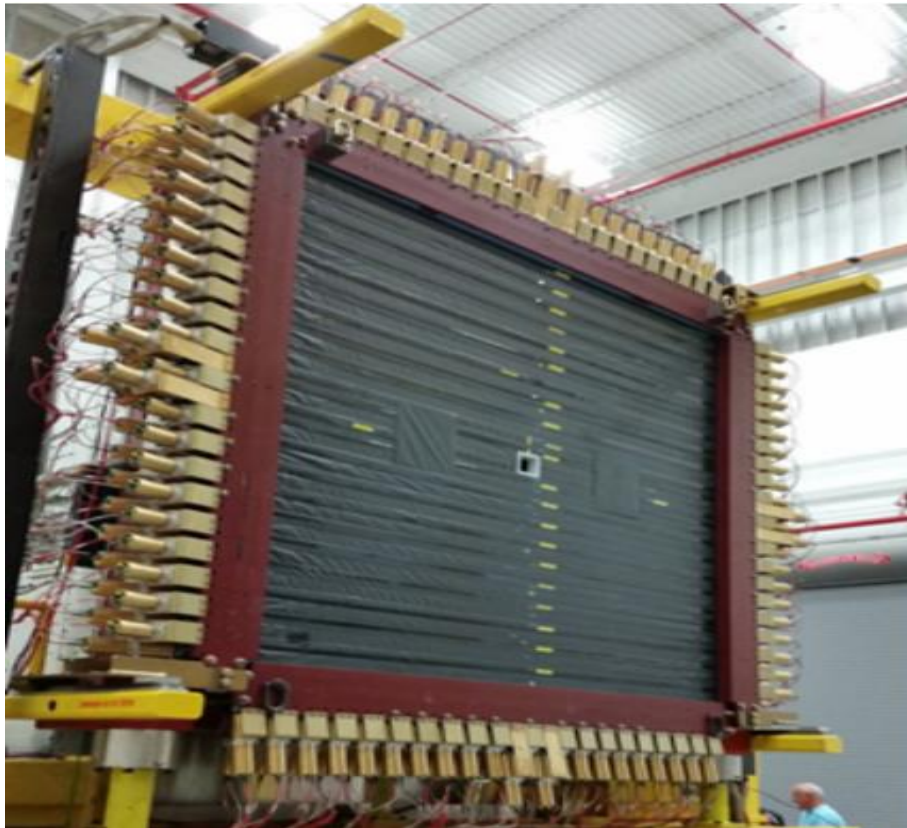


Figure 2.15: A fully constructed TOF Detector with a 12×12 cm^2 cutout for the beamline.

2.12 Forward Calorimeter

The Forward Calorimeter (FCAL), as seen in Figure 2.16, is the detector that is the furthest downstream. The FCAL, like TOF, is orthogonal to the beamline with a planar geometry. FCAL provides a fast energy sum that is used as a part of the level one trigger system. FCAL contains 2800, $4 \times 4 \times 45 \text{ cm}^3$ lead glass blocks stacked in a circular array, with each block connected to a photomultiplier tube. The FCAL measures forward-going particles with a polar angle coverage between 1° to 11° [11]. As stated earlier, the purpose of this detector is to detect and measure forward going photons from the decay of π^0 and η 's to aide in the reconstruction of exotic states.



Figure 2.16: Fully constructed FCAL with 2800 lead blocks exposed.

2.13 Detection of Internally Reflected Cherenkov (DIRC)

The most recent installation to the Hall-D experiment is the DIRC detector, that resides upstream of both the TOF and FCAL detectors and downstream of the spectrometer magnet. The DIRC consists of two parts, the first detects the signal, and the latter collects the signal by multi-anode photomultipliers.

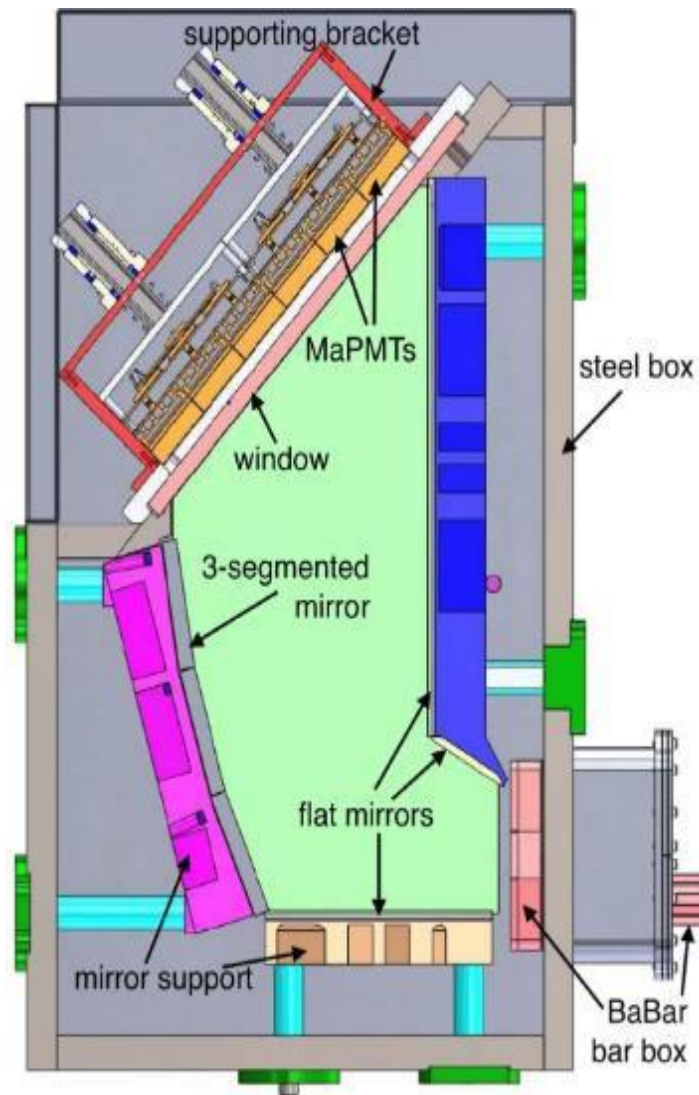


Figure 2.17: Cross section of photon camera. The BaBar pads slide into the bottom and the light is bounced into the MaPMT.

The detection of the signal is by four BaBar (BaBar is the name of an experiment and collaboration. BaBar refers to the b/b-bar system of mesons produced at SLAC National Accelerator Laboratory). The BaBar DIRC detectors are 12 decommissioned, synthetic fused silica bars. Each pair of DIRC detectors are connected to a compact photon camera. The cross section of the photon camera is pictured in Figure 2.17. The set of detectors above the beam have the photon camera on the left end of the BaBar bars while the set below the beam has the photon camera on the right. The photon camera is filled with distilled water and coupled to an array of Multi-Anode PMT's that ultimately read out the cameras [14]. The Cherenkov radiation is expanded and imaged on a pixelated photodetection plane. The resulting pattern provides information regarding the velocity of the charged particle [14].

The TOF detector has pion-kaon momenta separation up to 2.0 GeV/c, but with the installation of the DIRC detector, the pion-kaon separation will move up to 4.0 GeV/c [14]. Charged particles emit Cherenkov radiation when inside the fused silica, and a fraction of the light cone is trapped within the radiator and transported to the photon camera.

Chapter 3

DATA SET

3.1 Run period

The data used in this dissertation comes from the spring and fall 2018 run periods. Roughly 22 percent of the time was run with each orientation of the incident photon polarization at $0^\circ/45^\circ/90^\circ/135^\circ$ relative to the floor, with eight percent dedicated for special normalization runs. The remaining four percent of data acquisition was attributed to dead time. The combination of spring and fall 2018, resulted in 223 billion events in total, where 145 billion events were collected in spring and 78 billion collected in the fall [15].

Collectively, by 2018 GlueX collected 80 percent of the phase one GlueX dataset. Future dataset will use the improved kaon pion separation from the DIRC detector for particle identification. With the improvements emanating from pion kaon separation, future datasets should be very valuable in the reconstruction of additional excited cascades due to a reduction in misidentified pions and kaons.

3.2 Beam Photons

Determining the correct initial state photon coming from the correct beam bunch is not always possible. Many photons are created through the coherent bremsstrahlung process (described in section 2.3) and are consistent with other reactions in the GlueX

spectrometer. Physically, there could only be one photon that causes the reaction. To begin identifying the initial state photon we select the correct beam bunch delivered to the hall.

The electron beam is delivered by CEBAF every four nanoseconds. The time when photons arrive from the tagger hall is well known and referred to as the RF time [11]. The experiment also uses beam-time, where beam-time is the time in which the reconstruction converges onto a shared vertex time. The vertex time is derived by taking all final-state particle momentum and timing information to backtrack the decay to a common point in space-time. The difference between the beam-time and RF time should be centered at zero and is used to determine the correct beam bunch. Figure 3.1 shows a plot of the difference between the RF time and the beam time. The large structure centered about zero is the in-time peak (signal) with four smaller out-of-time (sideband) peaks. The signal peak centered at zero, has boundaries at -2.004 ns and 2.004 ns, meaning everything outside of this time zone is considered to be out-of-time.

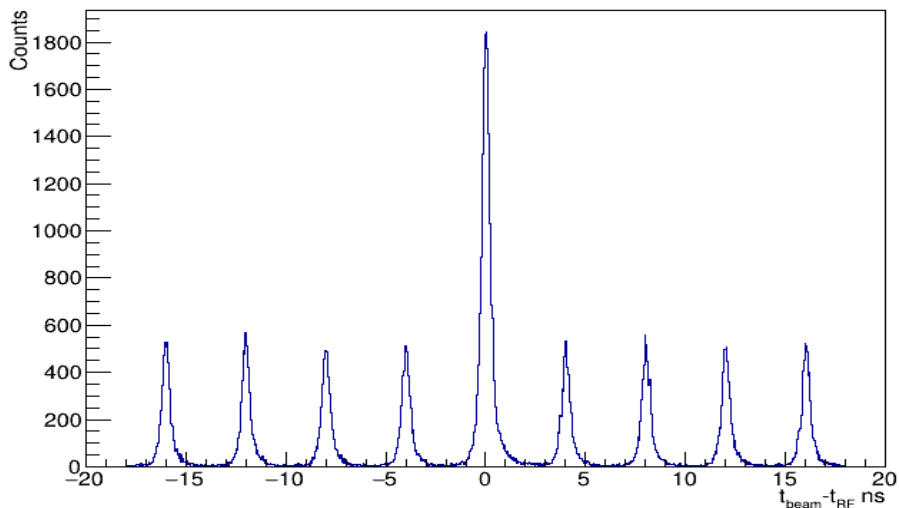


Figure 3.1: The sideband and signal peak structure using beam time and RF-time with a confidence level above 10^{-4} .

There are accidental coincidences underneath the central signal peak that must be compensated for in determining the cross-section. The process is called side-band subtraction. To complete the sideband subtraction, the out-of-time events are weighted by a factor of $-1/N_b$, where N_b are the number of beam bunches used. In my analysis, there are 4 sidebands on each side of the central in-time signal peak, totaling eight side bands.

3.3 Photon Flux

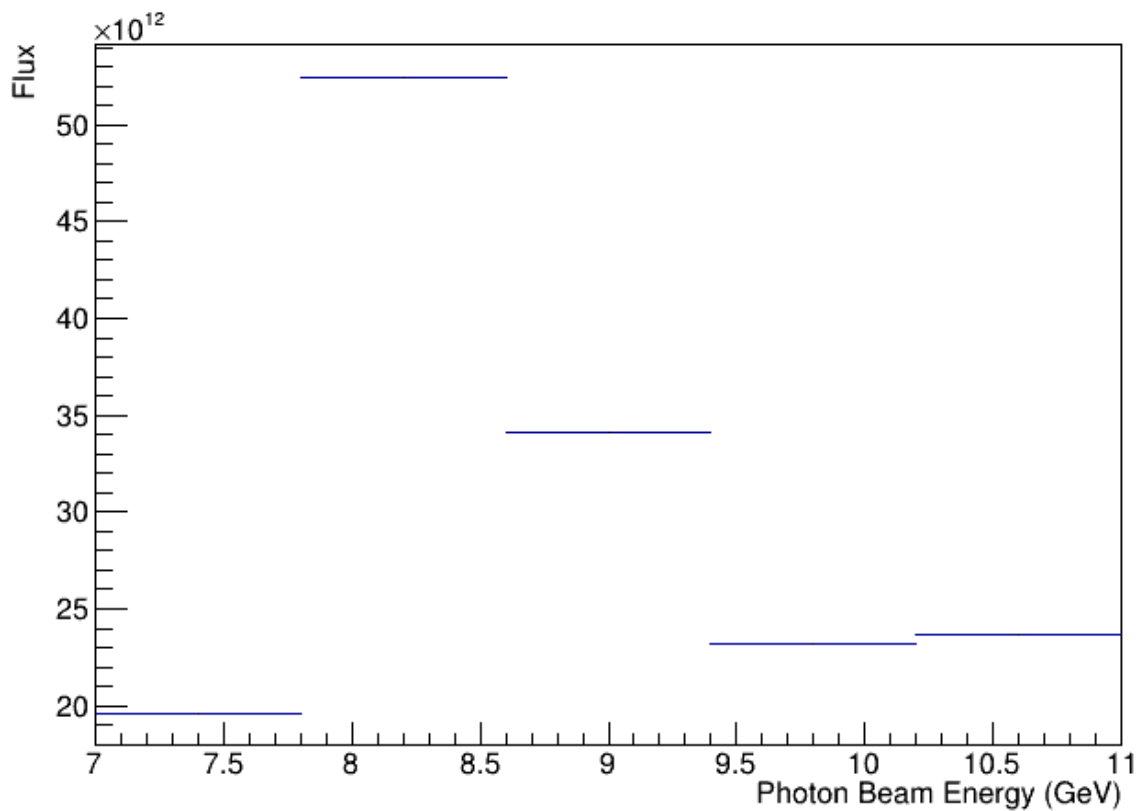


Figure 3.2: The tagged photon flux from the pair spectrometer.

The tagged flux of photons, as seen in Figure 3.2, is used in the cross-section measurement and determined from the tagged flux from the pair spectrometer. The term “tagged” refers to the photon energy being determined from the tagger hodoscope (or

microscope), given the known CEBAF delivered electron beam energy. The number of photons tagged in each bin are obtained by computer scripts that access the CCDB (Calibration Database). The flux determination utilizes run numbers that are associated with physics production runs. The flux determination for the spring 2018 run period, for which the $E^{*-}(1530)$ cross section was measured, consists of 544 production runs.

3.4 Number of Scattering Centers per Unit Area

The total mass of protons incident to the beam can be expressed as, $\rho_{LH_2} \cdot A \cdot l$, where ρ_{LH_2} is the density of liquid hydrogen in the target, A is the cross-sectional area of the collimated photon beam, and l is the length of the target. Dividing by the molar mass of hydrogen, M_{H_2} , and multiplying by Avogadro's number, N_A , gives the total number of scattering centers presented to the cross-sectional area of the photon beam. The area of the beam is difficult to determine, however by dividing out the area we have the total number of scattering centers per unit area, τ :

$$\tau = \frac{\rho_{LH_2} \cdot l \cdot N_A}{M_{mH_2}}$$

The density of liquid hydrogen in the target is 0.0734 g/cm^3 , from the geometry presented above τ is $1.32 \times 10^{24}/\text{cm}^2$ or 1.32 per barn.

Chapter 4

EVENT SELECTION

4.1 Kinematic fitting

Kinematic fitting is a technique employed by the GlueX collaboration to improve the resolution of experimental data [16]. There will always be errors associated with measurements (e.g. momentum, timing, position) and these measurements will have distributions around a central value. Kinematic fitting uses vertex position along with conservation of energy and momentum, to constrain the measured values. More specifically, the kinematic fitting technique modifies the measured quantity within error, forced to obey conservation of energy and momentum. Mathematically, the kinematic fitting is done by an iterative routine of χ^2 minimization utilizing Lagrange-multipliers

$$\chi^2 = \epsilon^T V^{-1} \epsilon + 2\lambda^T F = 0,$$

with $\epsilon = \eta - y$, where epsilon (ϵ) is the difference in the vector of measured quantities before (η) and after (y) the kinematic fit, V is the covariance matrix, F is a vector of the constraints and λ is a vector of Lagrange multipliers. The first term, $\epsilon^T V^{-1} \epsilon$, improves the resolution of the particle 4-momenta while the second term, $2\lambda^T F$, contains constraints for a specific reaction hypothesis. The second term can help reject events that do not match the reaction hypothesis and is not limited to energy and momentum conservation. Other common constraints include vertex information, the invariant mass of reconstructed

particles and the mass of missing particles. For the kinematic fitter to work the elements of the covariance matrix, a $mN \times mN$ symmetric matrix (N is the number of particles and m the number of measured variables) must be known. To analyze how well the kinematic fitter is addressing the hypothetical reaction, we have the confidence level. The confidence level is a “goodness of fit” quantity that relates how well the data and hypothetical reaction agree. The confidence level (CL) is defined as:

$$CL = \int_{\chi^2}^{\infty} f(z, n) dz,$$

where $f(z, n)$ is the χ^2 probability density function with n degrees of freedom (NDF). CL is a measure of the probability that a χ^2 from the theoretical distribution is greater than the measured χ^2 obtained from the fit.

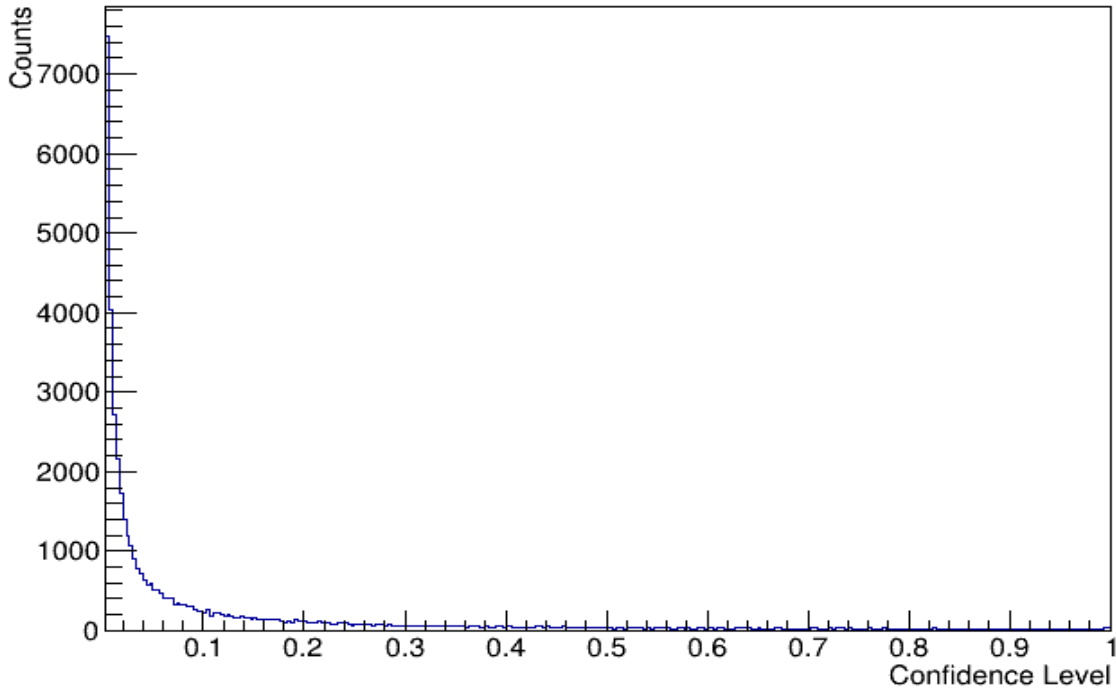


Figure 4.1: Confidence level distribution for the reaction $\gamma p \rightarrow K^+ K^+ \Xi^- \pi^0$.

The confidence level distribution is relatively flat distribution, except around zero, where the distribution peaks. Figure 4.1 shows the confidence level for the $\gamma p \rightarrow K^+ K^+ \Xi^- \pi^0$ reaction. The events with an incorrect hypothesis level are associated with low confidence level. When the data files are cooked, the mass of identified charged particles that are directly measured can be constrained to the PDG masses. The additional constraints help purify the signal, improving the resulting fitted values and filtering out events that do not fit the hypothetical reaction.

4.2 Reconstruction

4.2.1 $\Xi^- \pi^0$ Decay Channel

The photoproduced charged cascade Ξ^{*-} (1535) can be produced in the following decay chain:

$$\gamma p \rightarrow K^+ Y^*,$$

$$Y^* \rightarrow K^+ \Xi^{*-},$$

$$\Xi^{*-} \rightarrow \pi^0 \Xi^-,$$

$$\Xi^- \rightarrow \Lambda \pi^-, \text{ and}$$

$$\Lambda \rightarrow \pi^- p.$$

In the data files for this reaction, the Lambda and neutral pion are kinematically fit to their PDG masses. To begin event reconstruction and refine the excited cascade peak, a generic baseline confidence level cut was implemented to remove much of the background associated with low confidence-level events. To begin the analysis, a 10^{-4} blanket

confidence level cut was applied to all events. The choice of analysis cut will be further analyzed later. For particle identification, β vs momentum plots show clear particle identification signatures, but the resolution of different detector elements must be investigated in determining how effectively they can reconstruct the different particles. The different detector elements that can be accessed are the ST, BCAL, FCAL, TOF, and NULL (Null events are defined as events that do not have a defined flight time). With a confidence level cut, Figure 4.2 shows the β vs p plots for the start counter and time-of-flight detector.

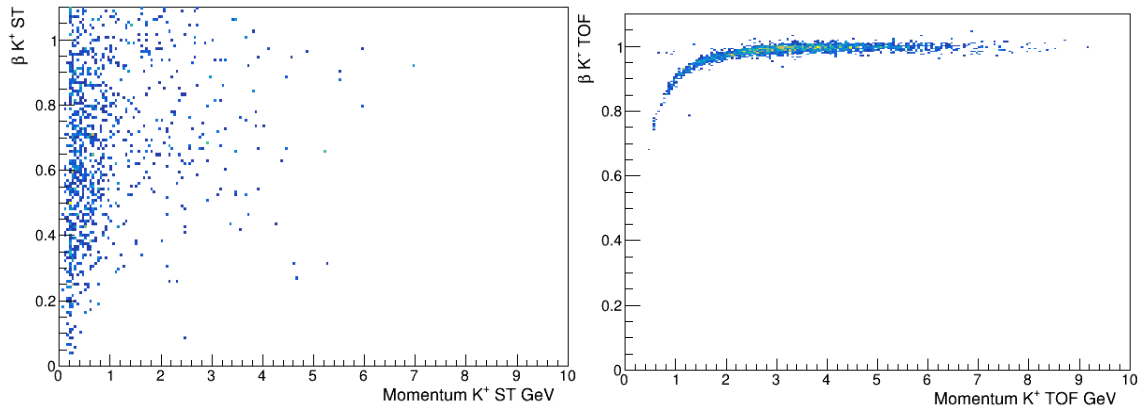


Figure 4.2: Plots of β vs p for a kaon. The plot on the left is for kaons that have time of flight information only from the ST. The plot on the right is for the case where time-of-flight information is taken from the TOF detector.

Referring to Figure 4.2, the TOF detector (right) has the appropriate curvature for a kaon and has a limited amount of pion or electron contamination. The ST plot (opposite the TOF plot with identical axes) only contains events for the kaons that use the ST for the time of flight. As evident from the ST plot given on the left side of Figure 4.2, the lack of structure cannot reliably help verify the particle identification and are excluded from the

analysis. Additionally, 113 NULL (no flight time) events were also excluded from the analysis.

With the initial confidence level and detector cuts applied, the next step is to reconstruct the negative ground state cascade. The $\Xi^-(1320)$ decays into a $\Lambda(1115)$ and π^- , while the $\Lambda(1115)$ and π^- are both constrained to their PDG masses, any resulting particle constructed from them are not necessarily constrained. In Figure 4.3 is a plot of the invariant mass of the $\Lambda\pi^-$ system. There is a clear $\Xi^-(1320)$ peak. Using a Gaussian for the signal and first order polynomial for the background, the peak center is found to be 1.322(1) GeV with a standard deviation of 4.7(1) MeV, resulting in a full width at half max (FWHM) of 11(3) MeV. There are background events underneath and outside of the $\Xi^-(1320)$ peak. To reduce the Ξ^- background, before the reconstruction of the excited cascade, Ξ^{*-} , the unnecessary events outside the peak region should be cut. Thus, the invariant mass of the $\Lambda\pi^-$ system was required to be from 1.31 to 1.34 GeV.

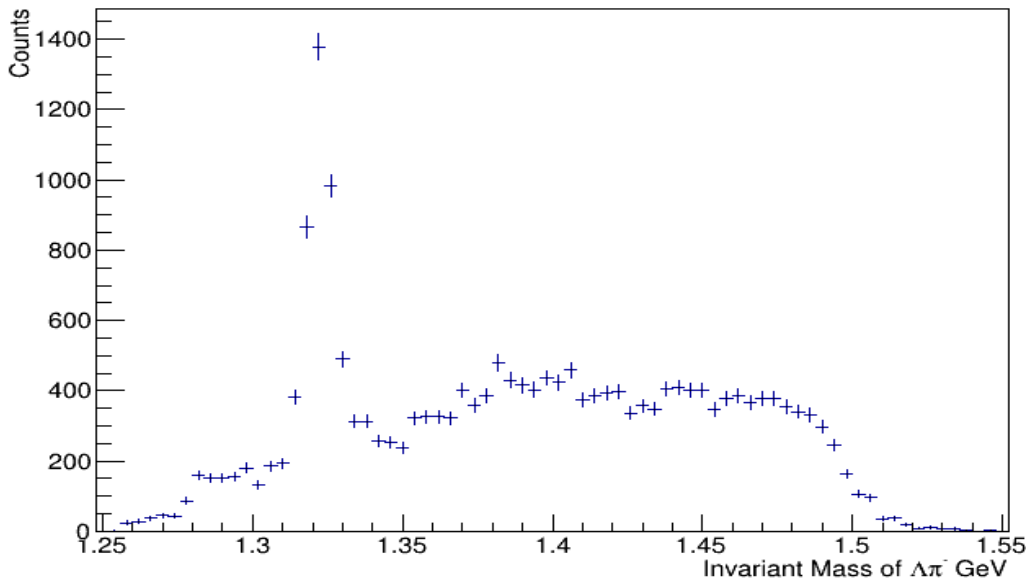


Figure 4.3: The invariant mass of the $\Lambda\pi^-$ system in GeV.

The final step in the reconstruction of the $\Xi(1530)$ is the addition of a neutral pion. The neutral pion is kinematically constrained to its PDG mass. Figure 4.4 is counts versus the invariant mass of the $\Xi\pi^0$ system and shows another clear cascade peak. With a Voigtian function (convolution of a Breit-Wigner and gaussian) for the signal, and the background modeled by an argus function (a probability distribution that contains a phase-space cutoff), the cascade is centered at 1.536(1) GeV with a Breit-Wigner width of 13(1) MeV.

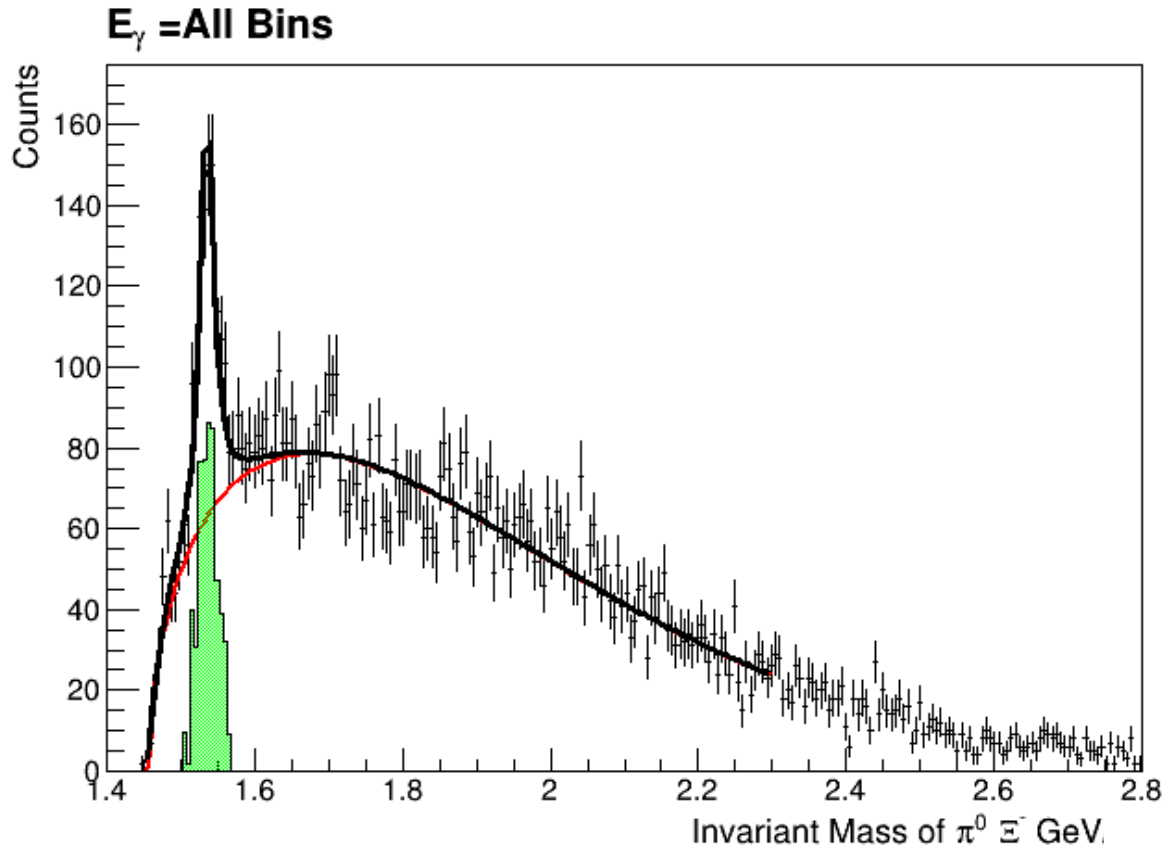


Figure 4.4: The invariant mass of the Ξ^{*-} in GeV

Additionally, Figure 4.4 has evidence of another excited cascade, the $E(1690)$, that couples to this channel. An analysis cut for reducing the accidental background associated with the final state particles arising from K^* mesons was implemented. The final state contains: $p, K^+, K^+, \pi^-, \pi^-, \gamma, \gamma$, where the two photons reconstruct to a π^0 that may not have come from a E^* decay, but instead arose from a K^* decay ($K^{*+} \rightarrow K^+ \pi^0$), causing unwanted background. As can be seen in the plot of the invariant mass of $K^+ \pi^0$ in Figure 4.5, there is a large K^* contamination (mass of K^* is 892 MeV). The peak near the K^* has a center at 894(2) MeV with a standard deviation of 29(2) MeV. The K^* has been cut out of the analysis.

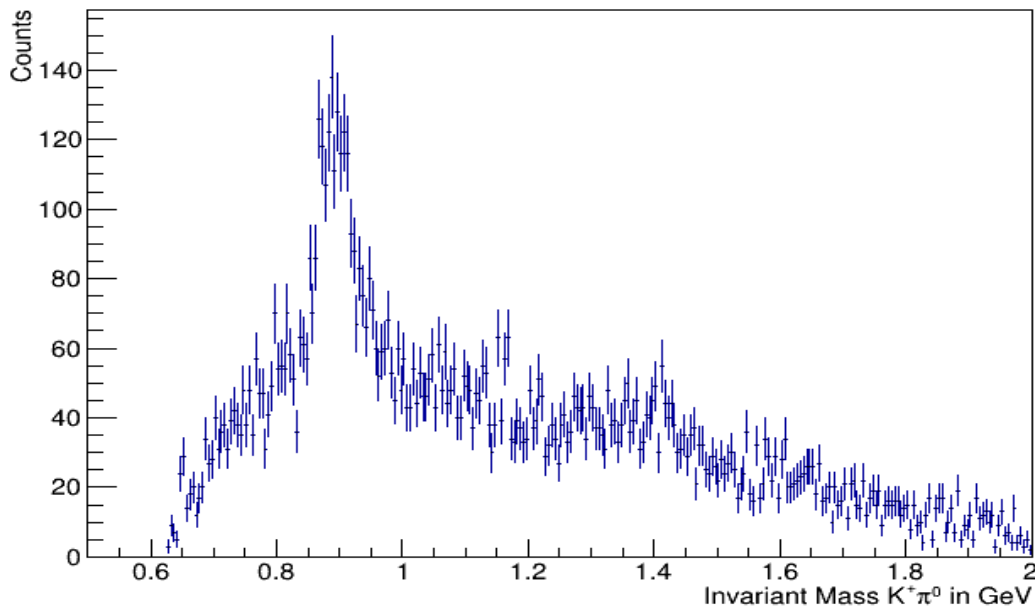


Figure 4.5: K^* contribution of the excited cascade.

Another step in the reconstruction of the excited cascade is revisiting the first analysis cut implemented. The blanket confidence level of 10^{-4} was investigated. The desired confidence level cut minimizes the error in the final cross section measurement. The cross-section is given by

$$\sigma = \frac{Y}{T * \tau * \epsilon}.$$

With the form of the cross-section above, the square of the fractional error in the cross-section measurement will be

$$\frac{\sigma_Y^2}{Y^2} + \frac{\sigma_T^2}{T^2} + \frac{\sigma_\tau^2}{\tau^2} + \frac{\sigma_\epsilon^2}{\epsilon^2}.$$

I defined a figure of merit, FOM, as the fraction error in the signal yield $\left(\frac{\sigma}{Y}\right)$. The confidence interval that minimizes the FOM will be the confidence level used for the entirety of the analysis. The excited cascades were fit as previously described (Voigtian signal with argus background) for various confidence level cuts. Figure 4.6 shows a plot of $\Xi(1530)$ with a minimum confidence level starting at 10^{-7} .

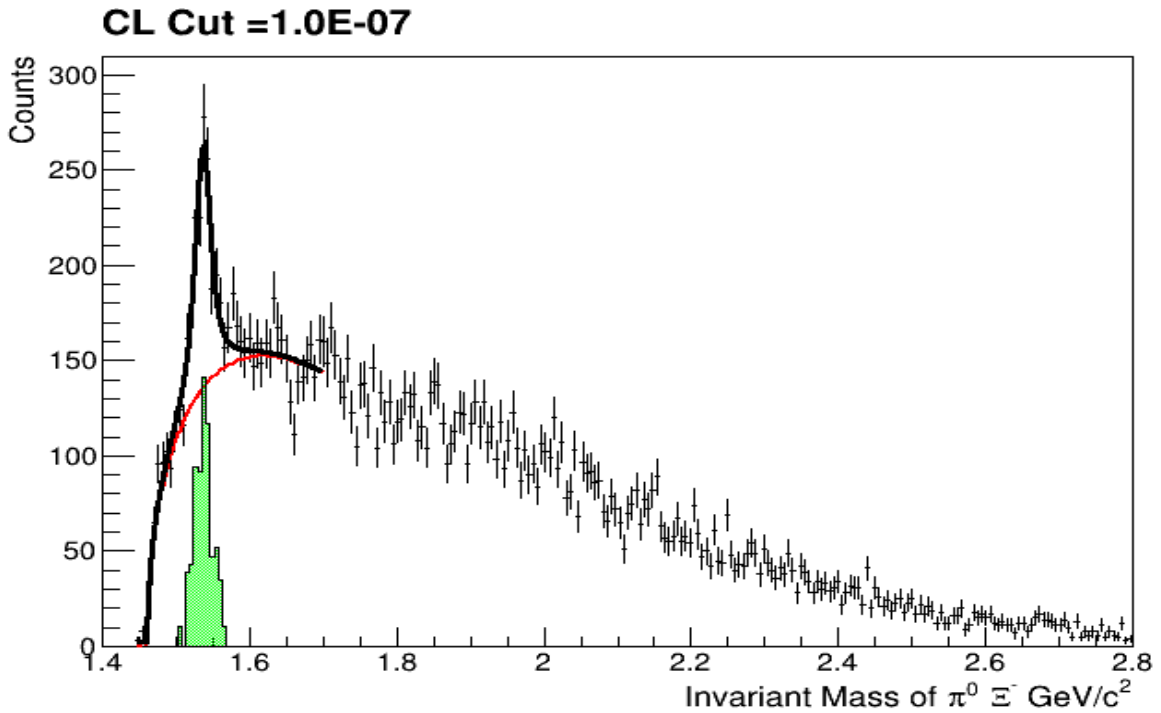


Figure 4.6: A plot of the invariant mass of the $\Xi^- \pi^0$ system for events where the confidence level is greater than 10^{-7} .

In the plot of the FOM against confidence level, there is a degree of stability from 10^{-2} to 10^{-8} . The confidence interval that minimizes the FOM is the same as the initial confidence level cut at 10^{-4} .

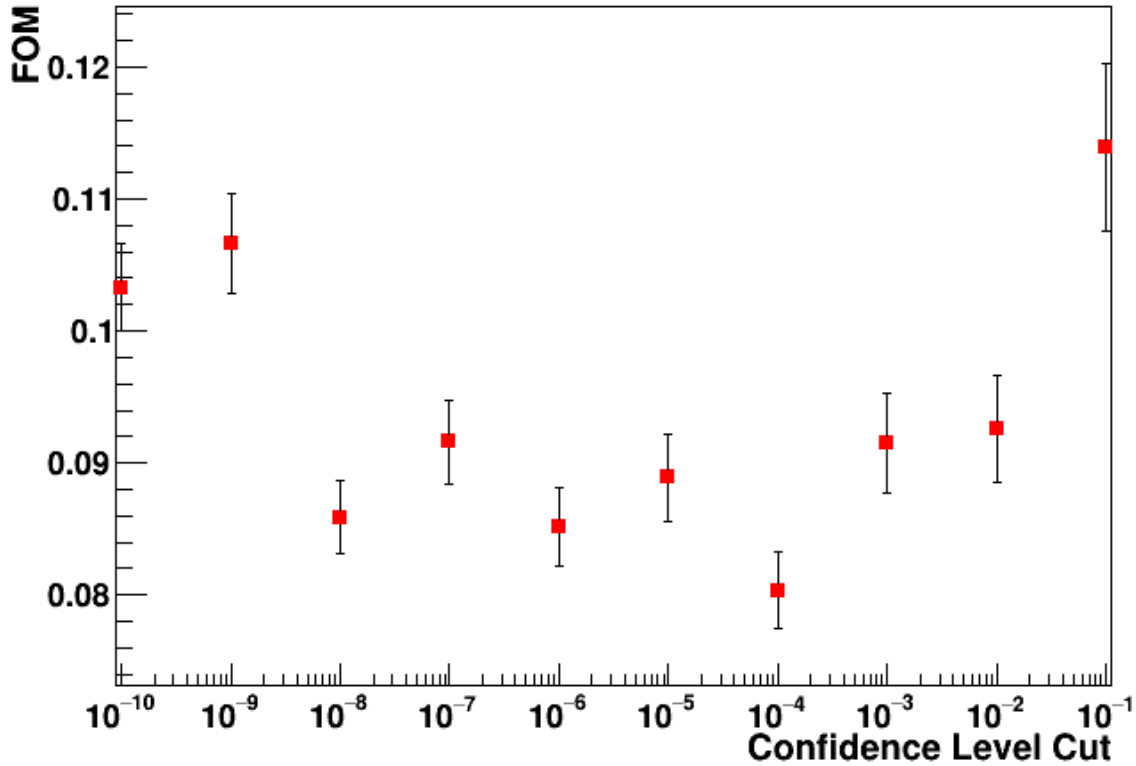


Figure 4.7: A plot of the FOM against the confidence interval.

4.2.2 $K\Lambda$ Decay Channel

The heavily favored (100% [2]) decay channel for the $E(1530)$ is the $E\pi$ mode, but higher mass cascades often couple to the ΣK or ΛK channels. For the purposes of this document, I will be covering the ΛK channel. To begin the reconstruction for this channel, one must begin with the decay chain for this reaction:

$$\gamma p \rightarrow K^+ Y^*,$$

$$Y^* \rightarrow K^+ \Xi^{-*},$$

$$\Xi^{-*} \rightarrow \Lambda K^-, \text{ and}$$

$$\Lambda \rightarrow \pi^- p.$$

In the cooked data, all of the kaons are kinematically constrained to their PDG mass of 493 MeV. To clean up the signal around the lambda baryon peak, an initial confidence level cut of 10^{-4} was implemented.

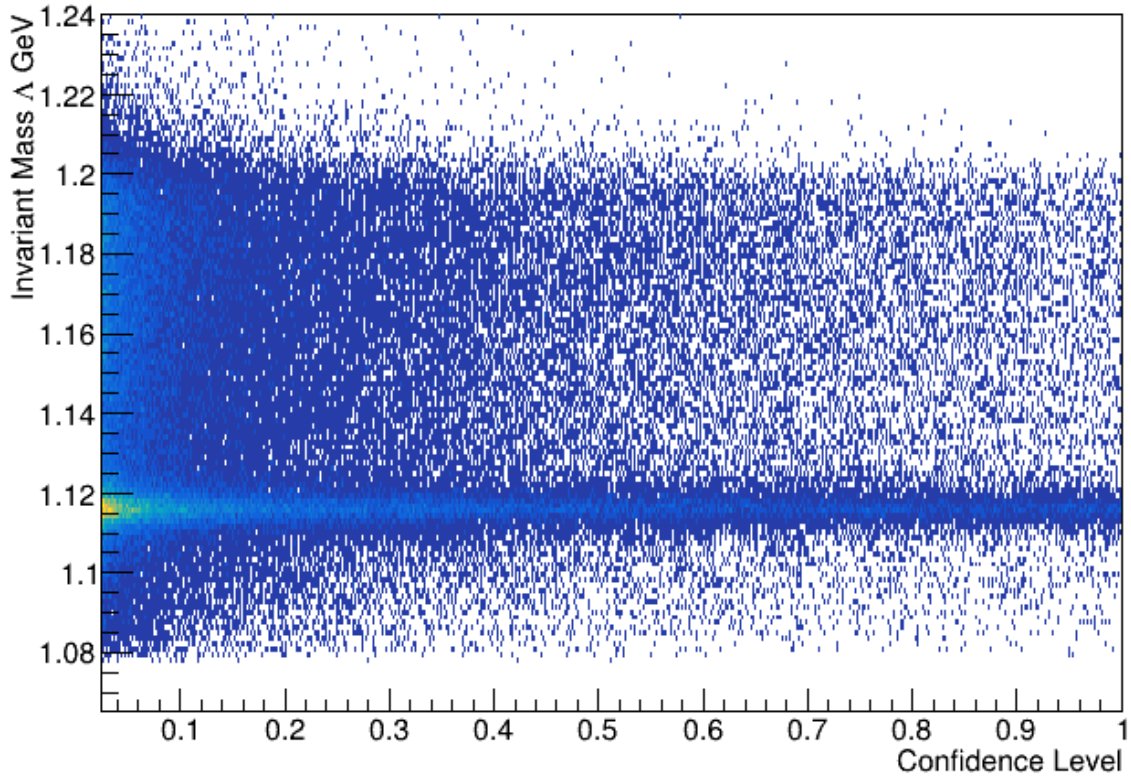


Figure 4.8: Plot of the invariant mass of the lambda baryon plotted versus the confidence level.

In Figure 4.8 we see the invariant mass of the Λ plotted against the confidence level. There is a clear band about the mass of the lambda baryon. Using a gaussian to model the signal and first order polynomial to model the background, the center was located at

1.1159(2) GeV and the standard deviation was 2.71(2) MeV (FWHM 6.38(4) MeV). Events selected for further analysis are within three standard deviations from the center of the Lambda baryon peak (1.107 GeV to 1.124 GeV).

While the confidence level cut should remove much of the background, to further assist in the identification of signal, the background associated with misidentified particles was removed. The list of particles involved in this reaction can be combined to the decay of the ϕ meson. In this case, the list of final state particles is K^+, K^+, K^-, p and π^- .

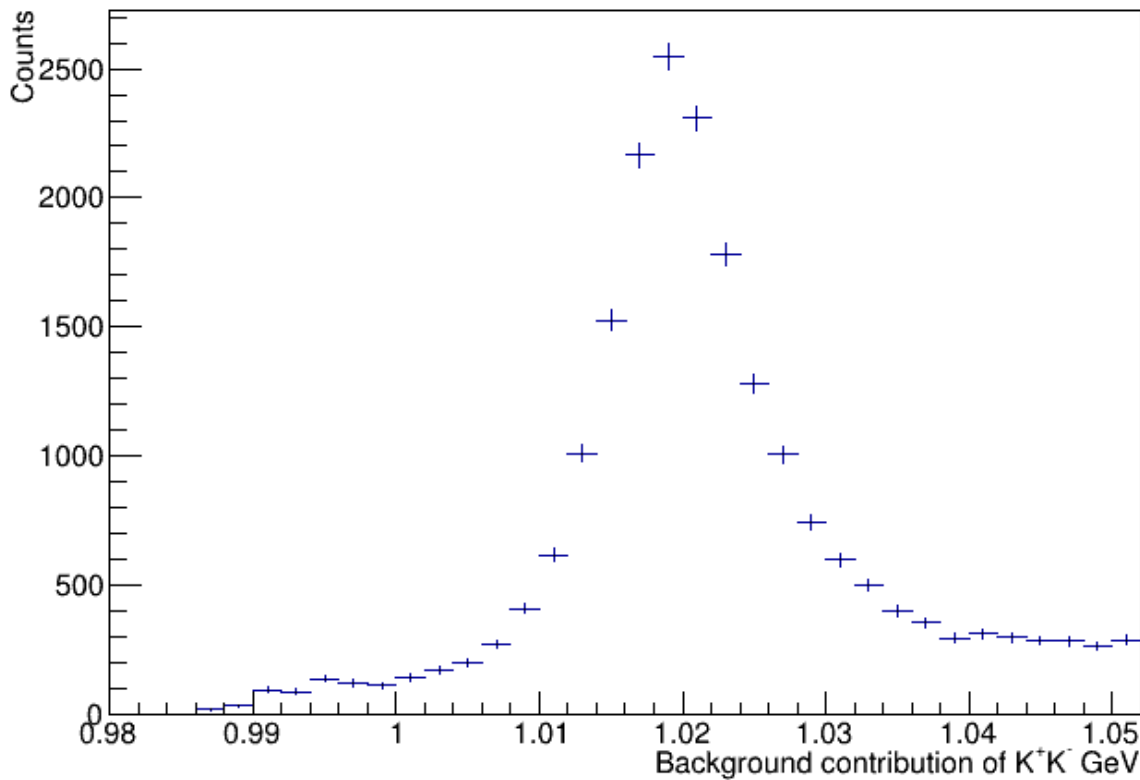


Figure 4.9: Invariant mass of the K^+K^- system in GeV

The ϕ meson, is reconstructed from a combination of K^+K^- and was cut out of the signal that is attributed to the $K^-\Lambda$ system. As seen in Figure 4.9, the ϕ peak formed by invariant mass $K^+ K^-$ is clearly visible. The ϕ peak was fit with a gaussian for the signal

and first order polynomial as the background. The gaussian was centered at 1019.5(6) MeV with a standard deviation of 4.78(6) MeV (FWHM 11.3(2) MeV).

A study on the value to place the confidence level cut was not performed for the $K^- \Lambda$ channel. However, the invariant mass of the $K^- \Lambda$ spectrum was plotted with confidence level cuts in ascending powers of ten to determine the best confidence level cut to use in elevating the cascade peaks above the background. The analysis uses a confidence level above 10^{-2} .

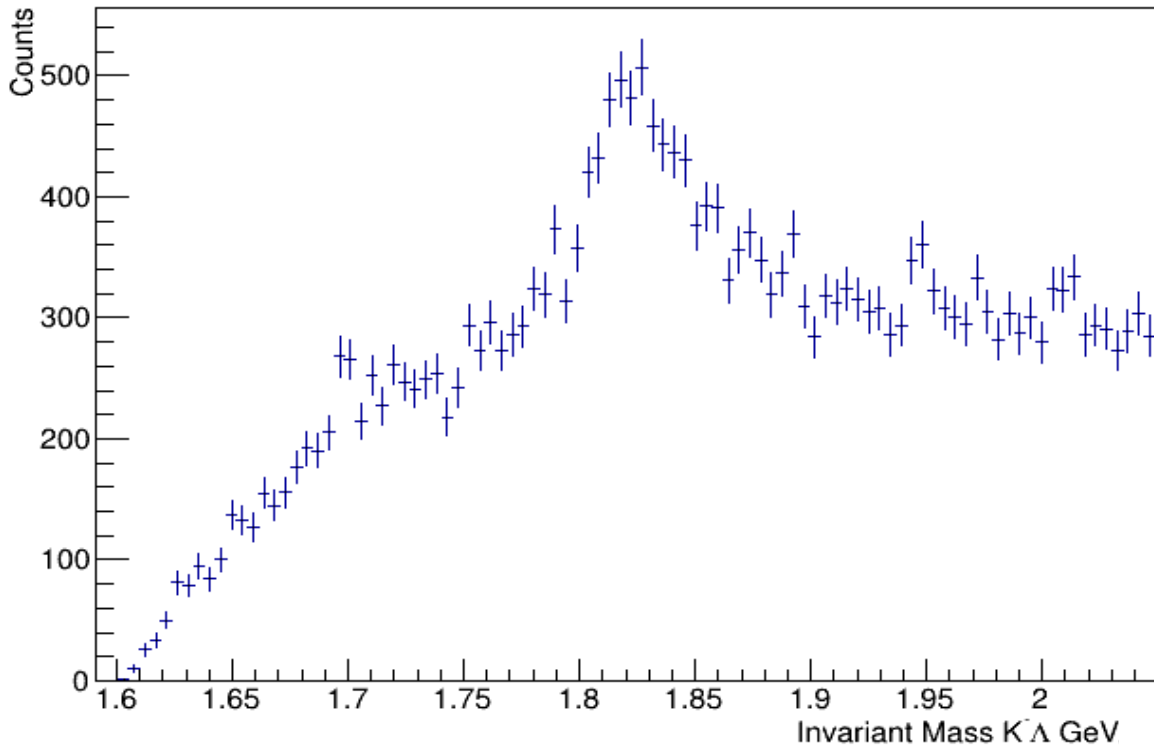


Figure 4.10: Invariant Mass of $K^- \Lambda$ system in GeV.

Figure 4.9 is the invariant mass of the $K^- \Lambda$ system with a confidence level above 10^{-2} . In Figure 4.9 there are three enhancements near known excited cascade states: $E(1690)$, $E(1820)$, $E(1950)$.

4.3 Error Determination

The error determination for the data points in Figure 4.7 are dependent on poisson statistics. Due to reoccurring use of the error propagation, I elaborate on the error determination of background subtracted yields. The signal yield is the difference in the total signal (S) minus the background contribution (B),

$$Y = S - B,$$

From error propagation, the error in the signal yield is given by,

$$\sigma_Y^2 = \sigma_S^2 + \sigma_B^2.$$

Following poisson statistics the variance of a variable K is given by the mean value of K .

Therefore, the error in the signal yield is,

$$\sigma_Y^2 = S + B.$$

Substituting the total signal in terms of the signal yield and background contributions, the variance is

$$\sigma_Y^2 = Y + 2B.$$

The variance is given as the yield plus twice the background contribution and illustrates the importance of reducing background contributions prior to yield extraction.

MONTE CARLO EXCITED CASCADE

5.1 Event generation

In the direct photoproduction of the excited cascade baryon, two strong interactions occur, replacing the two up quarks in the proton into strange quarks. Due to two quark-antiquark pairs being at the production vertex, the direct production of the excited cascades is OZI suppressed. Thus, the more probable production of the cascade baryon is the two-step process seen in Figure 5.1.

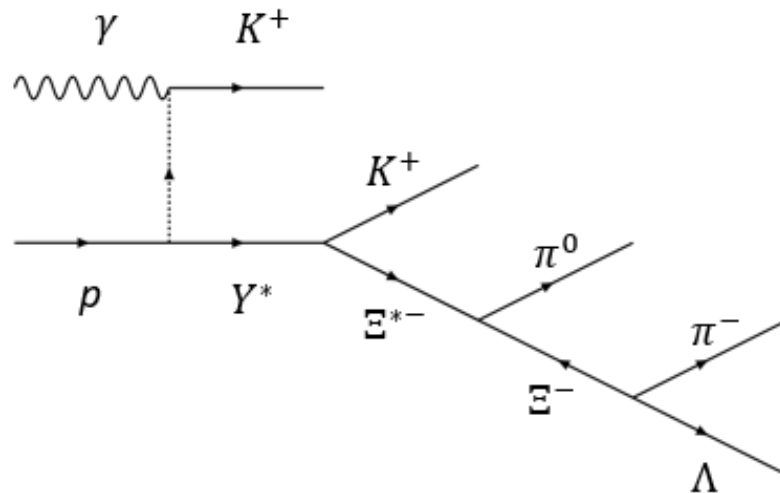


Figure 5.1: Feynman diagram of the photoproduction of the excited cascade.

To generate accurate efficiencies, the Monte Carlo must take into account the two-step process. Little is known about the intermediate hyperon Y^* , but to model the reaction, the bounds on the invariant mass and width are essential. A complication that arises is that

the order of the two kaons involved in the reaction can't be determined in real data. However, since the kaon that couples directly to the incident photon will be emitted more frequently in the forward direction than the second K^+ (from the hyperon decay), I choose the most forward K^+ as the kaon that couples directly to the photon within the real data. With the analysis cuts in place, I plot the polar angle against the momentum of the kaon.

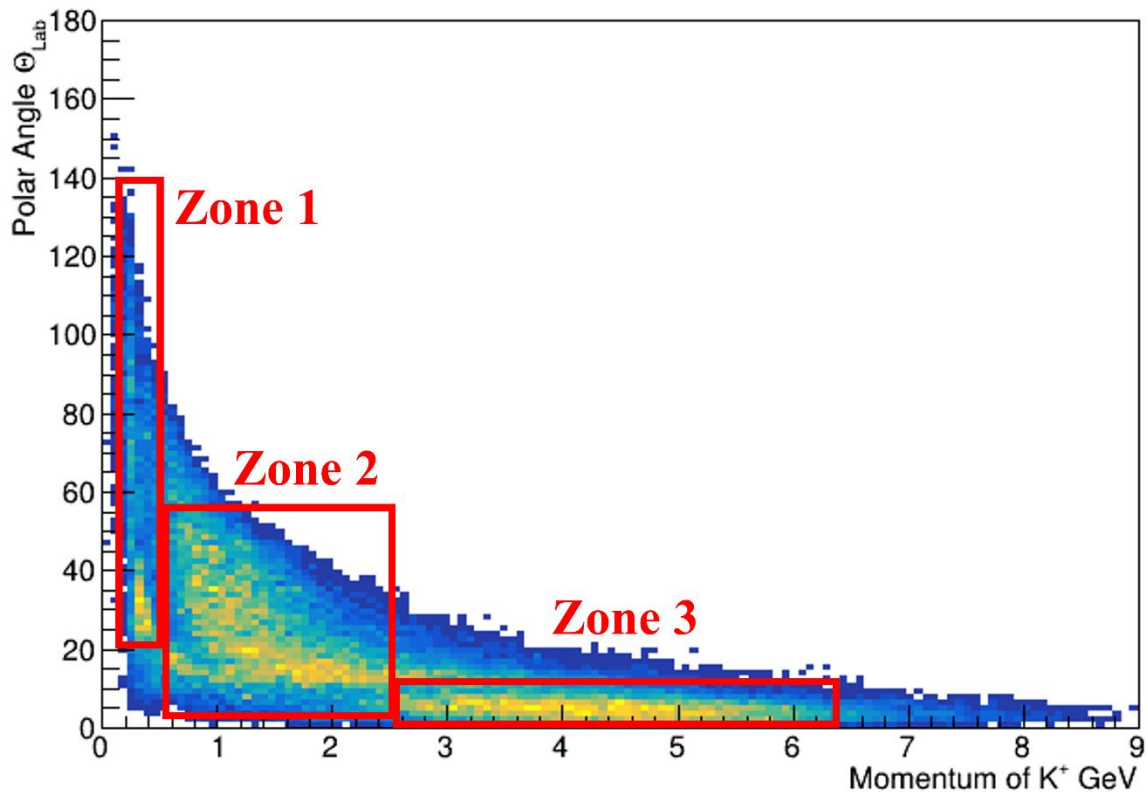


Figure 5.2: Kaon polar angle vs momentum in GeV.

In Figure 5.2, there are three zones having a higher intensity of kaons. The first zone is a low momenta kaon with an intermediate opening angle, zone two houses higher momentum kaons than zone one with lower opening angle, and zone three has the highest momentum kaons with a very small opening angles. During the t -channel process that creates the Y^* , the K^+ associated with the photon vertex is more preferentially linked with

zone three. Taking the K^+ that couples directly to the Y^* as the one with the larger polar angle, I create a plot of the invariant mass of the $Y^* \rightarrow K^+ \Xi^{*-}$. I fit the invariant $\Xi^{*-}K^+$ system using a gaussian signal with a first order polynomial background as shown in Figure 5.3. The center of the gaussian in Figure 5.3 is 2.917(2) GeV with a standard deviation of 0.468(3) GeV.

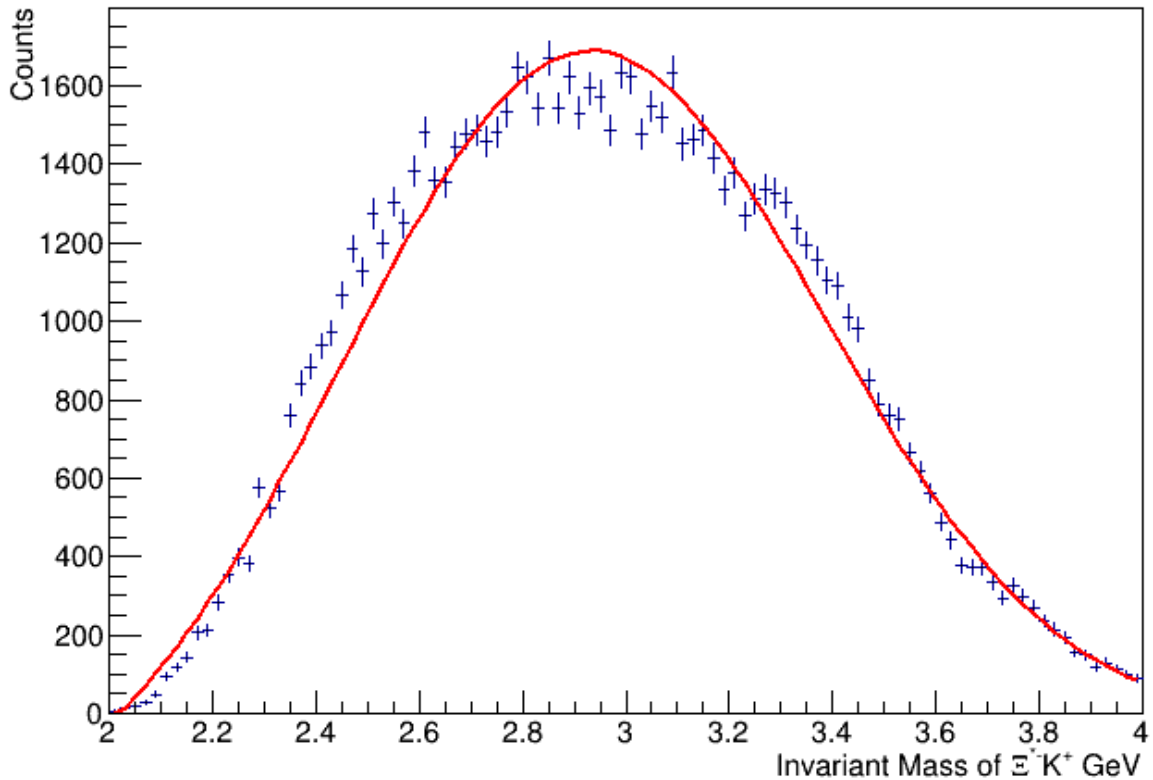


Figure 5.3: Invariant mass of $\Xi^{*-}K^+$ system in GeV.

With that bit of phenomenology out of the way, having the bounds on the intermediate hyperon, one can produce the entirety of the decay chain mentioned early in section 4. Proceeding down the decay chain, the next piece of information that is needed for modeling the kinematics of this reaction is the t -slope. The Mandelstam variable t is defined in two-to-two reactions (see Figure 5.4) as:

$$t = (p_1 - p_3)^2 = (p_2 - p_4)^2 .$$

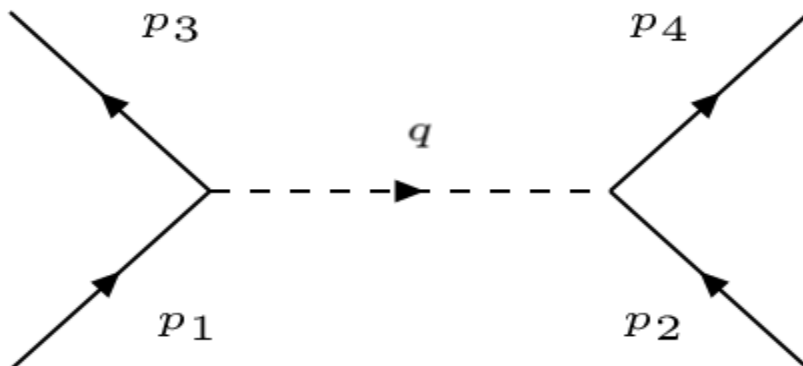


Figure 5.4: Generic Feynman diagram for a t -channel process with time running upward.

Mandelstam variable t , as defined above, is an inherently negative quantity. Assuming the cross section is proportional to $e^{-b|t|}$, one can extract the t -slope (variable b) for the excited cascade with the events in the vicinity of the $E^{-*}(1530)$. For the events within the excited cascade peak, the t -slope parameter extracted from the events in Figure 5.5, is $b = 1.08(4) c^4/\text{GeV}^2$.

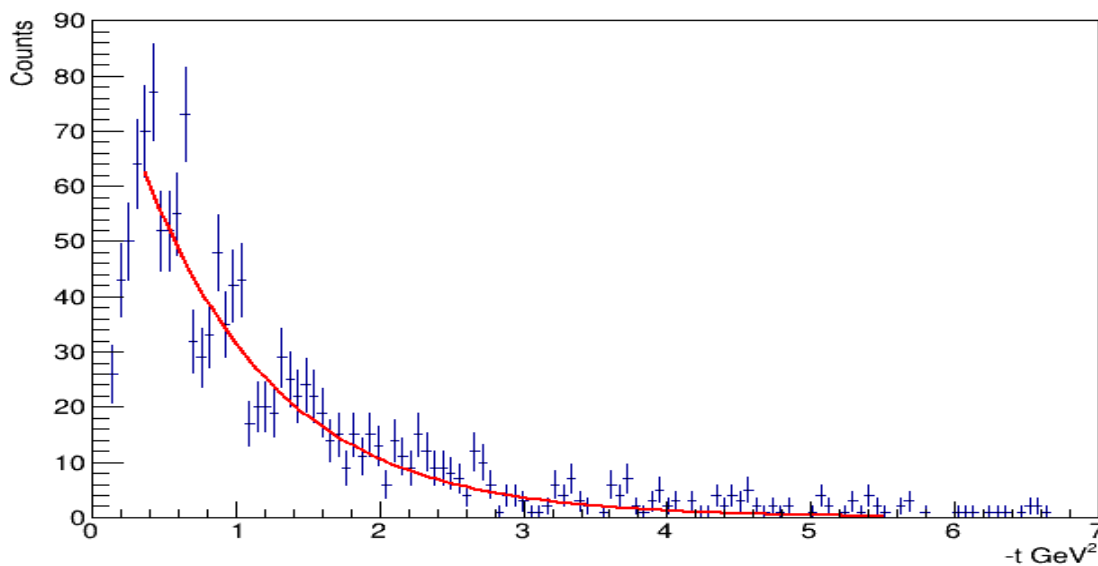


Figure 5.5: Counts vs Mandelstam variable $-t$ for events within the $E^{-*}(1530)$ peak.

5.2 Efficiencies

In a perfect experiment, all particles created would be detected and associated with the correct reaction. Unfortunately, this is not the case in real-world experiments. The GlueX detector is a near hermetic detector but is inefficient in reconstructing events in specific spatial regions.

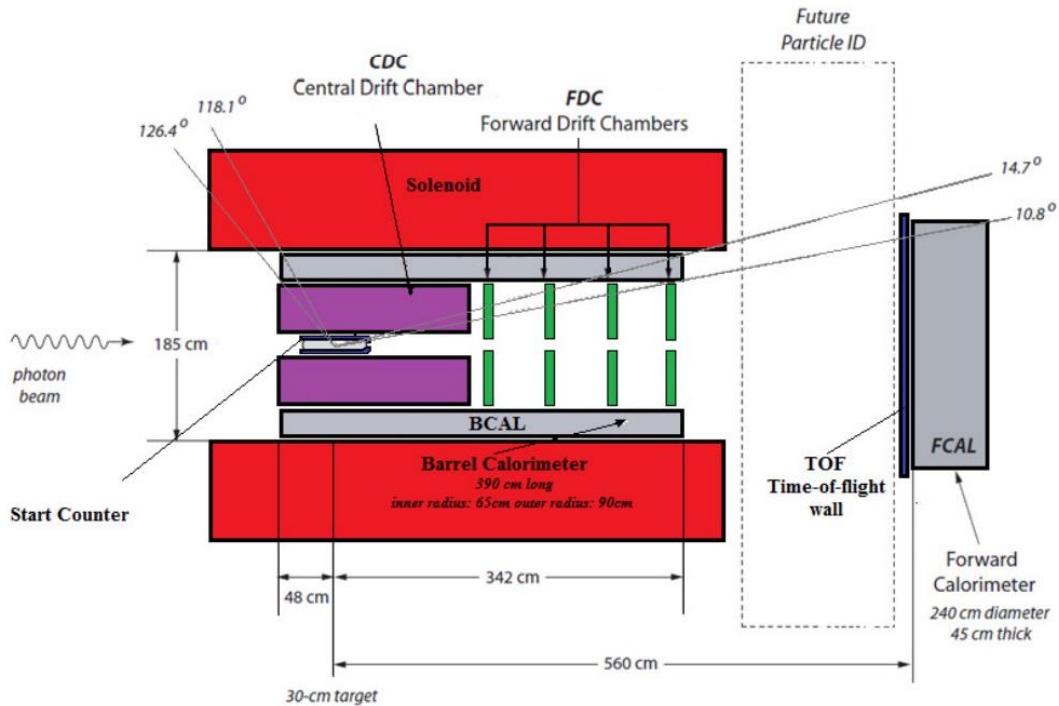


Figure 5.6: Illustration of the GlueX Spectrometer with polar acceptance angles.

Near the beamline of the detector, $\theta < 2^\circ$, detecting any particle, charged or neutral, is impossible because of the hole required for the beamline to exit. Another region where the detection of particles is problematic is in the transition region between the FCAL and BCAL as shown in Figure 5.6, $10.6^\circ < \theta < 11.3^\circ$ [11]. Therefore, efficiency correcting measured data due to faults in the equipment, is important when making a

measurement. To determine the efficiency for the cross-section measurement I produced 6 million events that were partitioned into five energy bins that were each 800 MeV wide and ranged from 7.0 to 11.0 GeV. The plot of the efficiency against beam energy in GeV is given in Figure 5.7. (with errors given by binomial statistics).

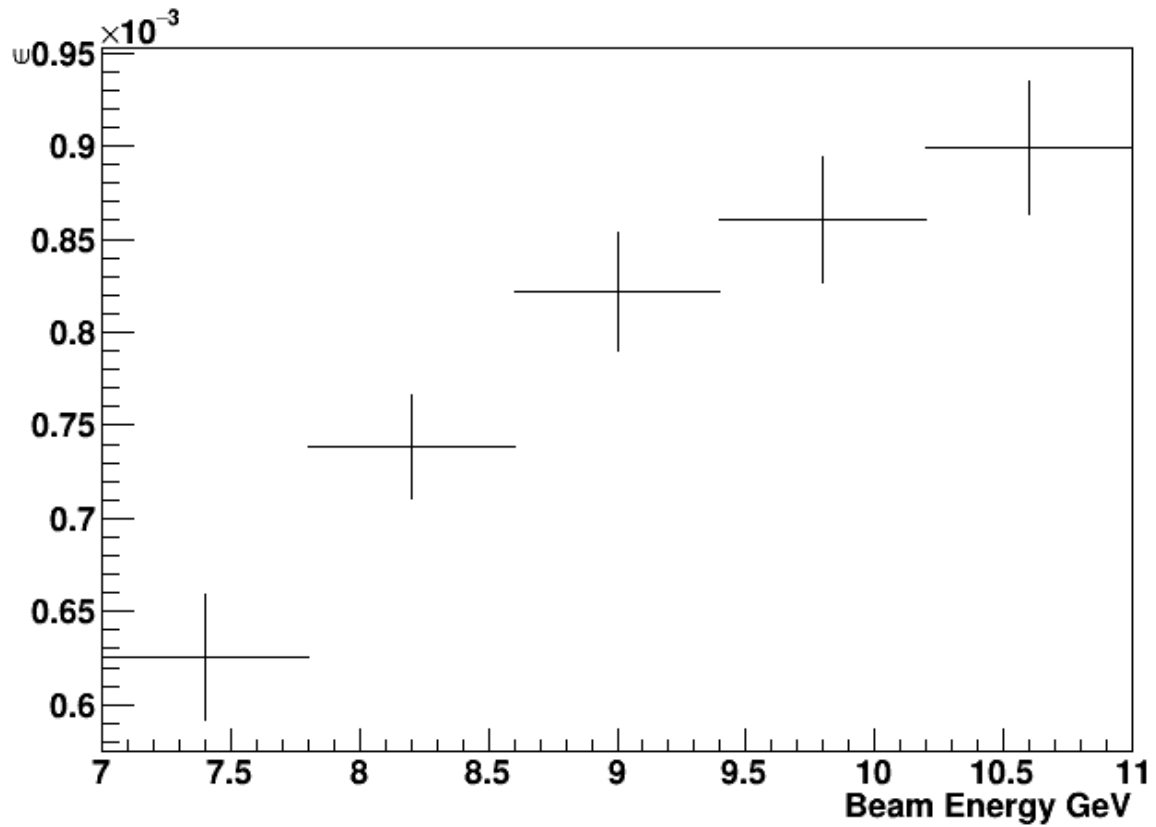


Figure 5.7: Plot of the efficiency versus beam energy in GeV.

Chapter 6

$E(1530)$ CROSS SECTION

6.1 $E^- \pi^0$ Cross Section

The cross-section equation, given in section 4.2.1, is stated again here:

$$\sigma = \frac{Y}{T * \tau * \epsilon}.$$

Figure 4.4 in section 4.2.1, shows the invariant mass spectrum of the $E^-(\Lambda\pi^-)\pi^0$ without accidental subtraction (explained in section 3.2). However, the yield (Y) in the cross-section equation represents an accidental free quantity. With the analysis cuts described in section 4.2.1 (Invariant mass of $\Lambda\pi^-$ system, detector, confidence level and K^* elimination), the yields were extracted in five 800 MeV wide bins starting at beam energy of 7 GeV and ending at 11 GeV. The five mass spectra were fit with a gaussian function for the signal and first order polynomial for the background. Unlike all other fits in this dissertation, which use a χ^2 minimization, the five fits shown in Figure 8.1 use a log-likelihood method for the fits. The log-likelihood method of modeling the fits is employed because of the paucity of events in each of the five mass spectra.

The χ^2 method for fitting data implies the variables are Gaussian distributed, but this is only in the limit of many events. The reason to transition to a Log-Likelihood fit is because the data does not support the benchmark of “many events” and is more consistent with Poisson statistics.

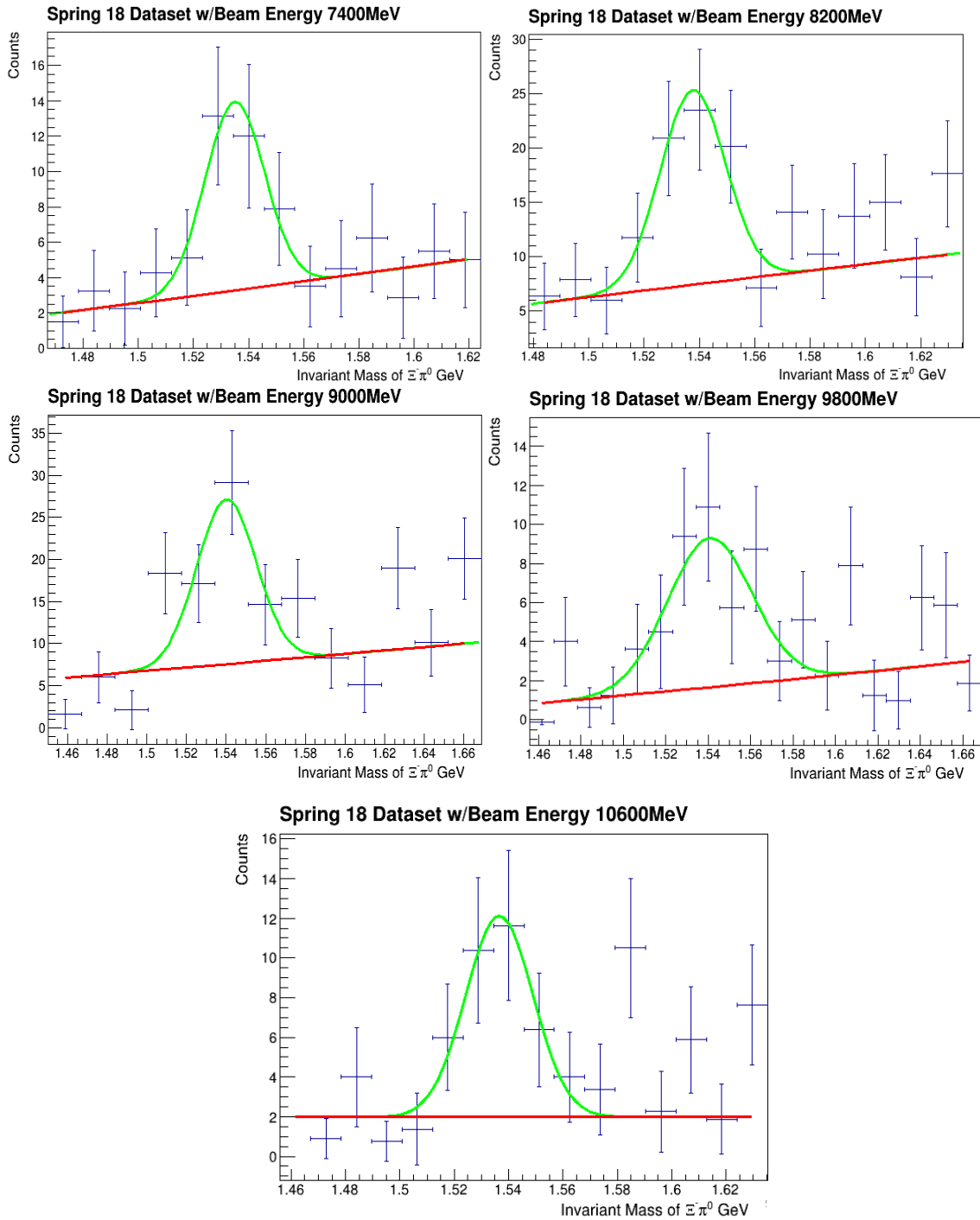


Figure 6.1: Fit to the $E^{*-}(1530)$ for five different energy bins with each energy bin spanning 800 MeV. The photon energy is clearly labeled on each histogram. The green line represents the full fit (gaussian with a first order polynomial background) and the red line represents the background.

With the yields from Figure 6.1, a preliminary cross-section measurement for the reaction $\gamma p \rightarrow K^+ K^+ E^- \pi^0$ were made. The errors shown in Figure 6.2 are only statistical.

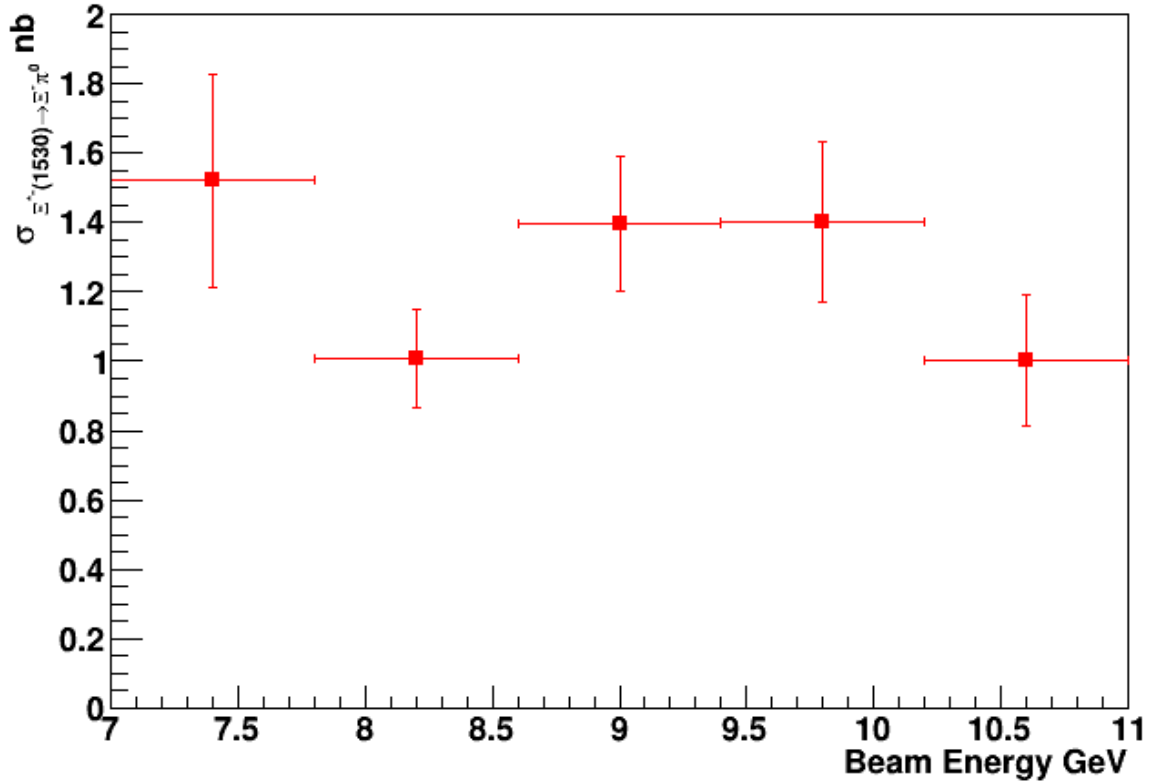


Figure 6.2: Cross section for the $E^{*-}(1530) \rightarrow E^- \pi^0$ for beam energies 7-11 GeV.

The cross-section measurement is a fairly flat distribution above 1 nb. Fitting the distribution with a zeroth order polynomial gives a nominal value of 1.18(8) nb with a χ^2/NDF of 5.85/4.

6.2 Attempt at $E^0 \pi^-$ Cross Section

The decay of E^0 is similar to E^- , and the production follows a similar decay chain:

$$\gamma p \rightarrow K^+ Y^*,$$

$$Y^* \rightarrow K^+ \Xi^{*-},$$

$$\Xi^{*-} \rightarrow \pi^- \Xi^0, \text{ and}$$

$$\Xi^0 \rightarrow \Lambda \pi^0.$$

The difference in the two decay chains ($\Xi^{*-} \rightarrow \Xi^- \pi^0$ and $\Xi^{*-} \rightarrow \Xi^0 \pi^-$) is a swap of charged and neutral pions (both reconstructed from $\Lambda \pi^0 \pi^0$). Analysis cuts implemented on the data use the invariant mass interval of the Ξ^0 from 1.29 to 1.33 GeV/c^2 with the confidence interval above 10^{-3} . Figure 6.3 shows the invariant mass of the $\Xi^0 \pi^-$ system without vertex fitting, and the once prominent $\Xi(1530)$ pictured in Figure 4.4 is washed out. While the peak is not prominent above the background, a fit to the $\Xi(1530)$ was able to extract a center and width. The reconstructed cascade is modeled by a gaussian for the signal and a second order polynomial for the background. The gaussian is centered at 1533(1) MeV/c^2 with standard deviation of 6(2) MeV/c^2 (FWHM of 14(2) MeV).

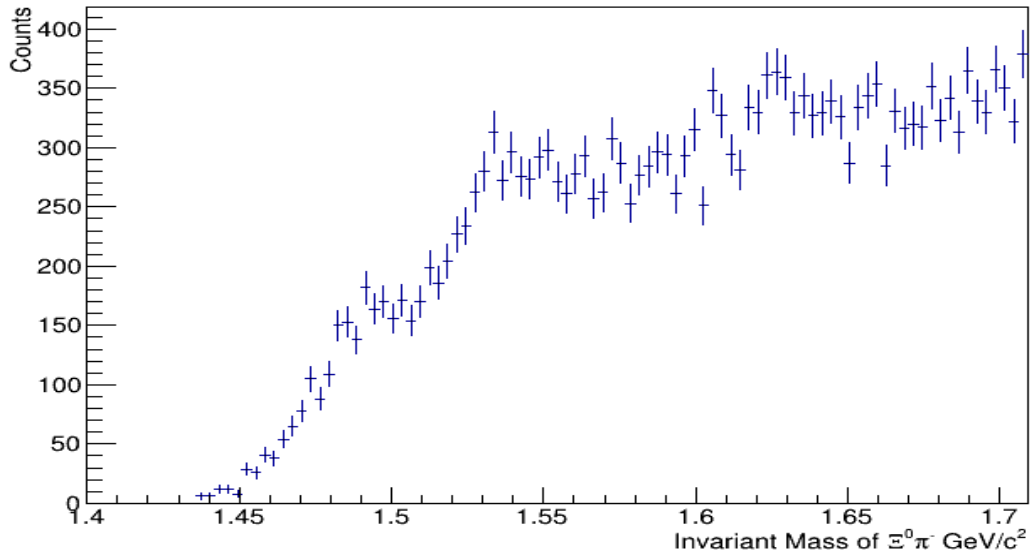


Figure 6.3: Invariant mass of the of $\Xi^0 \pi^-$ (reconstructed from $\Lambda \pi^0 \pi^-$) without vertex fitting.

The vertex fitting cannot be reliably used when only neutral particles come from the same vertex (namely the decay of $\Xi^0 \rightarrow \Lambda \pi^0$), because there are no charged tracks available for a vertex starting value. The vertex determination for a reaction like $\Xi^0 \rightarrow \Lambda \pi^0$ has too few experimental constraints to reliably reconstruct. In order to purify the $\Xi^{*-}(1530)$, kinematic fitting with vertex constraints should be used, but the decay $\Xi^0 \rightarrow \Lambda \pi^0$ has a fatal flaw. Figure 6.4 shows the confidence level versus the invariant mass of the $\Lambda \pi^0$ system with vertex fitting constraints (for comparison see Figure 4.8). There is a very noticeably, large contamination of misidentified events at high confidence level.

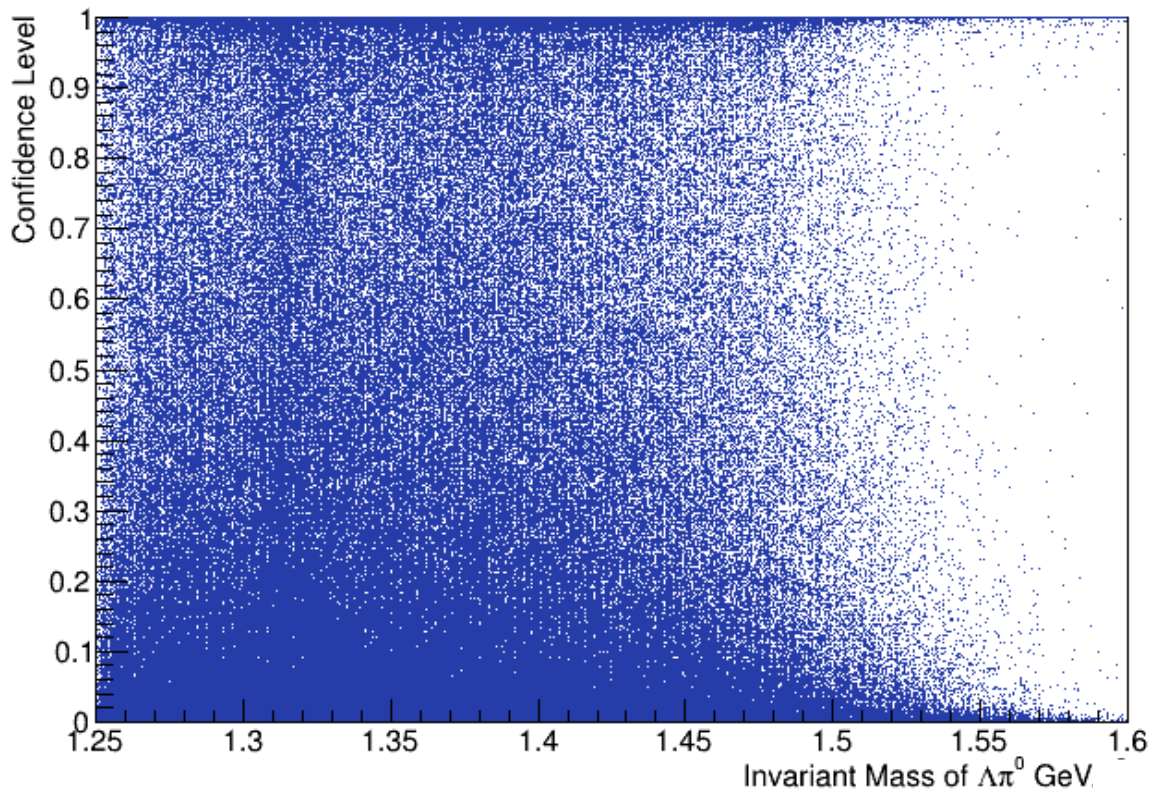


Figure 6.4: Plot of the confidence level against the invariant mass for the $\Lambda \pi^0$ system in GeV.

The amount of misidentified events at high confidence level is a clear indicator that there is a problem using kinematic fitting with vertex constraints for the $\Xi^{*-} \rightarrow \Xi^0 \pi^-$ branches.

There are approximately 167 million events in the files without vertex constraints compared to 99 million events using the vertex fitting. When looking at a confidence level above 0.99, the files without vertex fitting leave only 62 events (representing 3^{-5} % of the entire dataset without vertex constraints), while 88.0 million events survive the same confidence level with vertex constraints (representing 88.7 % of the data). Without progress on vertex identification when a neutral particle decays into more neutrals, further analysis on the $\Xi^0 \pi^-$ branch must be halted. Nevertheless, issues with the vertex fitting have been presented to appropriate members of the GlueX collaboration and a possible resolution is being explored.

6.3 Past Measurements

In general, there have not been many measurements made on the attributes of the cascades since their experimental discovery in 1952. The lack of new cascade data is especially true for photoproduction. However, in the early 2000s, the CLAS (CEBAF Large Acceptance Spectrometer) collaboration began looking at the hyperon spectrum. They investigated reactions of the form $\gamma p \rightarrow K^+ K^+ X$ and $\gamma p \rightarrow K^+ K^+ \pi^- X$, where X could be any particle that was not seen in the detector for that event. Their resolution was sufficient to discern the relatively large $7 \text{ MeV}/c^2$ separation in the known masses of the Ξ^- and Ξ^0 . Additionally, they were able to make cross section measurements of the Ξ^- and $\Xi^-(1530)$.

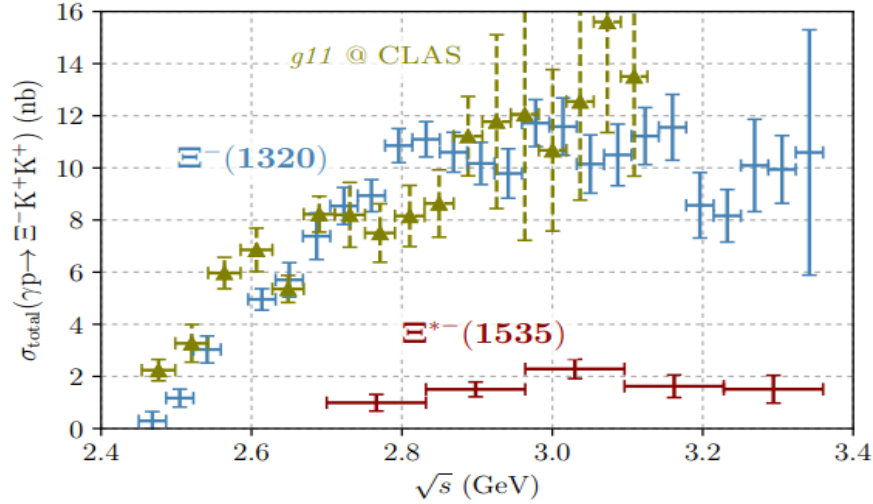


Figure 6.5: The total cross-section for differing values of center of mass energy (\sqrt{s}) for the E^- and $E(1530)$. Note: the photon energy range corresponding to the \sqrt{s} range shown for the $E(1530)$ is ~ 3.5 to 5.3 GeV [17].

The total cross-section utilizing differing values of center of mass energy for the E^- and $E(1530)$ photoproduction during the 6 GeV era at Jefferson Lab is shown in Figure 6.5. The two features of this measurement that are important for purposes of comparison with the GlueX data, that is the topic of this document, is the scale and the energy. The beam energy corresponding to the center of mass energy shown in Figure 6.3 is ~ 3.5 to 5.3 GeV and are less than those used for the GlueX data. In comparison, the GlueX $E(1530)$ cross sections have incident photon energies ranging from 7 to 11 GeV. Additionally, the value of the cross section for the reaction $E(1530) \rightarrow E^- \pi^0$ is on the scale of a few nanobarns which is consistent with the cross-section expectation for other photoproduced excited cascades. According to the CLAS collaboration:

Upper limits were calculated on the production total cross sections of the three best-known excited states: the $E(1690)$, the $E(1820)$ and the $E(1950)$ at 0.75 nb, 1.01 nb, and 1.58 nb, respectively, at the 90% confidence limit. [17]

The experimental observation lends some credence to cross-section calculations reported above. Additionally, an earlier CLAS collaboration paper [18], published in 2007, reported the total cross-section of $E^-(1530)$ as $1.76 \pm 0.24 \pm 0.13$ nb with a beam energy ranging from 3.35- 4.75 GeV.

In 2018, for the incident photon energy range from 7 to 11 GeV, Ashely Ernst from Florida State University made an experimental measurement of the total cross section for the reaction $\gamma p \rightarrow K^+ K^+ E^-$. Figure 6.6 shows the total cross section of the ground-state E^- from GlueX and CLAS versus incident photon energy. At higher beam energies the total cross section continuously diminishes from 6 to 11 GeV.

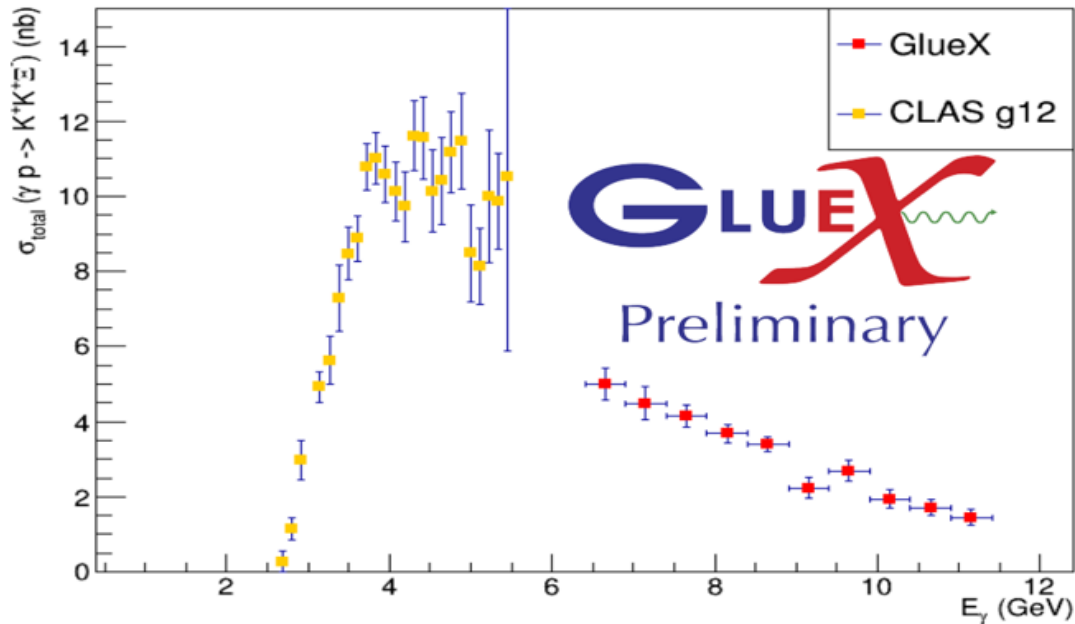


Figure 6.6: Updated total cross sections for the E^- [19].

6.4 Total Cross Section for $\mathcal{E}^{*-}(1530)$

To make a proper comparison to the CLAS 12 data, the total cross-section for the reaction channel $\gamma p \rightarrow K^+ K^+ \mathcal{E}^{*-}$ must include both decay modes of the $\mathcal{E}(1530)$ (to $\mathcal{E}^0 \pi^-$ and $\mathcal{E}^- \pi^0$). While the analysis focuses on the $\mathcal{E}^- \pi^0$ channel, progress can be made on the charge exchange channel, $\mathcal{E}^0 \pi^-$. The decay of $\mathcal{E}(1530)$ proceeds through the strong-interaction and this means isospin is conserved. Initial isospin of the excited cascade is $\frac{1}{2}$. The Clebsch-Gordan coefficients can be used to determine the relative rate of production for each channel. The decay can be written as

$$\mathcal{E}^{*-} = a|\pi^0\rangle |\mathcal{E}^-\rangle + b|\pi^-\rangle |\mathcal{E}^0\rangle,$$

where the coefficients a and b are the Clebsch-Gordan coefficients. We can write the reaction in terms of isospin:

$$\left|\frac{1}{2}, -\frac{1}{2}\right\rangle = \sqrt{\frac{1}{3}} \left[|1, 0\rangle \left|\frac{1}{2}, -\frac{1}{2}\right\rangle\right] - \sqrt{\frac{2}{3}} \left[|1, -1\rangle \left|\frac{1}{2}, \frac{1}{2}\right\rangle\right],$$

which corresponds to

$$|\mathcal{E}^{*-}\rangle = \sqrt{\frac{1}{3}} |\pi^0 \mathcal{E}^-\rangle - \sqrt{\frac{2}{3}} |\pi^- \mathcal{E}^0\rangle.$$

From the Clebsch-Gordan decomposition, the neutral cascade channel was determined to be twice as likely to occur when compared to the charged counterpart. The vertex fitting for the $\mathcal{E}^{*-} \rightarrow \mathcal{E}^- \pi^0$ is very helpful in refining the mass resolution, but when

comparing to the $\Xi^{*-} \rightarrow \Xi^0 \pi^-$ decay channel (plagued with vertex fitting issues), the vertex constraints have to be removed.

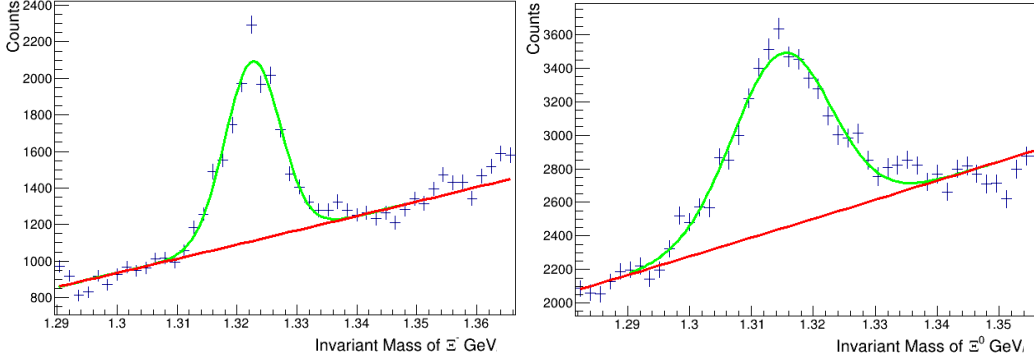


Figure 6.7: Invariant mass distributions of the Ξ^- on the left and neutral Ξ^0 right measured in GeV.

I determine the relative rate of production within the dataset by examining the raw yields of ground state cascades in each channel without vertex fitting. Referring to Figure 6.7, both signals from the cascades were fit with gaussians and the background were fit with a first-order polynomial. The signal for the Ξ^0 is centered at 1.314(2) GeV with a gaussian that has a standard deviation of 7.1(3) MeV (FWHM of 16.8(7) MeV). In comparison to the Ξ^- (without vertex fitting) which is centered at 1.3226(1) GeV with a gaussian standard deviation of 4.5503(2) MeV (FWHM of 11(2) MeV). The raw yields for $\Xi^-(1320)$ is $N[\Xi^-(1320)] \approx 7200$ while for the $\Xi^0(1320)$ $N[\Xi^0(1320)] \approx 13300$, suggesting that the imperfect iso-symmetry yields a reasonable prediction of the branching ratio between the two channels, $\frac{N[\Xi^-(1320)]}{N[\Xi^0(1320)]} = 0.54(2)$. Without efficiency correcting the data, the data conforms to iso-spin symmetry within two standard deviations.

There are two other interesting aspects of the ground-state cascades that the previous examination shows. The first is the difference in the mass of the two cascades. As reported in the PDG, the mass difference is $6.85(0.21)$ MeV, and the difference calculated from the data is within a single standard deviation at 8.6 ± 2.0 MeV. This mass difference between the Ξ^- and Ξ^0 is larger than would be predicted by simply exchanging up and down quarks. For purposes of comparison, the pseudoscalar meson K^- and neutral K^0 have a mass separation of only $3.934(0.20)$ [2]. The second measure that can be calculated, but also easily seen from Figure 6.7, is the differing widths of both cascades. The widening of the neutral cascade is due to detector resolution effects in reconstructing the neutral pion. The Ξ^0 dominant decay mode is $\Lambda\pi^0$, whereas $\Xi^- \rightarrow \Lambda\pi^-$. The charged pion is directly observed using the GlueX spectrometer, but the neutral π^0 is reconstructed from two photons seen in either the BCAL and/or FCAL.

The total cross section for the $\Xi(1530)$ is the summation of both possible decay branches ($\sigma_T = \sigma_{\Xi^-\pi^0} + \sigma_{\Xi^0\pi^-}$). Using the conservation of isospin we can relate the unknown cross section to the measured cross section:

$$\sigma_{\Xi^0\pi^-} = 2.0 \sigma_{\Xi^-\pi^0},$$

which leads to,

$$\sigma_T = 3.0 \sigma_{\Xi^-\pi^0}.$$

With relative scaling between the channels, I am able to produce a total cross section for the photoproduced excited $\Xi(1530)$ at previously unachieved beam energies. Figure 6.8 is the total cross section for the excited $\Xi(1530)$, my data are shown in blue and

the CLAS g12 data are red. The x-axis is in terms of center of mass energy \sqrt{s} in GeV. After surpassing the threshold energy for creating the excited cascade, the total cross section seems to rise slowly and maintain a value around 3.5(3) nb.

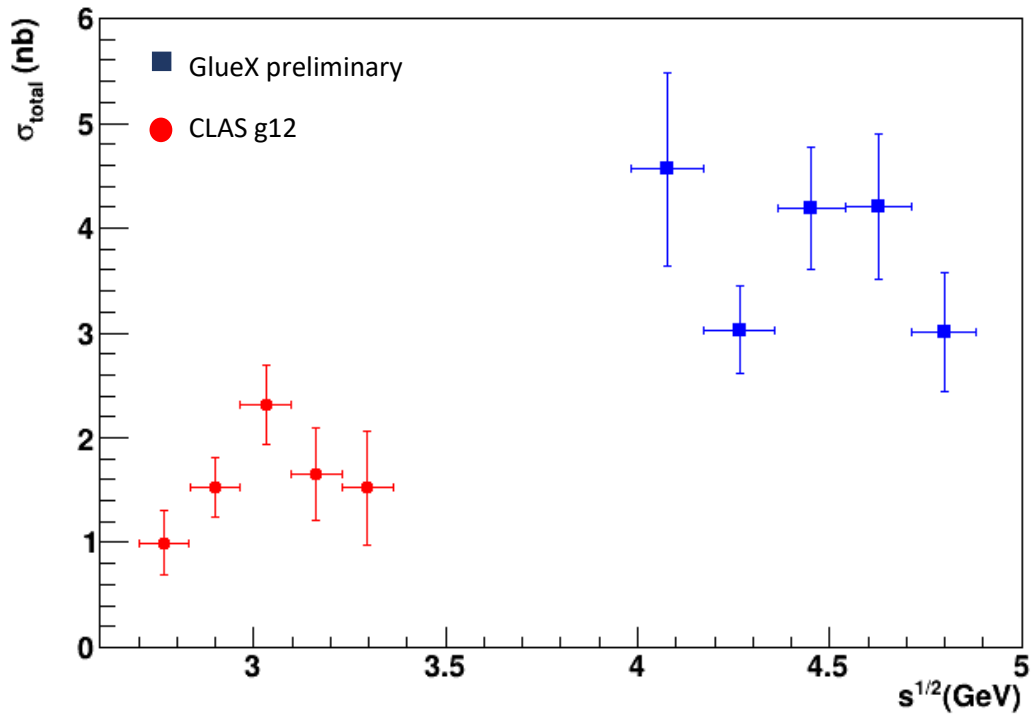


Figure 6.8: Total cross section for the $E(1530)$ in nb plotted against center of mass energy \sqrt{s} in GeV. CLAS g12 data is in red, my total cross section is in blue.

SIMULTANEOUS FITTING

Analysis Cut	$\Xi^- \pi^0$ channel	$K^- \Lambda$ channel
Data Set	Spring 2018	Fall 2018
Invariant Mass Cut	$1.31 < \Lambda \pi^- < 1.34 \text{ GeV}/c^2$	$1.107 < \Lambda < 1.124 \text{ GeV}/c^2$
Confidence Level	$>10^{-4}$	$>10^{-4}$
Background Excluded	$0.81 < K^+ \pi^0 < 0.98 \text{ GeV}/c^2$	$1.00 < K^- K^+ < 1.04 \text{ GeV}/c^2$

Table 7.1: Summary of important analysis cuts used on the spring and fall 2018 data sets for the $\Xi^- \pi^0$ and $K^- \Lambda$.

As mentioned in the introduction, the $\Xi(1530)$ couples almost entirely to the $\Xi\pi$ channel, but higher mass cascades tend to have a strong coupling to the $K\Lambda$ and/or $K\Sigma$ channel with a small branching fraction to $\Xi\pi$. High luminosity running at GlueX, given the small cross sections for the cascades (about a few nano-barns) opens the door to the opportunity for seeing higher mass cascades in the $\Xi\pi$ invariant mass spectrum. Table 7.1 gives a quick summary of important analysis cuts for the $\Xi\pi$ and $K^- \Lambda$.

The mass spectra for two decay branches of the Ξ^{*-} can be seen in Figure 7.1, where the top panel gives the invariant mass of $K^- \Lambda$ and the bottom panel shows the invariant mass of $\Xi^- \pi^0$. The apparent structures in the bottom panel of Figure 7.1 correlate to the first three excited cascades: $\Xi(1530)$, $\Xi(1620)$ and $\Xi(1690)$. The $\Xi(1530)$ is the strongest signal. Following the $\Xi(1530)$ in Figure 7.1, is a large bump near the $\Xi(1620)$.

Little is known about the nature of the $\Xi(1620)$ and, while included in the particle listing, is omitted from the summary table due to a lack of conclusive evidence. The PDG particle listing has three experimental measurements of the $\Xi(1620)$, with widths ranging from 22.5 to 55 MeV. The final resonance on the bottom plot of Figure 7.1 is the $\Xi(1690)$, a well-established, three-star state. The top plot of Figure 7.1 contains two visible resonances: the $\Xi(1690)$ and the $\Xi(1820)$.

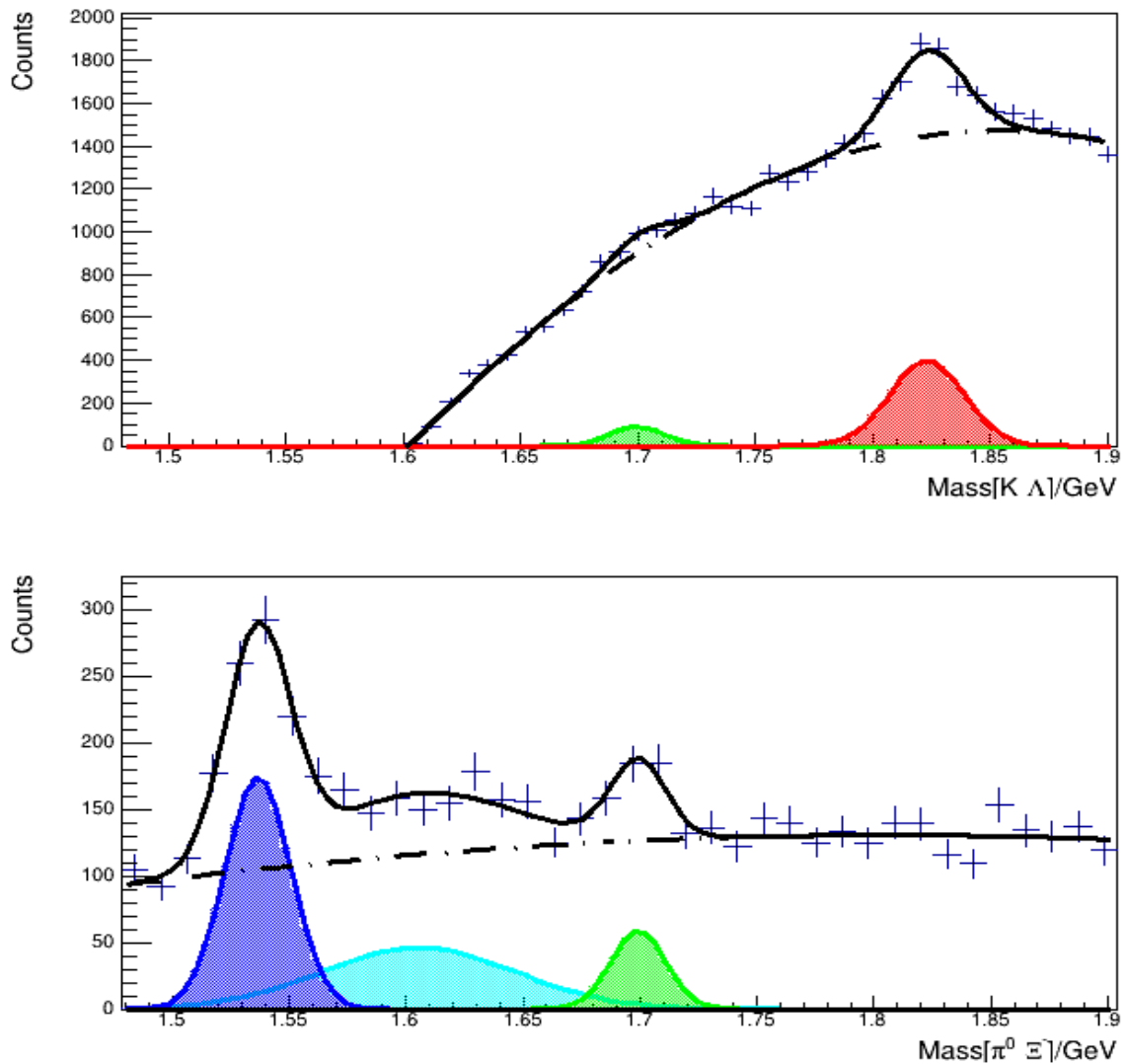


Figure 7.1: Simultaneous fit between the $K^- \Lambda$ channel and the $\Xi^- \pi^0$ channel.

A simultaneous fit was performed for the mass spectra shown in both panels of Figure 7.1. For simplicity, all signals were modeled with a gaussian, while the background was modeled as a third-order polynomial. The centers and widths for the three lightest excited cascades are given in Table 7.2.

		$E(1530)$ MeV	$E(1620)$ MeV	$E(1690)$ MeV	$E(1820)$ MeV
Data	Center	1537 ± 1	1610 ± 10	1699 ± 2	1823 ± 1
Data	FWHM	33 ± 5	99 ± 26	28 ± 5	35 ± 2
PDG	Center	1535 ± 0.6	1620	$1691.1 + 1.9 - 2.0$	1823 ± 5
PDG	Width	9.9+1.7-1.9	22.5	< 30	24+15-10

Table 7.2: Summary of $E\pi$ invariant-mass-spectrum gaussian-fit parameters in MeV, with comparison to PDG[2] values.

Regarding the $K\Lambda$ invariant mass spectrum, the relatively large branching ratio to the $E(1820)$ channel leaves that cascade as the dominant feature of the spectrum. Nevertheless, there is more information to be gleaned from the invariant mass spectrum in the top panel of Figure 7.1. What can be seen immediately, is the lack of events with mass below 1.6 GeV. The reason why the strongest cascade, $E(1530)$, has vanished from the $K\Lambda$ invariant mass spectrum can be easily explained. The minimum energy required to produce a kaon/lambda pair is the addition of the rest mass of each particle (1598 MeV), which is above the rest mass of the $E(1530)$. Simultaneously fitting both channels, with the centers and widths of the gaussian signals as common fitting parameters between the two branches, while allowing the amplitude and backgrounds to vary, results in the gaussian

parameters given in Table 7.2. As the only common cascade, the $\mathcal{E}(1690)$ shares the same parameters for both decay branches. The uncommon cascade, $\mathcal{E}(1820)$, has a center and standard deviation of 1.823(1) GeV and 15(1) MeV (FWHM 35(2) MeV), respectively.

To quantify the significance of the $\mathcal{E}(1690)$ peak in the $K^-\Lambda$ invariant mass spectrum, I simultaneously fit both channels with, and without, the $\mathcal{E}(1690)$ peak in the $K^-\Lambda$ spectrum, while taking note of the calculated χ^2 . With the cascade $\mathcal{E}(1690)$ peak included in the $K^-\Lambda$ fit, I obtained $\chi^2 = 77.9$ with a number of degrees of freedom equal to 54. Without the $\mathcal{E}(1690)$ peak modeled as a part of the signal within the $K^-\Lambda$ invariant mass spectrum, I obtain $\chi^2 = 91.2$ with the number of degrees of freedom 55. When referencing the χ^2 table, one can determine the probability of getting such values for χ^2 with and without the $\mathcal{E}(1690)$ modeled in the $K^-\Lambda$ invariant mass spectrum as 1.83 and 0.15 percent respectively. While the probability for such χ^2 are low, the probability is 12 times more likely when the $\mathcal{E}(1690)$ is included in both decay channels.

PARTIAL WAVE ANALYSIS

The purpose of the partial wave analysis performed in this document is to determine the quantum numbers of particular cascade resonances, J^P . While the ground state cascades (P assumed [2]) and $\mathcal{E}(1530)$ have well documented quantum numbers, many of the other cascades have no J^P designation.

To start the PWA, a specific frame of reference needs to be chosen. The Gottfried-Jackson (GJ) frame, described in section 1.4, was chosen. The partials waves are defined at the end of section 1.4 and the expression can be simplified using Figure 1.6. Referencing the equation for the partial wave A_b :

$$A_b(\tau) = \sqrt{\frac{2l+1}{4\pi}} F_l(p) a_{ls} \sum_{\lambda_1 \lambda_2} D_{m\lambda}^{J*}(\Omega_{GJ}) \langle l0s\lambda | J\lambda \rangle \langle s_1 \lambda_1 s_2^{-\lambda_2} | s\lambda \rangle.$$

The subscripts one and two refer to the daughter particles of the $\mathcal{E}(1530)$, while the lack of subscript refer to total spin (s) or helicity (λ). As the excited cascade decays into a spin- $\frac{1}{2}$ baryon ($\lambda_1 = \frac{1}{2}$) and pseudo-scalar meson ($\lambda_2 = 0$). Thus, the rightmost term simplifies to one,

$$\left\langle s_1 = \frac{1}{2}, \lambda_1 = \pm \frac{1}{2}, s_2 = 0,^{-\lambda_2} = 0 \middle| s = \frac{1}{2}, \lambda = \pm \frac{1}{2} \right\rangle = 1.$$

The $E(1530)$'s total angular momentum and parity is $3/2^+$, while the E^- and π^0 have total spin and parity of $1/2^+$ and 0^- , respectively. Given the daughter particles (E^- and π^0) have spin $1/2$ and 0 , the orbital angular momentum, l , could be either be 1 or 2. However, since the strong interaction conserves parity and the parity of angular momenta states is $P = (-1)^l$, then l must be equal one. The Clebsch-Gordan coefficient $\langle l0s\lambda | J\lambda \rangle$ represents the overlap of two different basis. For a given angular momentum J , total spin s and total orbital angular momentum l , the last free parameter is the total helicity λ . The total helicity is constrained to either $\pm 1/2$ for any $\langle l0s\lambda | J\lambda \rangle$. The two possible Clebsch-Gordan coefficients for $J = 3/2$, $l=1$, are shown in the top two rows of table 8.1. The bottom two rows give the coefficients for the $J = 1/2$, $l=1$ case.

Overlap	Value
$\langle l = 1, \lambda_l = 0, s = \frac{1}{2}, \lambda = +\frac{1}{2} J = \frac{3}{2}, \lambda = +\frac{1}{2} \rangle$	$\sqrt{\frac{2}{3}}$
$\langle l = 1, \lambda_l = 0, s = \frac{1}{2}, \lambda = -\frac{1}{2} J = \frac{3}{2}, \lambda = -\frac{1}{2} \rangle$	$\sqrt{\frac{2}{3}}$
$\langle l = 1, \lambda_l = 0, s = \frac{1}{2}, \lambda = +\frac{1}{2} J = \frac{1}{2}, \lambda = +\frac{1}{2} \rangle$	$-\sqrt{\frac{1}{3}}$
$\langle l = 1, \lambda_l = 0, s = \frac{1}{2}, \lambda = -\frac{1}{2} J = \frac{1}{2}, \lambda = -\frac{1}{2} \rangle$	$\sqrt{\frac{1}{3}}$

Table 8.1: Clebsch-Gordan coefficients $\langle l0s\lambda | J\lambda \rangle$ for $J=1/2$ and $J=3/2$.

The Wigner D-function, $D_{m\lambda}^J$, is used to rotate states. More specifically the Wigner-D functions define the coefficients of the overlap of different spin projections,

$$|J, m\rangle = \sum_{m'} D_{mm'}^J(\alpha, \beta, \gamma) |J, m'\rangle,$$

where, α, β, γ are the Euler angles. The Euler angles are replaced by traditional polar and azimuthal angles ($\alpha = \phi, \beta = \theta, \gamma = 0$). Substitutions allow us to write the big Wigner D-functions, $D_{mm'}^J$, in terms of the small Wigner D-functions, $d_{m,m'}$:

$$D_{mm'}^J(\Omega) = e^{-im'\phi} d_{m,m'}(\theta),$$

$$d_{m,m'}(\theta) = \langle Jm | e^{-i\theta J_y} | Jm' \rangle.$$

The small Wigner D-functions for $J = 1/2, 3/2$ are given in Table 8.2.

$J=3/2$	$m_2 = 3/2$	$m_2 = 1/2$	$m_2 = -1/2$	$m_2 = -3/2$
$m_1 = 3/2$	$\frac{1 + \cos(\theta)}{2} \cos\left(\frac{\theta}{2}\right)$	$-\sqrt{3} \frac{1 + \cos(\theta)}{2} \sin\left(\frac{\theta}{2}\right)$	$\sqrt{3} \frac{1 + \cos(\theta)}{2} \cos\left(\frac{\theta}{2}\right)$	$-\frac{1 - \cos(\theta)}{2} \sin\left(\frac{\theta}{2}\right)$
$m_1 = 1/2$	$\sqrt{3} \frac{1 + \cos(\theta)}{2} \sin\left(\frac{\theta}{2}\right)$	$\frac{3 \cos(\theta) - 1}{2} \cos\left(\frac{\theta}{2}\right)$	$-\frac{3 \cos(\theta) + 1}{2} \sin\left(\frac{\theta}{2}\right)$	$\sqrt{3} \frac{1 + \cos(\theta)}{2} \cos\left(\frac{\theta}{2}\right)$
$m_1 = -1/2$	$\sqrt{3} \frac{1 + \cos(\theta)}{2} \cos\left(\frac{\theta}{2}\right)$	$\frac{3 \cos(\theta) + 1}{2} \sin\left(\frac{\theta}{2}\right)$	$\frac{3 \cos(\theta) - 1}{2} \cos\left(\frac{\theta}{2}\right)$	$\sqrt{3} \frac{1 + \cos(\theta)}{2} \sin\left(\frac{\theta}{2}\right)$
$m_1 = -3/2$	$\frac{1 - \cos(\theta)}{2} \sin\left(\frac{\theta}{2}\right)$	$-\sqrt{3} \frac{1 + \cos(\theta)}{2} \cos\left(\frac{\theta}{2}\right)$	$-\sqrt{3} \frac{1 + \cos(\theta)}{2} \sin\left(\frac{\theta}{2}\right)$	$\frac{1 + \cos(\theta)}{2} \cos\left(\frac{\theta}{2}\right)$
	$J=1/2$	$m_2 = 1/2$	$m_2 = -1/2$	
	$m_1 = 1/2$	$\cos\left(\frac{\theta}{2}\right)$	$-\sin\left(\frac{\theta}{2}\right)$	
	$m_1 = -1/2$	$\sin\left(\frac{\theta}{2}\right)$	$\cos\left(\frac{\theta}{2}\right)$	

Table 8.2: Small Wigner- d table, $d_{m_1 m_2}^J$, for $J = 3/2, 1/2$ expressed in terms of sines and cosines.

More specifically, the $\cos\theta_{GJ}$ distributions for a given invariant mass is fit to the intensity function:

$$I(\tau) = \sum_{i,j} \sum_{b,b'} {}^i A_b(\tau) {}^{i,j} \rho_{bb'} {}^j A_{b'}^*(\tau),$$

where the index on the upper left of each variable is the initial state and the sum on b represents possible quantum numbers. The internal structure of the spin density matrix is not assumed, with individual elements assimilated within fit parameters.

For a given invariant mass range, the $\cos\theta_{GJ}$ spectrum is fit to the intensity spectrum. The invariant mass of the $\Xi\pi$ spectrum against the $\cos(\theta_{GJ})$ is plotted in Figure 8.1.

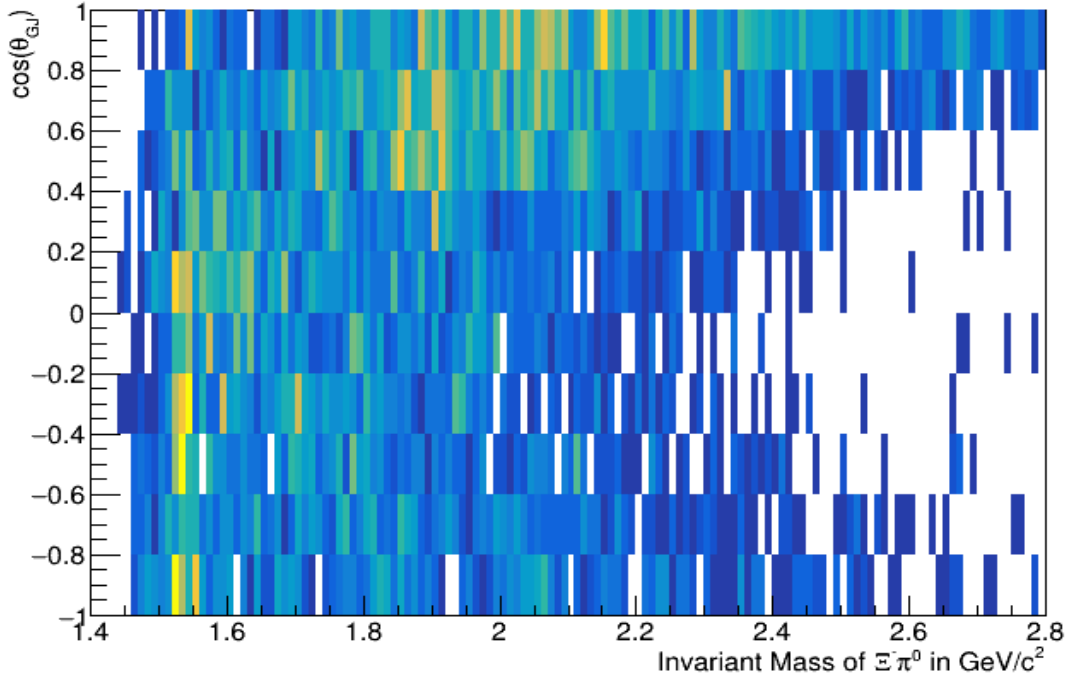


Figure 8.1: Invariant mass of the $\Xi\pi$ system plotted against $\cos(\theta_{GJ})$.

To extract the $\mathcal{E}(1530)$ yields in the GJ frame, I binned the y-axis in ten $\cos(\theta_{GJ})$ bins each 0.2 wide. Figures 8.2 to Figure 8.11 depicts the yield extraction for all $\cos(\theta_{GJ})$ values. The $\mathcal{E}(1530)$ is fit with a gaussian, the structure to the immediate right of the $\mathcal{E}(1530)$ is a consistent feature in all but one yield extraction fit (Fig. 8.3 with $\cos\theta_{GJ}$, between -0.8 and -0.6). The feature has a center around a mass of 1580 MeV and will be referred to as feature F(1580). The last resonance in the figures is the $\mathcal{E}(1690)$. For each figure, the red represents the background to the extracted $\mathcal{E}(1530)$. The background in red includes a third order polynomial that is multiplied by a sigmoid function used to mimic threshold behavior. Included with the polynomial background, there are background peaks representing the F(1580) feature and $\mathcal{E}(1690)$ resonance. The extracted background-subtracted signal peak is shown in green.

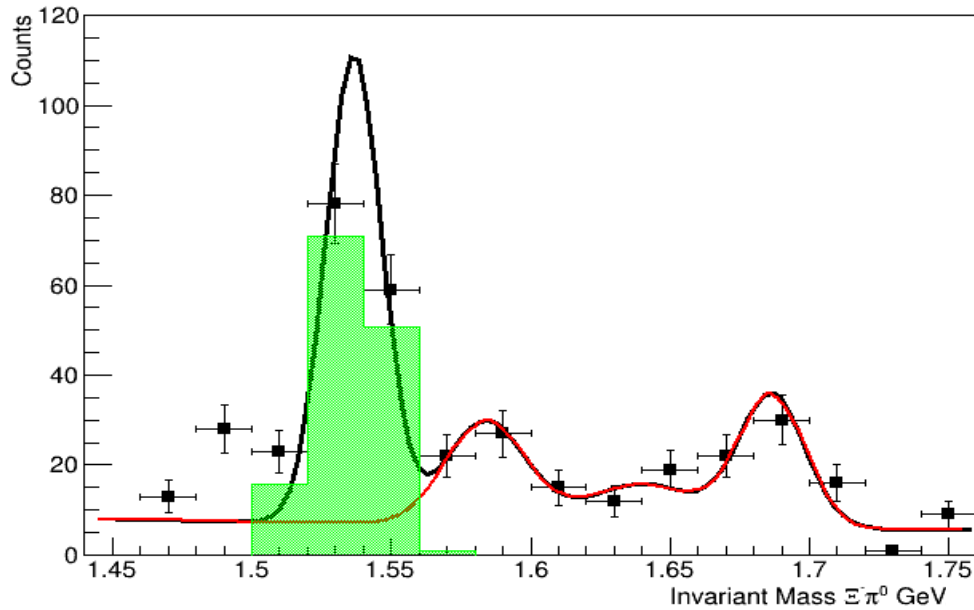


Figure 8.2: Invariant Mass Distribution of \mathcal{E}^{*-} in GeV with $\cos\theta_{GJ}$, between -1.0 and -0.8 , with extracted $\mathcal{E}(1530)$ having a yield of 138 ± 12 .

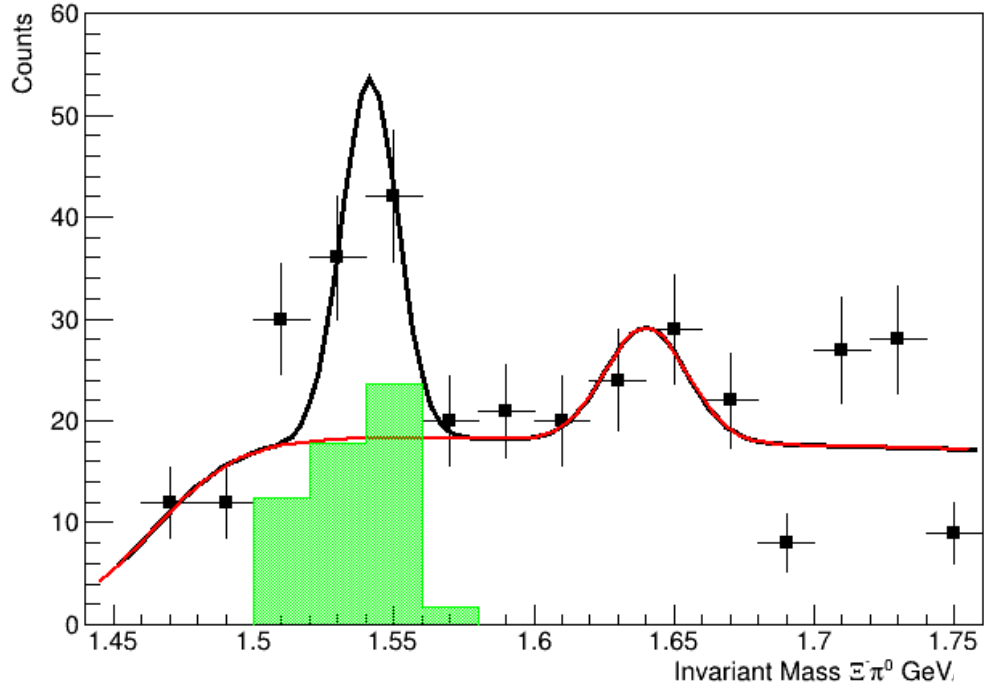


Figure 8.3: Invariant Mass Distribution of E^{*+} in GeV with $\cos\theta_{GJ}$, between -0.8 and -0.6 , with extracted $E(1530)$ having a yield of 56 ± 7 .

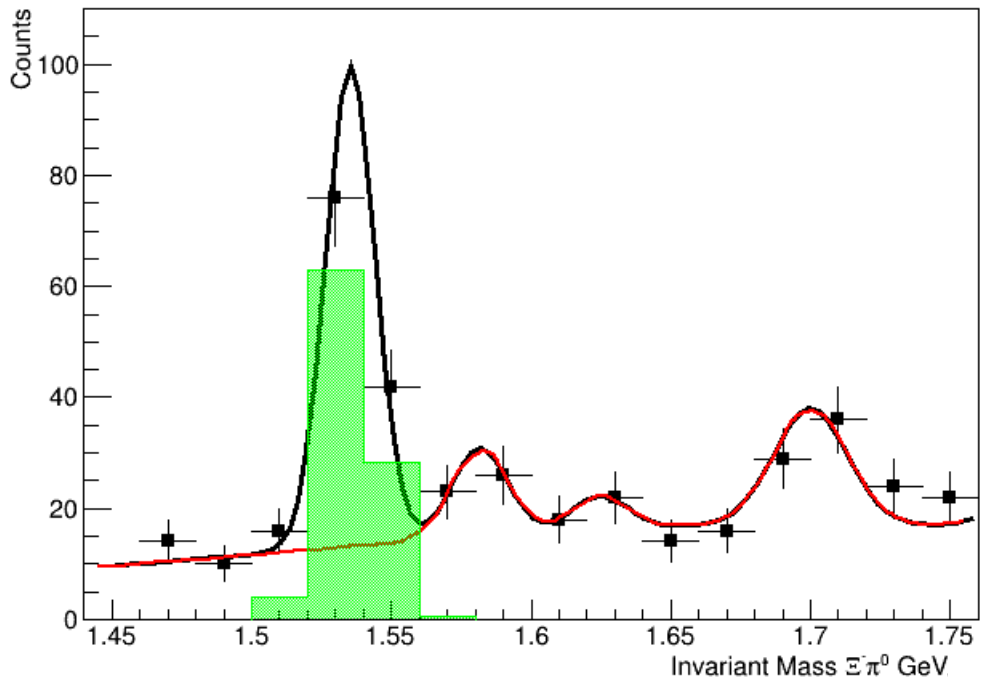


Figure 8.4: Invariant Mass Distribution of E^{*+} in GeV with $\cos\theta_{GJ}$, between -0.6 and -0.4 , with extracted $E(1530)$ having a yield of 96 ± 10 .

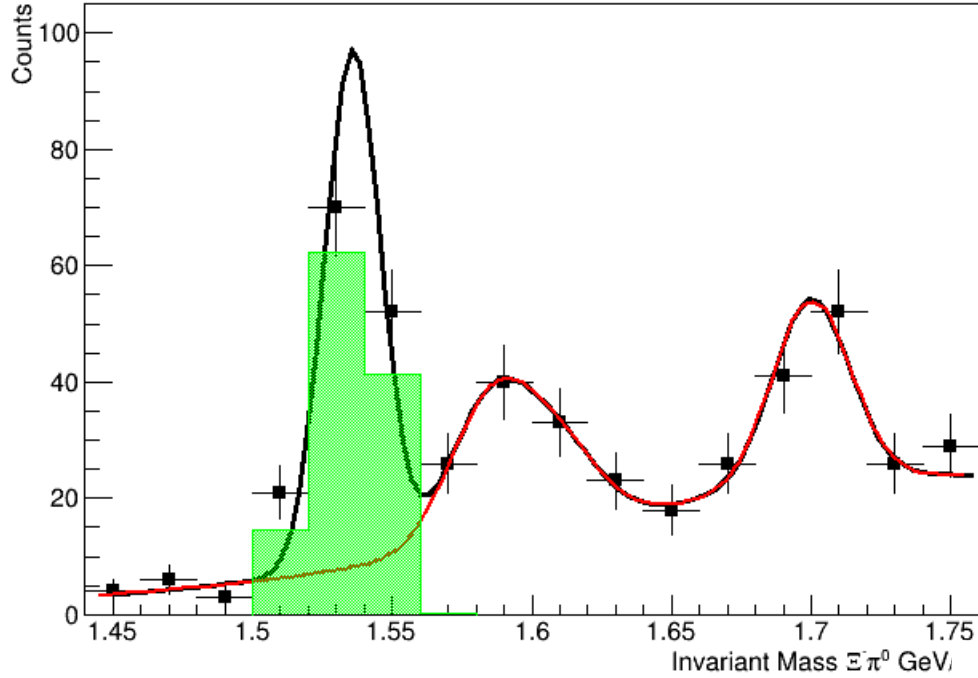


Figure 8.5: Invariant Mass Distribution of E^{*+} in GeV with $\cos\theta_{GJ}$, between -0.4 and -0.2 , with extracted $E(1530)$ having a yield of 119 ± 11 .

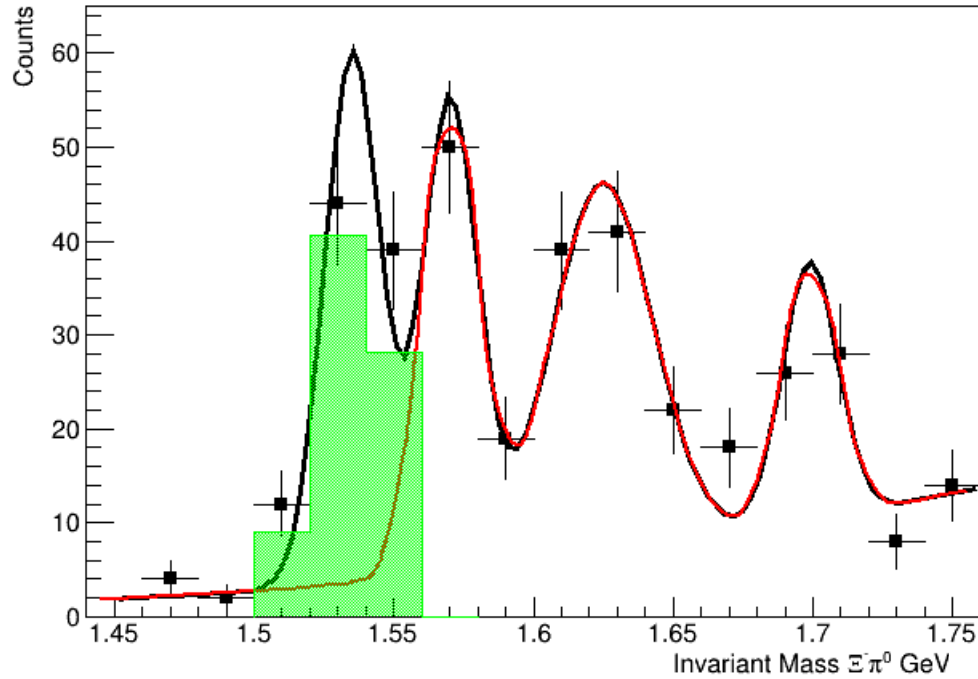


Figure 8.6: Invariant Mass Distribution of E^{*+} in GeV with $\cos\theta_{GJ}$, between -0.2 and 0.0 , with extracted $E(1530)$ having a yield of 72 ± 8 .

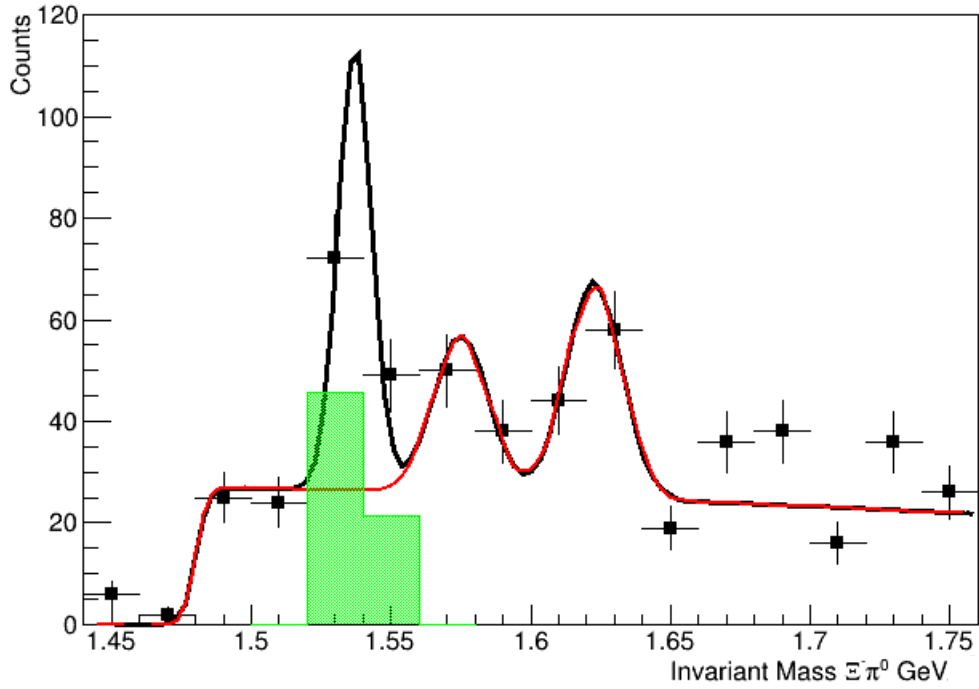


Figure 8.7: Invariant Mass Distribution of E^{*-} in GeV with $\cos\theta_{GJ}$, between 0.0 and 0.2, with extracted $E(1530)$ having a yield of 61 ± 8 .

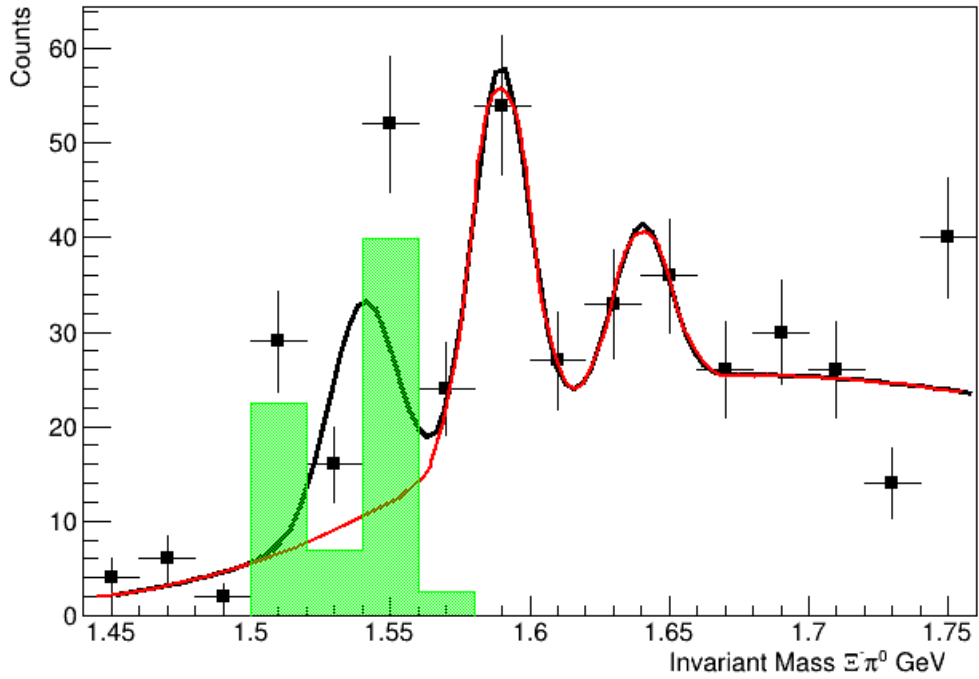


Figure 8.8: Invariant Mass Distribution of E^{*-} in GeV with $\cos\theta_{GJ}$, between 0.2 and 0.4, with extracted $E(1530)$ having a yield of 72 ± 8 .

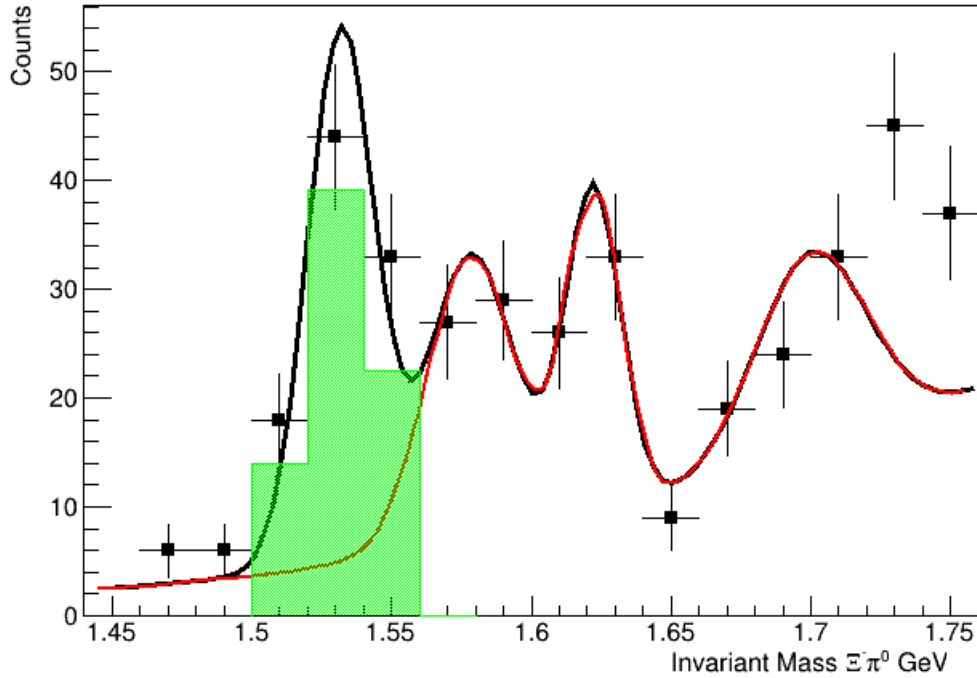


Figure 8.9: Invariant Mass Distribution of E^{*+} in GeV with $\cos\theta_{GJ}$, between 0.4 and 0.6, with extracted $E(1530)$ having a yield of 73 ± 9 .

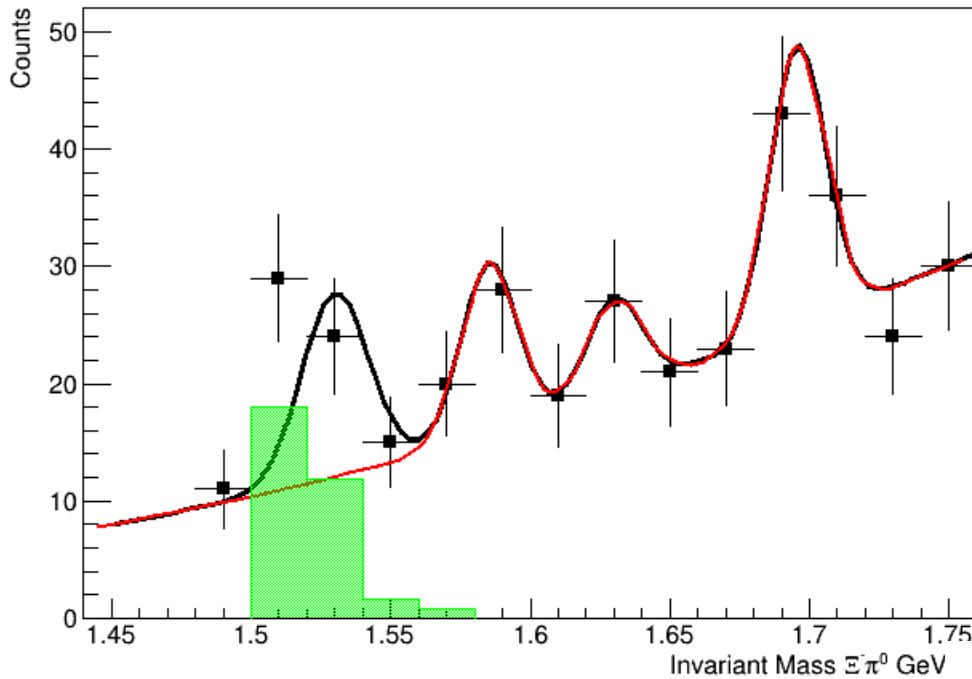


Figure 8.10: Invariant Mass Distribution of E^{*+} in GeV with $\cos\theta_{GJ}$, between 0.6 and 0.8, with extracted $E(1530)$ having a yield of 32 ± 6 .

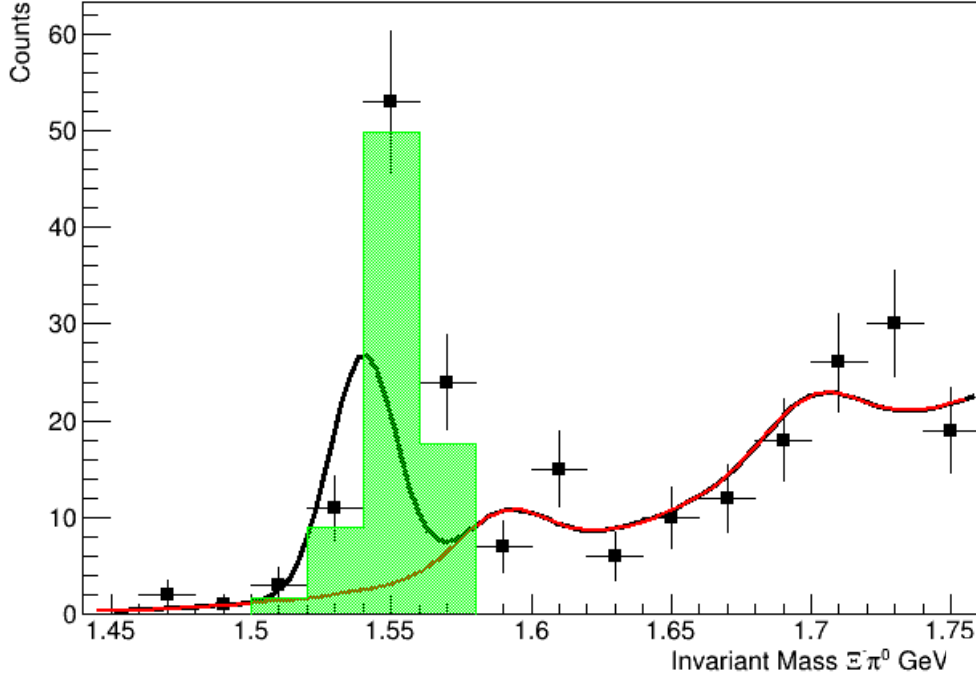


Figure 8.11: Invariant Mass Distribution of E^{*-} in GeV with $\cos\theta_{GJ}$, between 0.8 and 1.0, with extracted $E(1530)$ having a yield of 78 ± 9 .

The yield extraction process is repeated for all other $\cos\theta_{GJ}$ bins with the same fit functions (signal and background) except when the $E(1620)$ is present. If present, the additional peak is another background contribution. I generated $E(1530)$ efficiencies for each $\cos\theta_{GJ}$ bin using the monte carlo generator I created. The plots in Figures 8.12 and 8.13 show the same efficiency corrected yields for each $\cos\theta_{GJ}$ bin, but with different fits. Figure 8.12 assumes the $E(1530)$ is strictly a $J = 1/2$ state, while Figure 8.13 assumes a $J = 3/2$ state. The $E(1530)$ is clearly a $J = 3/2$ state, verifying the previous results of other measurements [2].

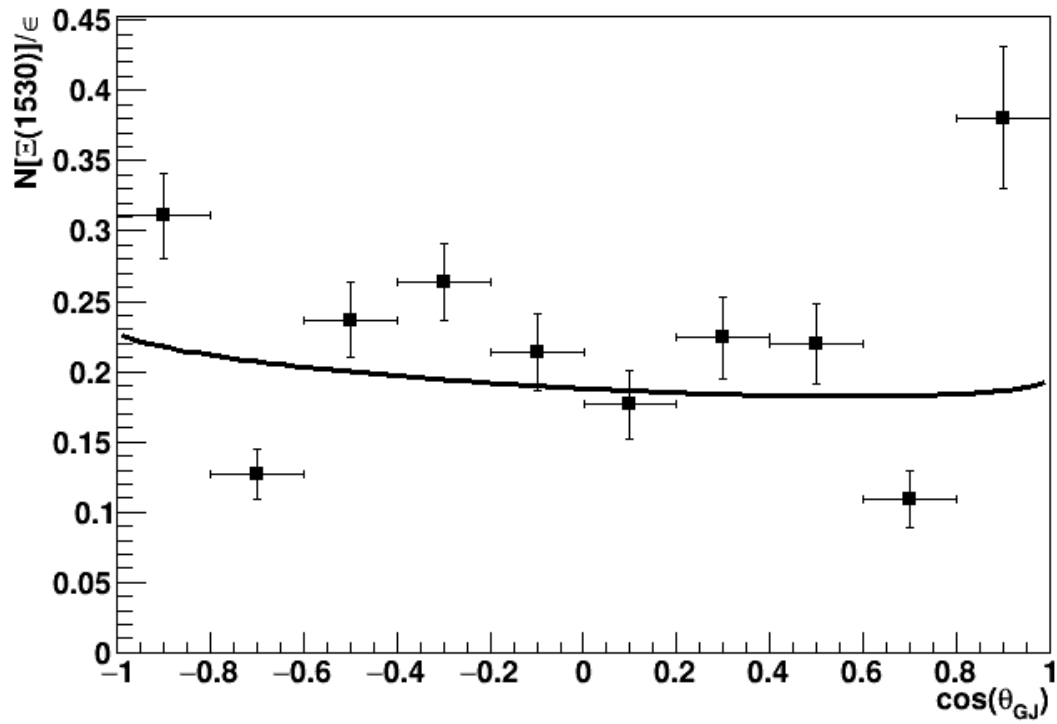


Figure 8.12: Efficiency corrected yields versus $\cos(\theta_{GJ})$ fit to an intensity function having only $J = 1/2$ contributions.

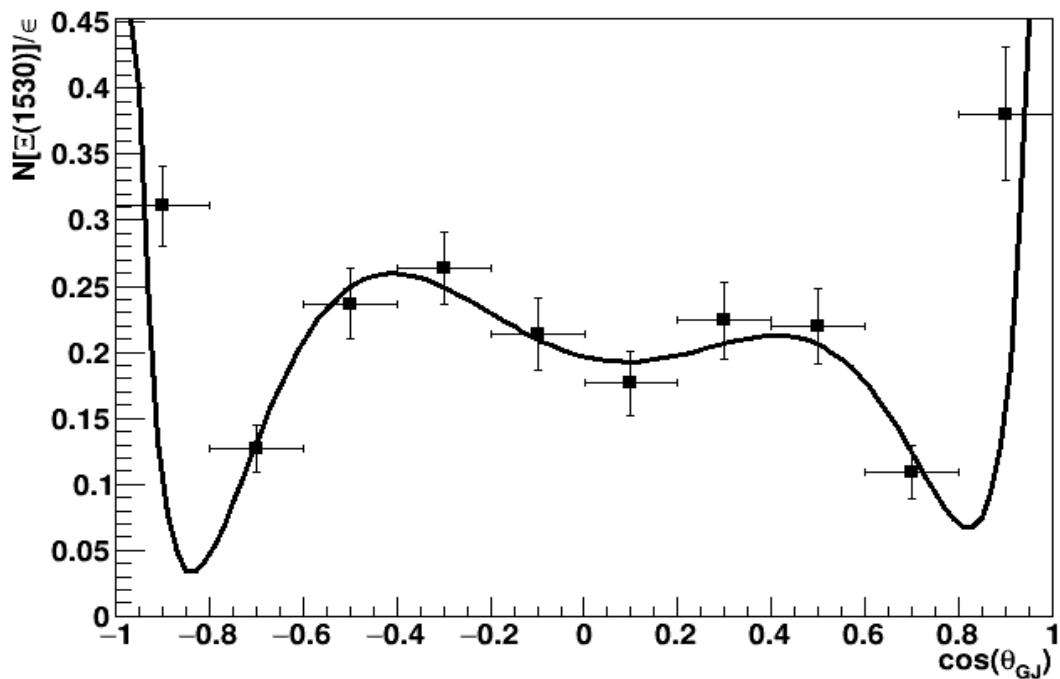


Figure 8.13: Efficiency corrected yields versus $\cos(\theta_{GJ})$ fit to an intensity function having only $J = 3/2$ contributions.

Chapter 9

CONCLUSIONS

9.1 Accomplishments

The cascade baryon sector has the potential for the discovery of new excited cascades states. There is also potential for discovering attributes of the known cascades that are currently unmeasured. I will give a brief summation of my attempts to deepen our knowledge of the cascade baryon sector of particle physics.

9.1.1 Cross Section Measurement

With the benefit of GlueX data, the photoproduced $\Xi(1530)$ signal was prominent enough to proceed with a cross section measurement at energies never before measured. Having the ability to reconstruct cleaner signals, I was able to make new, preliminary cross section measurements for the $\Xi(1530) \rightarrow \Xi^- \pi^0$. The cross section, $\sigma_{\Xi^- \pi^0}$, has a relatively flat distribution for incident photon energies between 7 and 11 GeV, with a value around 1.2 nb. Due to unforeseen difficulties with decay $\Xi(1530) \rightarrow \Xi^0 \pi^-$, a direct cross section measurement could not be made. However, after assuming isospin conservation, I was able to relate the two cross sections and produce a preliminary total cross section of about 3.5 nb.

9.1.2 Simultaneous Fit

With the precision that the GlueX experiment allows, I was also able to simultaneously fit one resonance signal to two separate channels. A statistically significant $\mathcal{E}(1690)$ signal in the $K^-\Lambda$ invariant mass spectrum coincided with $\mathcal{E}(1690)$ found in the $\mathcal{E}\pi$ invariant mass spectrum. The $\mathcal{E}(1690)$ signal in the $K^-\Lambda$ channel is small in comparison to the $\mathcal{E}(1530)$ peak. However, without modeling the $\mathcal{E}(1690)$, the fit has a confidence level that is a twelfth as large.

9.1.3 Branching Ratio

Studying the cascade states brought forth an opportunity to test isospin symmetry conservation in strong-force decays. With the excited cascade having two possible decays of the excited cascade going $\mathcal{E}\pi$ (namely $\mathcal{E}^* \rightarrow \mathcal{E}^0\pi^-$ and $\mathcal{E}^-\pi^0$). The Clebsch-Gordan coefficients of the isospin decomposition can determine the expected relative rate of production between the two channels. From the Clebsch-Gordan decomposition the expected rate of the $\mathcal{E}^0\pi^-$ production is twice that of the $\mathcal{E}^-\pi^0$. The relative rate of production was found to follow the Clebsch-Gordan coefficients to within two standard deviations. The ratio based off non-efficiency corrected yields was found to be

$$\frac{N[\mathcal{E}^-(1320)]}{N[\mathcal{E}^0(1320)]} \approx 0.54.$$

9.1.4 PWA

The final part of my analysis was a PWA. While the $\mathcal{E}(1530)$ quantum numbers have been determined experimentally, I was able to verify that the $\mathcal{E}(1530)$ is consistent with a $J = 3/2$ state. An interesting byproduct of the PWA was the discovery of a consistent

feature, I call F(1580). The feature F(1580) has a stable position to the right of the $\mathcal{E}(1530)$. This feature may help explain the exorbitant FWHM found from the simultaneous fit and given in Table 7.2 for the $\mathcal{E}(1620)$ when compared to other experimentally measured values. Interestingly with the paucity of detected cascade resonances detected, we expect to find more states below the mass of 2.4 GeV.

9.2 Future work

The next step with regards to the total cross section measurement is to further refine the event generator to match the experimental distribution of the $\mathcal{E}(1530)$ decays as seen in the PWA analysis shown in this document. Additionally, the values of the cross sections are consistent over different running periods should be ensured. The cross-section measurements for the $\mathcal{E}^{*-} \rightarrow \mathcal{E}^- \pi^0$ decay, from GlueX data sets not utilized in my cross-section analysis, must be obtained and compared. The study of isospin symmetry conservation can be made more precise by efficiency correcting the branching ratios between the neutral and negatively charged decay channels of the \mathcal{E}^{*-} . In the near future, a precision measurement of the total cross section for the $\mathcal{E}(1530)$ can be published.

While the $\mathcal{E}(1690)$ is known to couple to the $K^- \Lambda$ and $\mathcal{E}\pi$ channels, the branching fraction between the two has yet to be measured. To make the first-time measurement of the $\mathcal{E}(1690)$ branching ratio, i.e., $\Gamma(\mathcal{E} \rightarrow K^- \Lambda) / \Gamma(\mathcal{E} \rightarrow \mathcal{E}\pi)$, the efficiencies for each decay channel must be well understood. And, as part of the required efficiency study, a custom event generator for the $\mathcal{E}(1690)$ must be created.

Lastly, the PWA has a lot of promise for future studies. With the machinery in place, and more statistics imminent from Jefferson Lab, the same analysis as shown in this document can be performed, but on the $\Xi(1690)$. A PWA of the $\Xi(1690)$ will allow for the publication of a first-time measurement of the total angular momentum J of the $\Xi(1690)$. There are additional avenues of exploration. The possible $\Xi(1620)$ needs to be further measured. More data, along with monte carlo studies, will be needed to uncover the nature of the $F(1580)$. We must determine if the $F(1580)$ feature is an artifact of cuts and/or detector efficiency. For completeness, a PWA for the prominent $\Xi(1820)$ peak in the $K^- \Lambda$ spectrum should be performed to confirm the designation of $J = 3/2$.

References

- [1] S. Capstick and N. Isgur, Phys. Rev. D 34, 34 (1986). DOI:10.1103/PhysRevD.34.2809
- [2] P.A. Zyla et al. Review of Particle Physics. to be published in Prog. Theor. Exp. Phys. 2020, 083C01, 2020
- [3] J. T. Goetz Cascade Spectroscopy and Recent E^* Photo-production Results from CLAS. AIP Conference Proceedings **1257**, 553 (2010); <https://doi.org/10.1063/1.3483392>
- [4] M. Dugger and B. G. Ritchie, “Experimental Medium Energy Physics at Arizona State University” September 2018
- [5] T. Melde, W. Plessas and B. Sengl, Phys. Rev. D 77, 114002 (2008)
- [6] P. Petreczky, T. Izubuchi, L. Jin, C. Kallidonis, N. Karthik, S. Mukherjee, C. Shugert, and S. Syritsyn, Pion structure from Lattice QCD, 2018. arXiv:1812.04334.
- [7] S. Bethke. Experimental tests of asymptotic freedom. Prog. Part. Nucl. Phys., 58:351–386, 2007.
- [8] S. Capstick and W. Roberts, Prog. Part. Nucl. Phys. 45, S241 (2000) [nucl-th/0008028].
- [9] C. W. Salgado, D. P. Weygand, Phys. Rept. 537 (2014) 1–58. doi:10.1016/j.physrep.2013.11.005. arXiv:1310.7498.
- [10] Timeline,” *Timeline*” / *Jefferson Lab*. [Online]. Available: <https://www.jlab.org/about/visitors/history>. [Accessed: 21-Mar-2022].
- [11] S. Adhikari et al, “The GlueX Beamline and Detector”, 2020, eprint 2005.14272}, <https://arxiv.org/pdf/2005.14272.pdf>
- [12] R. Jones, “Intense beams of polarized and nearly monochromatic photons from coherent bremsstrahlung,” Coherent Bremsstrahlung Beam. [Online]. Available: <https://zeus.phys.uconn.edu/halld/wshop-7-1997/>. [Accessed: 21-Mar-2022].
- [13] E. Pooser, The GlueX Start Counter and Beam Asymmetry Σ in Single π^0 Photoproduction (Thesis/Dissertation) / *OSTI.GOV*, 26-Mar-2016. [Online]. Available: <https://www.osti.gov/servlets/purl/1351529>. [Accessed: 21-Mar-2022].
- [14] Ali, A. et al. “The GLUEX DIRC Program.” Journal of Instrumentation 15.04 (2020): C04054–C04054. Crossref. Web.
- [15] “Run periods,” *Run Periods - GlueXWiki*. [Online]. Available: https://halldweb.jlab.org/wiki/index.php/Run_Periods. [Accessed: 21-Mar-2022].
- [16] S. Dobbs and D. Lersch, “Kinematic Fitting in Hadron Physics,” *fsu.edu*. [Online]. Available: <http://www.hadron.physics.fsu.edu/>. [Accessed: 24-Mar-2022].
- [17] J.T. Goetz, et al., CLAS Collaboration, Phys. Rev. C 98 (2018) 062201, arXiv:1809.00074 [nucl-ex].

- [18] L. Guo et al., Phys. Rev. C 76, 025208 (2007).
- [19] A. Ernst” Total Cross Section of $\Xi(1320)$ in Photoproduction using the GlueX Detector at Jefferson Lab” [Online]. Available: https://halldweb.jlab.org/DocDB/0040/004069/009/Ernst_Analysis_Note_May2019_v2.pdf